(2)

Theoretical Study on Chemical Bonding around Lattice Imperfections in 3d-Transition Metal Compounds

(3d遷移金属化合物における欠陥構造の化学結合に関する理論研究)

Masataka MIZUNO

Department of Materials Science and Engineering
Kyoto University

1997

Contents

Chapter 1
Genaral Introduction

One of the central paradigms in modern materials science is that lattice imperfections dominate macroscopic properties of materials. Each material has its own advantages but most of single materials are not applicable to practical use. One of the most promising ways of modifying the properties of materials is to dope them with other elements. Interfaces play a key role to join different types of materials. Great efforts to reveal behaviors and nature of lattice imperfections, such as point defects, dislocations, planer faults, and interfaces have therefore been conducted in the past few decades. In order to discuss the influence of lattice imperfections, the change of the geometric and electronic structures induced by lattice imperfections has to be considered. Around lattice imperfections, there are lattice strains which arise from the lattice mismatch between matrix and additional elements. The chemical bonding around lattice imperfections is expected to be different from that of perfect crystalline elements or compounds due to the change of the electronic structure. Therefore, theoretical approach for lattice imperfections can be classified into two categories: One is based on the strain energy analyses, and the other is due to the electronic structure analyses. Although the strain energy approach is more widely used for treating the imperfections in general, it does not mean that the electronic structure has minor contribution to the behavior of the imperfections. These two approaches are mutually dependent, since the strain is originated from the spatial distribution of electron clouds around the imperfections. Major reason for the deficiency of electron theory for the imperfections is due to the difficulty of obtaining physical insight for electronic mechanisms behind the behavior and nature of the imperfections. Electrons obey the Schrödinger equation whose solution is not easy to imagine without special training. In polyatomic systems, we need to perform numerical calculations to solve the Schrödinger equation accurately. Especially when imperfections are included in the system, since the size of the calculation becomes large, we need to work with very fast computers that has not been available until recentness.

Transition metal compounds with the second and third row non-metal elements show wide variety of physical and chemical properties. A diversity of crystal structures can be noticed as well. Properties of pure transition metals have been extensively studied in the metallurgy society. Another well studied system is transition metal-oxides. A large number of studies on the oxides have been

piled up mainly in the field of inorganic chemistry/physics. In between these two extreme cases, variety of transition metal compounds have left unclarified in detail. Not only their imperfections but also the perfect bulk properties have not been sufficiently investigated. On the theoretical side, a considerable number of theoretical calculations have been performed to reveal electronic structures of transition metal compounds. However, targets of these works are limited to compounds having attractive unique properties for researchers performing theoretical calculations.

Three-dimensional periodicity is lost at lattice imperfections in polycrystalline materials. Theoretical study should, therefore, be able to clarify how the electronic structure at the imperfections differ from the perfect lattice. Band structure calculation imposing periodic boundary conditions requires large super cell if one desires to calculate the electronic structure of the planer imperfections, i.e., surface and interface. It is difficult to treat the electronic structure not only at the imperfections but also in perfect bulk compounds which have large unit cells by band structure calculations. On the other hand, cluster-calculation can be applied to any atomic arrangements and is a powerful tool to investigate the relationship between local atomic structure and electronic states. Moreover, the electronic structure is calculated not in the reciprocal space but in the real space, local chemical bonding can be intuitionally understood.

In the present work, the author calculated electronic structures of model clusters for the perfect crystalline compounds and lattice imperfections by first principles molecular orbital calculations using the DV-Xα cluster method. The author discussed the chemical bonding of solutes and interfaces as lattice imperfections based on the mechanism of the chemical bonding.

In Chapter 3, a systematic calculation for titanium compounds with the second and third row elements was performed. In order to estimate the strength of the covalent bonding quantitatively, the covalent bond density was evaluated. The mechanism and strength of the chemical bonding in these titanium compounds was investigated.

In Chapter 4, a systematic study for the electronic structure of 3d transition metal carbides was conducted. The mechanism of the chemical bonding in these carbides was discussed. In order to clarify a trend of the chemical bonding in these carbides, the strength of the metal-carbon and metal-metal bonds was quantitatively discussed.

Chapter 5 deals with Fe_3C containing solute atoms. Fe_3C usually contains some alloying elements such as Cr and Mn when it is present in steel. The electronic structure of Fe_3C containing

3d transition metal (Ti, V, Cr, Mn, Co and Ni) as solute atoms was calculated and the influence of the solute atoms on the chmical bonding was discussed.

Chapter 6 deals with the Fe/TiC, Fe/TiN and Fe/TiO interfaces with Baker-Nutting orientation relationship. These interfecaes have been used for precipitation hardening or intragranular ferrite nucleation site in steel industry. The electronic structures of these interfaces were calculated in order to investigate the mechanism of the interfacial bond with interests of the difference among Fe/TiC, Fe/TiN and Fe/TiO interfaces.

In Chapter 7, the chemical bonding of solute atoms in carbides and the metal/3d transition metal compoud interfaces was generally discussed based on the mechanism of the chemical bonding in perfect crystalline compounds and lattice imperfections investigated in preceding chapters.

Chapter 2
Computational method

2.1 Hartree-Fock-Slater approximation

Within the Hartree-Fock approxiamtion, one-electron wavefunction is wrriten as

$$h(\boldsymbol{r}_1)\phi_k(\boldsymbol{r}_1) = \varepsilon_k\phi_k(\boldsymbol{r}_1) \tag{2-1}$$

where

$$h(\boldsymbol{r}_1) = \left\{ -\frac{1}{2}\nabla_1^2 - \sum_v \frac{Z_v}{\boldsymbol{r}_{1v}} + \sum_l \int \frac{\phi_l^*(\boldsymbol{r}_2)\phi_l(\boldsymbol{r}_2)}{r_{12}} d\boldsymbol{r}_2 + V_{Xk}(\boldsymbol{r}_1) \right\} \tag{2-2}$$

is one-electron Hamiltonian. The first, second, third and forth term in the right-hand side in (2-2) are the kinetic energy operator, the nuclear plus core potential, the Coulomb potential with other electrons and the exchange term, respectively.

The exchange term can be written as

$$V_{Xk}(\boldsymbol{r}_1) = -\frac{\sum_l \int \phi_k^*(\boldsymbol{r}_1)\phi_l^*(\boldsymbol{r}_2)\frac{1}{r_{12}}\phi_l(\boldsymbol{r}_1)\phi_k(\boldsymbol{r}_2)d\boldsymbol{r}_2}{\phi_k^*(\boldsymbol{r}_1)\phi_k(\boldsymbol{r}_1)} . \tag{2-3}$$

Slater [1] has suggested an approximation to (2-3) in which the exchange term depends only the charge density, ρ. The exchange term is given by

$$V_{Xc}(\boldsymbol{r}) = -3\alpha\left[\frac{3}{4\pi}\rho(\boldsymbol{r})\right]^{\frac{1}{3}} \tag{2-4}$$

where, the factor α is a scaling parameter with a value between 2/3 to 1. The value of 0.7 is adequate for many molecular orbital calculations and employed in all present calculations.

2.2 DV-Xα method

In this work, the DV-Xα cluster method [2] based on the Hartree-Fock-Slater approxiamtion is used to calculate the electronic state of the model clusters from first principles. The molecular orbital wave function is expressed by linear-combination of atomic orbitals (LCAO) and is written as

$$\phi_l = \sum_i c_{il}\chi_i \tag{2-5}$$

where c_{il}'s are coefficients. As the basis function c_i, we use the numerical atomic orbitals obtained by solving radial part of the Schrödinger equation for individual atoms in a given cluster. The

matrix elements H_{ij} and S_{ij} in the secular equation **HC=ESC** are evaluated as

$$H_{ij} = \sum_k \omega(r_k)\chi_i(r_k)\boldsymbol{h}(r_k)\chi_j(r_k) \tag{2-6}$$

$$S_{ij} = \sum_k \omega(r_k)\chi_i(r_k)\chi_j(r_k) \tag{2-7}$$

by the DV numerical integration scheme [3], where $\boldsymbol{h}$ is the one-electron Hamiltonian operator, r_k is one of the sample points and $w(r_k)$ is the integration weight for the sample point.

2.3 Mulliken population analysis

In order to evaluate the magnitude of chemical bondings, the Mulliken population analysis [4] is employed. The orbital population, $Q_i(l)$, and the overlap population, $Q_{ij}(l)$, of the l th molecular orbital between c_i and c_j are defined by

$$Q_i(l) = \sum_l \sum_j f_l C_{il} C_{jl} \sum_k \omega(r_k)\chi_i(r_k)\chi_j(r_k) \tag{2-8}$$

$$Q_{ij}(l) = \sum_l f_l C_{il} C_{jl} \sum_k \omega(r_k)\chi_i(r_k)\chi_j(r_k) \tag{2-9}$$

where f_l is the occupation number of the l th molecular orbital, and r_k is one of the sample points and $w(r_k)$ is the integration weight for the sample point. The orbital population is useful to determine the effective atomic charge. The bond overlap population between A and B atoms is given by

$$Q_{AB} = \sum_{i\in A}\sum_{j\in B}\sum_l Q_{ij}(l) \tag{2-10}$$

The overlap population can be used as a measure of strength of the covalent bonding.

Reference

[1] J. C. Slater, Quantum Theory of Molecules and solids Vol. 4 (McGraw-Hill, New York, 1974).

[2] H. Adachi, M. Tsukada and C. Satoko, *J. Phys. Soc. Jpn.* **45**, 875 (1978).

[3] F.W. Averill and D. E. Ellis, *J. Chem. Phys.* **59**, 6412 (1973).

[4] R. S. Mulliken, *J. Chem. Phys.* **23**, 1833 (1955).

Chapter 3
Chemical bonding of titanium compounds

3.1 Introduction

Some of titanium compounds possess interesting physical and chemical properties. For example, TiB_2 and TiC possess high melting point, hardness and metallic conductivity. TiS_2 have been investigated for the use of cathode material in Li^+ ion batteries because Li^+ ion can be intercalated between the S layers in TiS_2. Therefore, not only for interests in their electronic structures but also for their technological importance, considerable number of theoretical calculations for TiB_2 [1-6], TiC [7-36], TiS_2 [37-48] and other titanium compounds have been performed. In the case of TiC, it is expected that there is no significant C-C bond in TiC because the C-C distance in TiC is about twice as the covalent C-C distance [49]. In several theoretical calculations for TiC, by the use of analysis of partial density of states (PDOS), it was found that there was a strong interaction between the Ti-3d and C-2p orbitals which is the origin of the strong covalent Ti-C bond. Regarding the Ti-Ti bonding, it is expected that the strength of the Ti-Ti bond is not so large as the Ti-C bond because the Ti-3d band is almost unoccupied. On the other hand, in the case of TiB_2, it is not so easy to estimate the chemical bonding as in the case of TiC. In several band-structure calculations for TiB_2 [4-6], it was suggested that the strong covalent B-B bond was formed because the B-B distance was close to the covalent B-B distance and there was an overlap between the B-2s and B-2p bands in PDOS. However, PDOS in TiB_2 also indicated that there was strong Ti-B bonds because of the strong interaction between the Ti-3d and B-2p orbitals. The bond overlap population based on Mulliken population analysis can be used as a measure of the strength of the covalent bondings. Burdett *et al.* [3] performed the extended Hückel type band-structure calculations for MB_2 (M=Ca to Ni) in the AlB_2 structure and found that the bond overlap population of the B-B bond was larger than that of the M-B bond. However, in order to estimate contribution of the covalent bonding, it is necessary to take account of not only the strength but also the number of the bonds in compounds. Namely, the number of the Ti-B and B-B bonds in TiB_2 in the unit volume are different. Therefore, it remains unsettled question what type of the chemical bonding is dominant in TiB_2. The same question applies to discussing the chemical bonding of $TiSi_2$ [50]. The difficulty in discussing the chemical bonding also arises in comparing the chemical bonding between compounds with different

crystal structures. Both TiC and TiB_2 are usually refereed as the compounds which possess high melting point and high hardness. However, only with these approaches, it is impossible to compare the chemical bonding quantitatively in different crystal structure, such as TiC and TiB_2.

In this work, the electronic structures of titanium compounds with the second-row elements, TiB, TiB_2, TiC, Ti_2N, TiN, TiO and TiO_2 and with the third-row elements, TiSi, $TiSi_2$, TiP, TiS and TiS_2 were calculated by first principles molecular orbital calculations using the DV-Xα cluster method. The origin of the covalent bondings in every compound was investigated . Furthermore, in order to estimate the covalent bonding quantitatively in these compounds with different crystal structures, covalent bond density was calculted by taking account of the strength and the number of the each type of the bonds. The chemical bonding of the Ti-X, Ti-Ti, X-X and total covalent bonding were quantitatively discussed by the use of the bond overlap population and the covalent bond density.

3.2 Crystal Structures

The crystal structure of TiB is FeB type orthorhombic structure which belongs to the spacegroup *Pnma*, with a=6.12Å, b=3.06Å and c=4.56Å [51] (Fig. 3-1). There are four Ti and four B atoms in the unit cell. Every B atom is surrounded by seven neighboring Ti atoms at an average distance of 2.385Å which form a mono-capped trigonal prism as seen in Fig. 3-1 (c). The trigonal prisms are linked together by sharing their corners and edges along the *a* and *c*-axis, and by sharing their plains along the *c*-axis (Fig. 3-1 (b)). Every B atoms has two nearest neighbor B atoms and is joined together to make a zigzag chain along *b*-axis. The B-B distance of 1.83Å is close to the covalent B-B distance of 1.76Å. TiB_2 has AlB_2 type hexagonal structure which belongs to the spacegroup *P6/mmm*, with *a*=3.030Å and *b*=3.232Å[52] (Fig. 3-2). There are one Ti and two B atoms in the unit cell. Every B atom has three nearest neighbor B atoms and is joined together to make a graphite-like layer. The B-B distance of 1.75Å is almost the same as the covalent B-B distance of 1.76Å. Ti atoms are arranged in hexagonal layers. The Ti and B layers are stacked alternately along the c-axis. The intralayer Ti-Ti distance is equal to the length of *a*-axis (=3.030Å) which is slightly larger than the metal Ti-Ti distance of 2.924Å. The interlayer Ti-Ti distance is equal to the length of *c*-axis (=3.232Å). Regarding the local structure of B atoms, every B atom is surrounded by six nearest neighbor Ti atoms which form a trigonal prism. The trigonal prisms are linked by sharing their

TiB

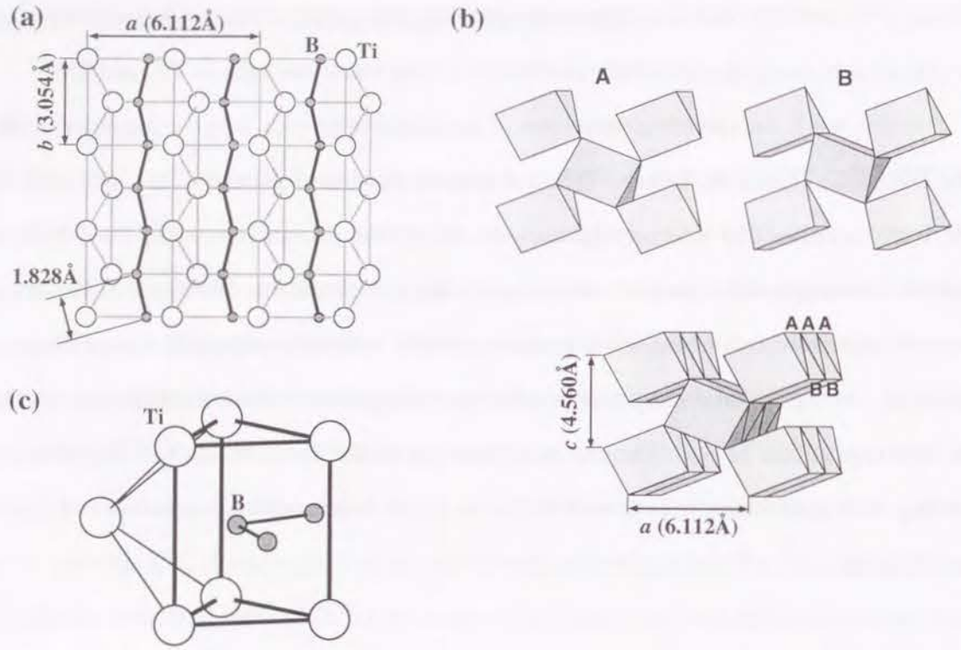

Fig. 3-1 The structure of TiB.
(a) The (001) projection.
(b) The arrangement of the trigonal prisms.
(c) Local structure around B atom: a mono-capped trigonal prism composed of seven Ti atoms and one B atom.

TiB_2

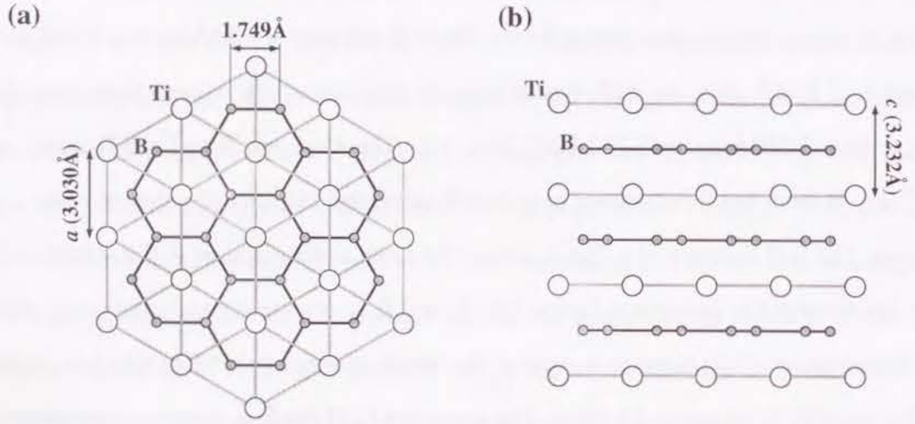

Fig. 3-2 The structure of TiB_2.
(a) The (001) projection.
(b) The stacking of the Ti and B layers.

planes.

TiC, TiN and TiO have the rock-salt type cubic structure which belongs to the spacegroup , with a=4.3275Å [53], 4.240Å [54] and 4.1766Å[55], respectively (Fig. 3-3 (a)). There are four Ti and four X (X=C, N, O) atoms in the unit cell. Every Ti and X atoms are located in a octahedron composed of six another kind of atoms at a distance of half of a-axis length. The Ti-Ti and X-X distances are the same, 3.092, 3.087 and 2.954Å in TiC, TiN and TiO, respectively. These Ti-Ti distances are a little larger than metal Ti-Ti distance of 2.924Å.

The crystal structure of Ti_2N and TiO_2 is rutile type tetragonal structure which belongs to the spacegroup $P4_2/mnm$, with a=4.9428Å and c=3.0357Å in Ti_2N[56] (Fig. 3-3 (b)) and with a=4.5937Å and c=2.9587Å in TiO_2 [57]. In TiO_2, two Ti and four O atoms are located in 2a and 4f Wyckoff positions in the unit cell, respectively. The positions of Ti and N atoms in Ti_2N are alternated for those of TiO_2. In following sentences, we take up the structure of Ti_2N. Every N atom is surrounded by six neighboring Ti atoms at an average distance of 2.078Å which form a distorted octahedron. The distorted octahedra are linked by sharing their edges along the c-axis and by sharing their corners along the [110] and [1$\bar{1}$0] directions. Every Ti atom has eleven neighboring Ti atoms at an average distance of 2.946Å.

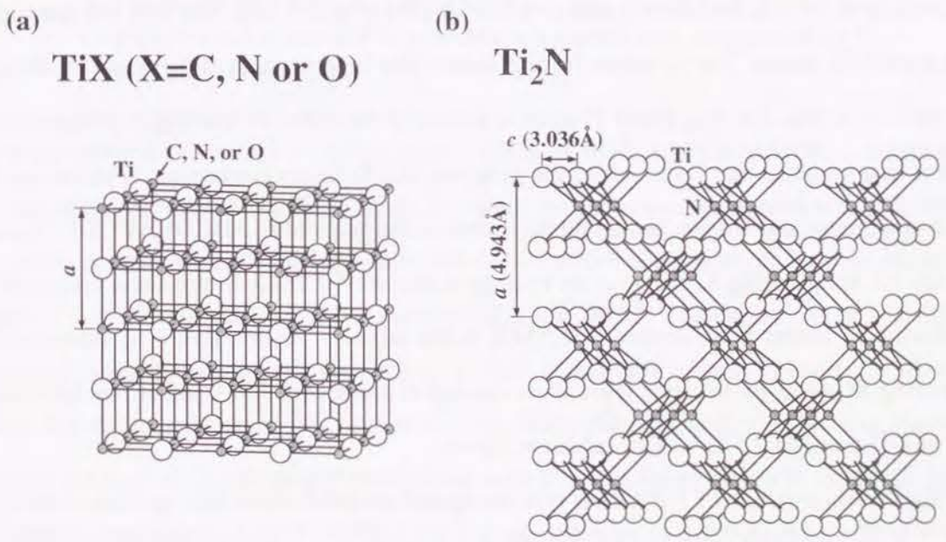

Fig. 5-3 (a) The structure of TiX (X=C, N or O).
(b) The structure of Ti_2N.

$TiSi_2$

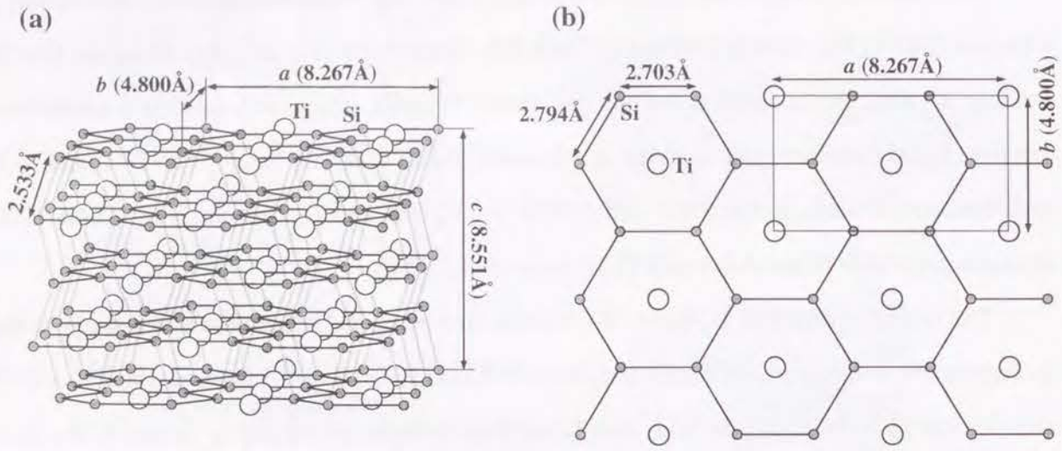

Fig. 5-4 (a) The structure of $TiSi_2$.
(b) The (001) projection of one layer in $TiSi_2$.

TiSi has the same crystal structure as TiB. The lattice parameters are a=6.57Å, b=3.64Å and c=5.03Å [58]. The Si-Si distance is 2.22Å which is slightly shorter than the covalent Si-Si distance of 2.34Å. The crystal structure of $TiSi_2$ is orthorhombic structure which belongs to the spacegroup *Fddd*, with a=8.2671Å, b=4.8000Å and c=8.5505Å [59] (Fig. 3-4 (a)). The unit cell has eight Ti atoms and 16 Si atoms. The Si atoms form graphite-like layers which is distorted by about 3% along the b-axis (Fig. 3-4 (b)). Every Ti atom is located in the center of a hexagon composed of six Si atoms in a graphite-like layer. All of the graphite-like Si layers containing Ti atoms have the same arrangement and are stacked along the c-axis in the sequence (ABCD)(ABCD)... Every Ti atom has six neighboring Si atoms at an average distance of 2.764Å in the same layer and four neighboring Si atoms at a distance of 2.554Å in the adjacent layers. Every Si atom has three neighboring Si atoms in the same layer at an average distance of 2.764Å and two neighboring Si atoms at a distance of 2.533Å in the adjacent layers.

The crystal structure of TiP is TiAs type hexagonal structure which belongs to the spacegroup $P6_3/mmc$, with a=3.499Å and c=11.700Å [60] (Fig. 3-5). There are four Ti atoms on 4*f* site, two P_1 atoms on 2*a* site and two P_2 atoms on 2*d* site in Wyckoff notation in the unit cell. The TiP structure consists of stacking of hexagonal closest-packing Ti and P layers. As seen in Fig. 3-5 (b), the Ti and

TiP

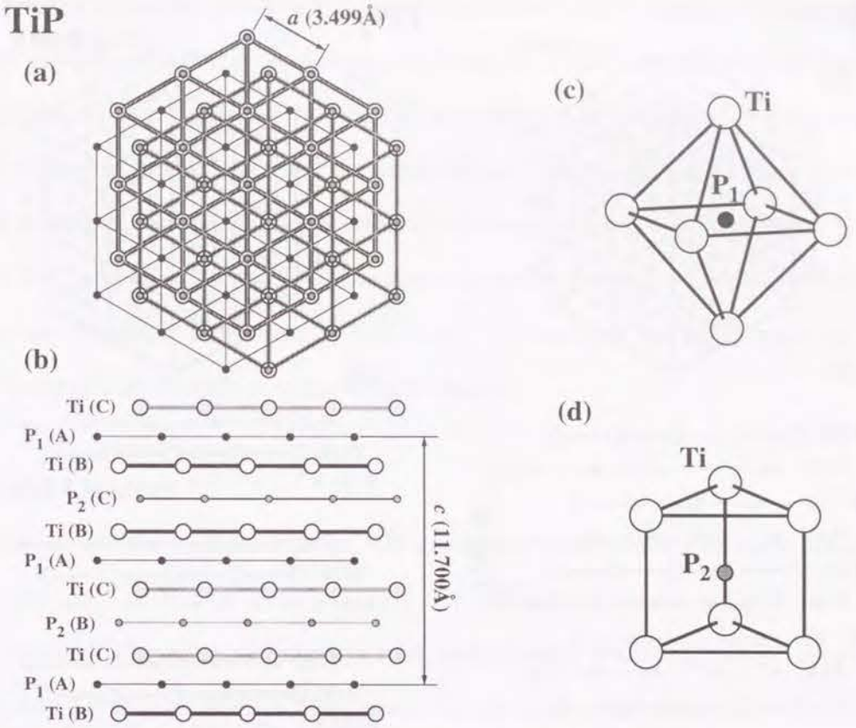

Fig. 3-5 The structure of TiP.
(a) The (001) projection.
(b) The stacking of the Ti and P layers.
(c) Local structure around P atom on 2*a* site: a distorted octahedron composed of six Ti atoms and one P atom.
(d) Local structure around P atom on 2*d* site: a trigonal prism composed of six Ti atoms and one P atom.

P layers are stacked alternately in the sequence (ABCBACBCA) (ABCBACBCA)... where the A, B and C layers are composed of the P_1, Ti and P_2 atoms, respectively. The nearest neighbor distance in the layers is equal to the length of a-axis (=3.499Å), which is quite larger than the metal Ti-Ti distance of 2.951Å or the covalent P-P distance of 2.20Å. Every Ti atom has six neighboring Ti atoms in the same layer, one at a distance of 3.112Å in one side of next Ti layer and three at a distance of 3.402Å in the other side of next Ti layer. Every P atom has six neighboring P atoms in the same layer and six neighboring P atoms in the next P layers. Every Ti and P_1 atoms are located in ochtahedra composed of six P atoms at an average distance of 2.495Å and six Ti atoms at a distance of 2.440Å, respectively (Fig. 3-5 (c)). Every P_2 atom is located in a trigonal prism composed of six Ti atoms at a distance of 2.550Å (Fig. 5-5 (d)).

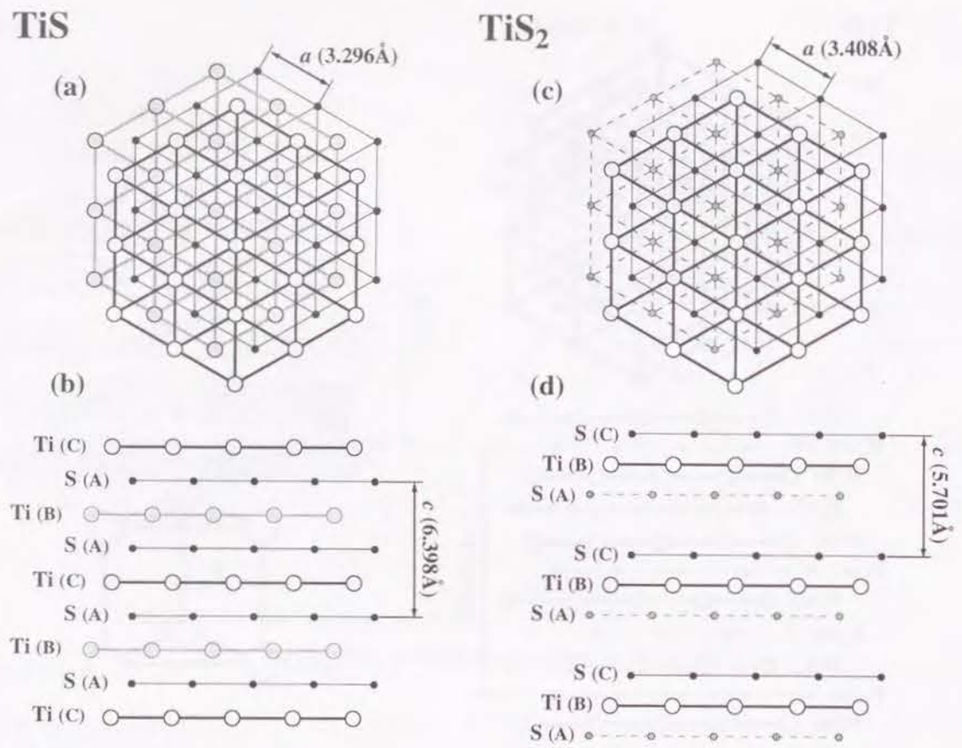

Fig. 3-6 The Structure of TiS and TiS_2.
(a) The (001) projection of the structure of TiS.
(b) The stacking of the Ti and S layers in TiS.
(c) The (001) projection of the structure of TiS_2.
(d) The stacking of the Ti and S layers in TiS_2.

The crystal structure of TiS is NiAs type hexagonal structure which belongs to the spacegorup $P6_3/mmc$ with a=3.296Å and c=6.398Å [61] (Fig. 3-6 (a),(b)). There are two Ti and two S atoms in the unit call. The TiS structure consists of stacking of hexagonal closest-packing Ti and S layers like TiP. As seen in Fig. 3-6 (b), the Ti and S layers are stacked alternately in the sequence (ABACA) (ABACA)..., where the A layers are composed of S atoms and both the B and C layers are composed of Ti atoms. Every Ti atom is located in a trigonal prism composed of six nearest neighbor S atoms and every S atom is located in a octahedron composed of six nearest neighbor Ti atoms. The Ti-S distance is 2.486Å. The intralayer Ti-Ti and S-S distances are equal to the length of a-axis (=3.296Å). The S-S distance is quite larger than the covalent S-S distance of 2.02Å. Every S atoms has two S atoms at a distance of 3.199Å in the next S layers. TiS_2 has CdI_2 type hexagonal structure which belongs to the spacegroup,with a=3.408Å and c=5.699Å [62] (Fig. 3-6 (c),(d)). There are one Ti

and two S atoms in the unit cell. The TiS_2 structure also consists of stacking of hexagonal closest-packing Ti and S layer, however, in contrast to TiP and TiS, a manner of stacking of Ti and S layers is not alternate. As seen in Fig. 3-6 (d), the TiS_2 structure can be considered as the stacking of the layers composed of one Ti layer and the adjacent two S layers. Every Ti atom is located in a distorted octahedron composed of six S atoms at a distance of 2.430Å. The interlayer S-S distance is 3.462Å and intralayer S-S and Ti-Ti distances are equal to a-axis (=3.408Å) which are quite larger than the covalent S-S and metal Ti-Ti distance. The interlayer spacing between the S layers is the same value of 2.851Å with or without the Ti layers.

3.3 Model Clusters

The model clusters composed about 100 atoms were employed in all present calculations for TiB, TiB_2, TiC, Ti_2N, TiN, TiO, TiO_2, TiSi, $TiSi_2$, TiP, TiS and TiS_2 shown in Fig. 3-7 and 3-8. In the case of TiO and TiO_2, the model clusters were embedded in Madelung potential generated by approximately 5,000 point charges. The atomic orbitals used in the present calculations are 1s-4p for Ti, 1s-2p for the second-row elements (B, C, N and O) and 1s-3d for the third-row elements (Si, P and S).

3.4 Covalent bond density

The bond overlap population gives us the strength of the covalent bondings between atoms. However, when comparing the covalent bondings in different crystal structures, it is not sufficient to estimate the strength of the covalent bonding using the bond overlap population because the difference of the crystal structure, such as the coordination number or the stoichiometry, affect on the value of the bond overlap population. Moreover, in order to estimate contribution of the covalent bondings in compounds, it is necessary to estimate not only the strength but also the number of the bonds in the compounds. In this work, in order to estimate the covalent bondings in different crystal structures, we calculate covalent bond density with taking account of the number of the covalent bondings in the unit cell.

In AB compound, the number of the bonds between A and B atoms in the unit cell, $N_{A\text{-}B}$, can be calculated by

$$N_{A\text{-}B} = n_A N_A^B = n_B N_B^A \qquad (3\text{-}1)$$

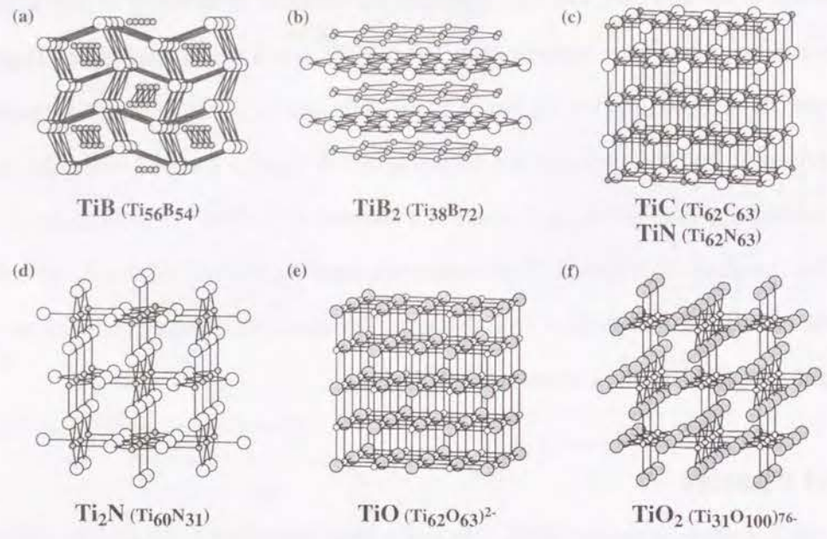

Fig. 3-7 The structure of model clusters employed in this work for the titanium compounds with the second-row elements: B, C, N and O. Open circles denote Ti atoms and filled circles denote X atoms (X=B, C, N or O).
(a) $Ti_{56}B_{54}$ cluster for TiB. (b) $Ti_{38}B_{72}$ cluster for TiB_2.
(c) $Ti_{62}C_{63}$ cluster for TiC and $Ti_{62}N_{63}$ cluster for TiN.
(d) $Ti_{60}N_{31}$ cluster for Ti_2N. (e) $(Ti_{62}O_{63})^{2-}$ cluster for TiO.
(f) $(Ti_{31}O_{100})^{76-}$ cluster for TiO_2.

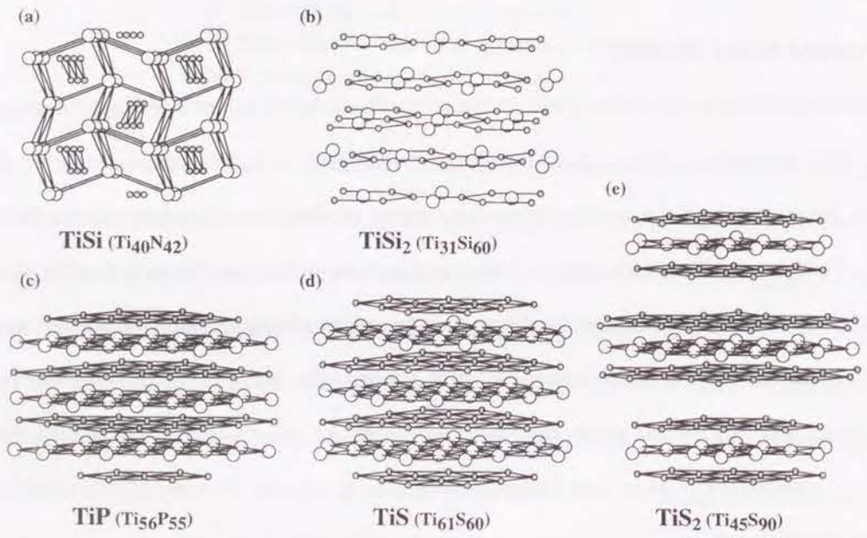

Fig. 3-8 The structure of model clusters employed in this work for the titanium compounds with the third-row elements: Si, P and S. Open circles denote Ti atoms and filled circles denote X atoms (X=Si, P and S).
(a) $Ti_{40}Si_{42}$ cluster for TiSi. (b) $Ti_{31}Si_{60}$ cluster for $TiSi_2$.
(c) $Ti_{56}P_{55}$ cluster for TiP. (d) $Ti_{61}S_{60}$ cluster for TiS.
(e) $Ti_{45}S_{90}$ cluster for TiS_2.

where n_A and n_B are the number of the A and B atoms in the unit cell, respectively, N_A^B is the number of the neighboring B atoms of the A atom and N_B^A is the number of the neighboring A atoms of the B atom. The number of the A-A and B-B bonds in the unit cell, $N_{A\text{-}A}$ and $N_{B\text{-}B}$, can written as

$$N_{A\text{-}A} = \frac{1}{2}\ n_A N_A^A \qquad (3\text{-}2)$$

$$N_{B\text{-}B} = \frac{1}{2}\ n_B N_B^B \qquad (3\text{-}3)$$

Since every compound has different unit cell volume, consider the number of the bonds in unit volume of $1Å^3$. The value of the number of the bonds, *N*, divided by the unit cell volume represents the number of the bonds in the unit volume. In order to take account of the strength and the number of bonds at the same time, the covalent bond density, ρ, is defined as

$$\rho_{A\text{-}B} = Q_{A\text{-}B}\, N_{A\text{-}B} / V \qquad (3\text{-}4)$$

where $Q_{A\text{-}B}$ is the bond overlap population between the A and B atoms and *V* is the unit cell volume. $\rho_{A\text{-}A}$ and $\rho_{B\text{-}B}$ can be obtained in the same way. Since the covalent bond density represents the strength of the covalent bonding per unit volume irrespective of crystal structures, the value of the covalent bond density can be compared between those in different crystal structures. Moreover, the total covalent bond density, which represents the covalency of the compound, can be calculated by summing up every ρ as following:

$$\rho_{Total} = \rho_{A\text{-}B} + \rho_{A\text{-}A} + \rho_{B\text{-}B} \qquad (3\text{-}5)$$

If there are more than two Wyckoff sites for one kind of atoms in the unit cell, such as P_1 and P_2 sites in TiP, every atom occupying the different site has to be regarded as different atom. Therefore, in the case of TiP, the covalent bond densities of Ti-P_1, Ti-P_2, Ti-Ti, P_1-P_2, P_1-P_1 and P_1-P_2 have to be evaluated separately. In this work, for simplicity, the same kind of the covalent bond density is summed each other as following:

$$\rho_{Ti\text{-}P} = \rho_{Ti\text{-}P_1} + \rho_{Ti\text{-}P_2} \qquad (3\text{-}6)$$

$$\rho_{P\text{-}P} = \rho_{P_1\text{-}P_2} + \rho_{P_1\text{-}P_1} + \rho_{P_2\text{-}P_2} \qquad (3\text{-}7)$$

In this way, the covalent bond density can be calculated irrespective of the number of Wyckoff sites in binary AB compound, which means that the covalent bond density is also applicable to more than ternary system compounds. Generally, when the unit cell has *n* Wyckcoff sites, there are $n(n+1)/2$ types of the bonds to be considered separately.

In some crystal structures, neighboring atoms which have significant contribution to the

covalent bonding are not only the first nearest neighbor atoms. For example, in body centered cubic (BCC) structure, the second nearest neighbor atoms are not farther enough to neglect their contribution to the covalent bonding. Figure 3-9 and 3-10 show the number of the neighboring atoms and the bond overlap populations as a function of the neighboring distance in metal α Ti with HCP structure and metal β Ti with BCC structure. The bond overlap populations are calculated using HCP-Ti_{57} and BCC-Ti_{51} clusters. In HCP-Ti, since the first nearest and second nearest neighbor distances are almost the same, the bond overlap populations for the first nearest and second nearest atoms are also the same. On the other hand, in BCC-Ti, the second nearest neighbor distance is about 15% longer than the first nearest neighbor distance. Therefore the bond overlap population for the second nearest neighbor atoms is less than half of that for the first nearest neighbor atoms, while it is not small enough to be neglected. If the second nearest neighbor atoms are regarded as the neighboring atoms, the number of the neighboring atoms are 14 and the bond overlap population is the average of that of eight first nearest neighbor and six second nearest neighbor atoms, i.e., $(0.282\times8+0.146\times6)/14 = 0.224$. This value is smaller than that in HCP-Ti, 0.240. If not only the first nearest neighbor atoms but also farther atoms have contribution to the covalent bonding like BCC structure and they are regarded as the neighboring atoms, the strength of the covalent bonding is underestimated using the average of the bond overlap populations. Moreover, the difference of the coordination number affects on the comparison of the bond overlap population. Therefore, it is doubtful to conclude from the comparison of the average of the bond overlap population that the covalent bonding in HCP-Ti is stronger than BCC-Ti. This is one of the reason why it is not sufficient to estimate only the strength of the covalent bonding when comparing between different crystal structures. If the covalent bond density is applied in this case, the value of HCP-Ti is 0.082/Å^3 and that of BCC-Ti is 0.087/Å^3.

The values for the distance and number of the bonds in the titanium compounds studied here are presented in Table 3-1. In this work, neighboring atoms which has significant contribution to the covalent bonding are taken into account irrespective of the bond distance. If neighboring atoms are not only the first nearest neighbor atoms such as BCC structure, the bonds whose distance is larger than the first nearest neighbor distance are also counted as one bond. Therefore, it is not always correct comparison to compare only the number of the bonds. Regarding the covalent bond density, since the number and the strength of the bonds are taken into account, the covalent bond

density can be always applied to comparison the covalent bonding.

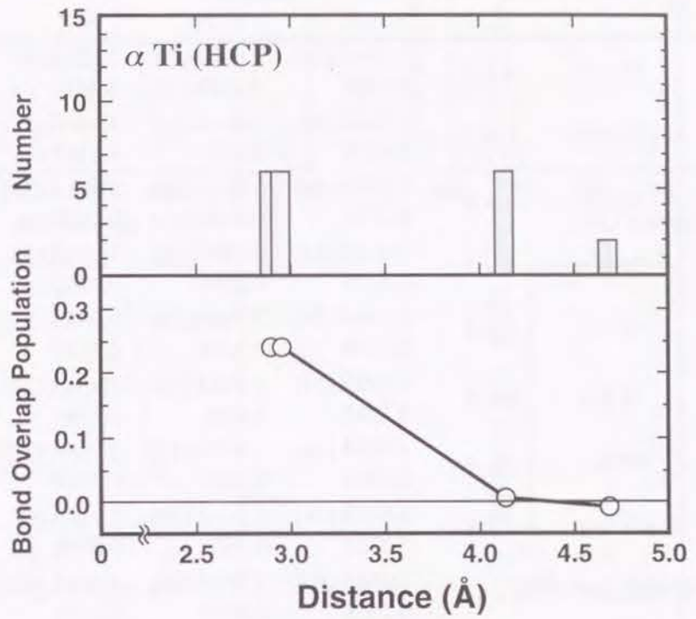

Fig. 3-9 The number of neighboring atoms and the bond overlap population as a function of the neighboring distance in metal α Ti with HCP structure.

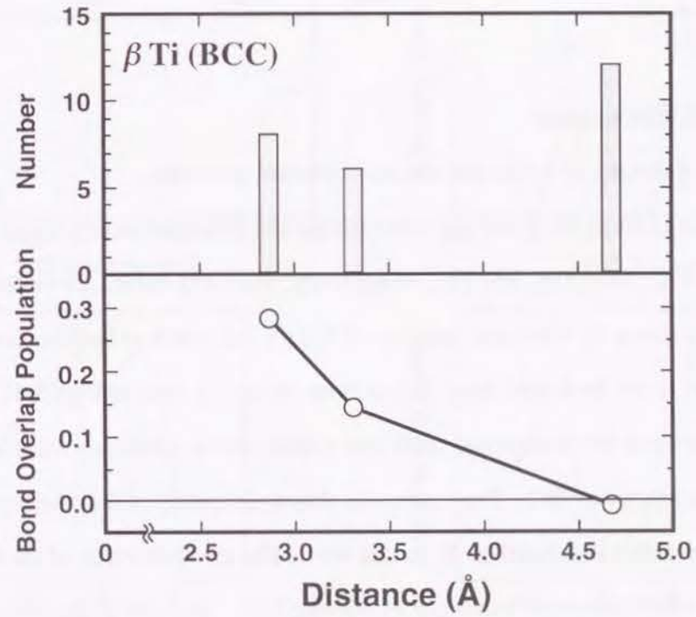

Fig. 3-10 The number of neighboring atoms and the bond overlap population as a function of the neighboring distance in metal β Ti with BCC structure.

Table 3-1 Geometrical data for the unit cell of titanium compounds studied in this work.

	Unit Cell Volume(Å^3)	Number of Atoms (Ti+X)	Average distance (Number of bonds in Unit Cell) Number of bonds in 1Å^3 Ti-X	Ti-Ti	X-X
TiC	85.117	4 + 4	2.385Å (28) 0.3290	2.994Å (20) 0.2350	1.828Å (4) 0.0470
TiB_2	25.697	1 + 2	2.382Å (12) 0.4670	3.081Å (4) 0.1557	1.749Å (3) 0.1167
TiC	81.127	4 + 4	2.165Å (24) 0.2958	3.061Å (24) 0.2958	3.061Å (24) 0.2958
Ti_2N	74.166	4 + 2	2.078Å (12) 0.1618	2.946Å (22) 0.2996	3.036Å (2) 0.0270
TiN	76.225	4 + 4	2.120Å (24) 0.3149	2.998Å (24) 0.3149	2.998Å (24) 0.3149
TiO	72.878	4 + 4	2.089Å (24) 0.3293	2.954Å (24) 0.3293	2.954Å (24) 0.3293
TiO_2	62.435	2 + 4	1.959Å (12) 0.1922	3.447Å (12) 0.1602	2.789Å (22) 0.3524
TiSi	118.964	4 + 4	2.635Å (28) 0.2354	3.363Å (20) 0.1681	2.216Å (4) 0.0336
$TiSi_2$	339.302	8 + 16	2.680Å (80) 0.2358	3.206Å (16) 0.0472	2.909Å (40) 0.1179
TiP	124.052	4 + 4	2.495Å (24) 0.1935	3.431Å (20) 0.1612	3.499Å (24) 0.1935
TiS	60.194	2 + 2	2.486Å (12) 0.1994	3.296Å (12) 0.1994	3.272Å (8) 0.1329
TiS_2	57.347	1 + 2	2.430Å (6) 0.1046	3.408Å (3) 0.0523	3.436Å (12) 0.2093

3.5 Results and discussion

3.5.1 Comparison of density of states and the experimental spectrum.

Figures 3-11 to 14 show the density of states (DOS) and the experimental X-ray photoemission spectrum (XPS) for TiC, TiO_2, $TiSi_2$ and TiS_2, respectively. The DOS curves are made by broadening the desecrate energy levels by Gaussian function of 1.0 eV full width at half-maximum (FWHM) and are shifted so as to set the Fermi level (E_F) at zero. As can be seen in Figs 3-11 to 14, there is good agreement between the theoretical DOS and experimental spectrum without the absolute value of the peak positions in TiO_2. The reason for this discrepancy is that the highest occupied molecular orbital (HOMO) is selected as E_F in this work. The absolute value of the DOS is shifted for compounds in which the clear band-gap exists like TiO_2. Therefore, the discrepancy is not essential in comparing the theoretical DOS and experimental spectrum. Model clusters employed in this work is thus confirmed to reproduce the feature of DOS for bulk compounds.

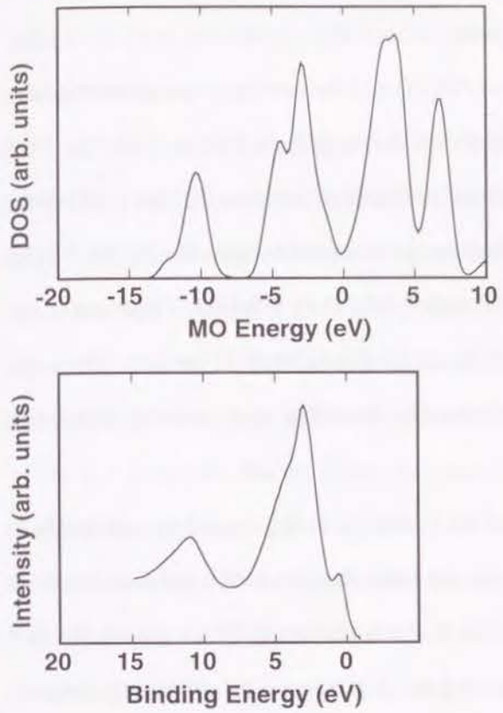

Fig. 3-11 Density of states and the experimental photoemission spectrum in ref. [63] for TiC.

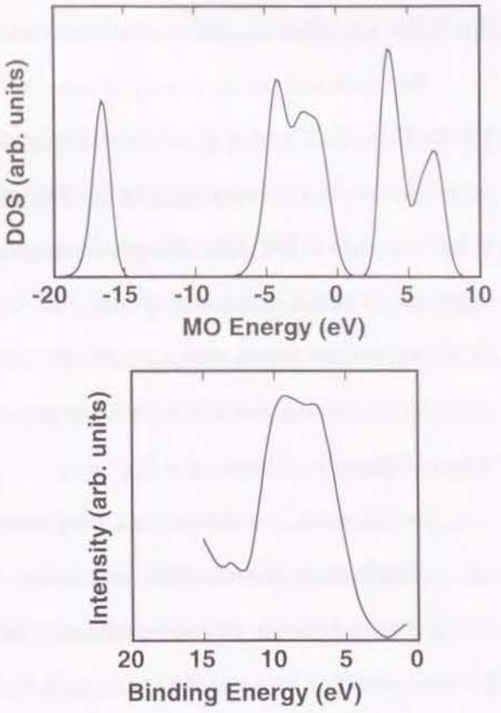

Fig. 3-12 Density of states and the experimental photoemission spectrum in ref. [64] for TiO_2.

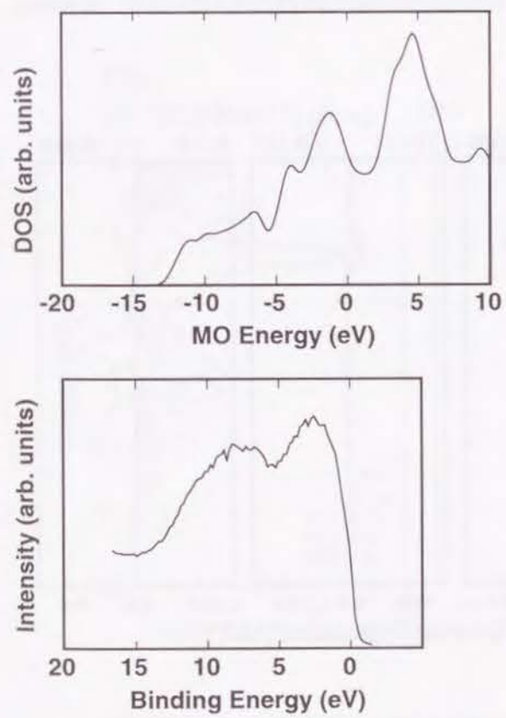

Fig. 3-13 Density of states and the experimental photoemission spectrum in ref. [65] for $TiSi_2$.

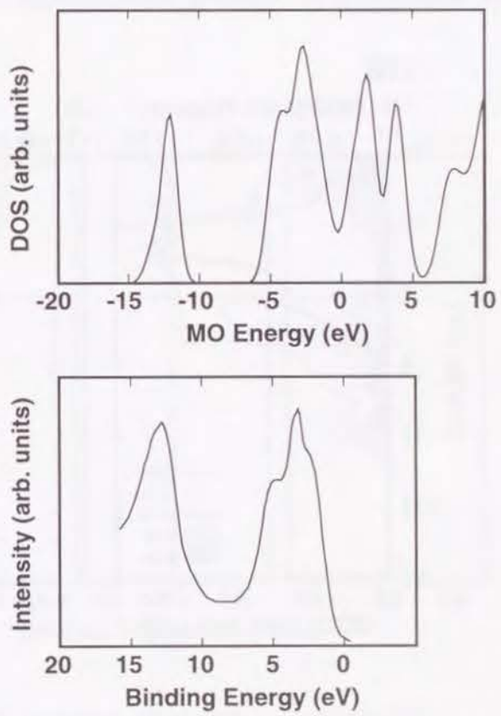

Fig. 3-14 Density of states and the experimental photoemission spectrum in ref. [66] for TiS_2.

3.5.2 Density of states and overlap population diagram

The total and partial density of states (TDOS and PDOS) and the overlap population diagrams for the Ti-X, Ti-Ti and X-X bonds of these model clusters are shown in Figs. 3-15 to 3-26. The DOS curves are made by broadening the discrete energy levels by Gaussian function of 1.0 eV full width at half-maximum (FWHM). The overlap population diagrams are obtained by convoluting the overlap population at each molecular orbital with Gaussian function of 1.0 eV FWHM. These curves of DOS and overlap population diagrams are shifted so as to set the Fermi level (E_F) at zero. The value written in each panel is the bond overlap population obtained by summing up the overlap population at each molecular orbital up to E_F.

In TiB, there is a continuous band lying from -12 eV and the Ti-3d, 4s and 4p and the B-2s and 2p bands overlap each other. Especially, as we shall see later, the interaction between the X-*n*s and X-*n*p can be seen only in borides and silicides. The B-B interaction in TiB is due to the B-B distance which is close to the covalent B-B distance and the B-B bond displays strong covalent bonding. Regarding the Ti-B bonding, all the valence orbitals have bonding contribution. The Ti-B bond mainly arises from the B-2p band interacting with Ti-3d, 4s and 4p orbitals. Mohn *et al.* [67] calculated the electronic structure of 3d transition metal mono-borides including TiB. They presented

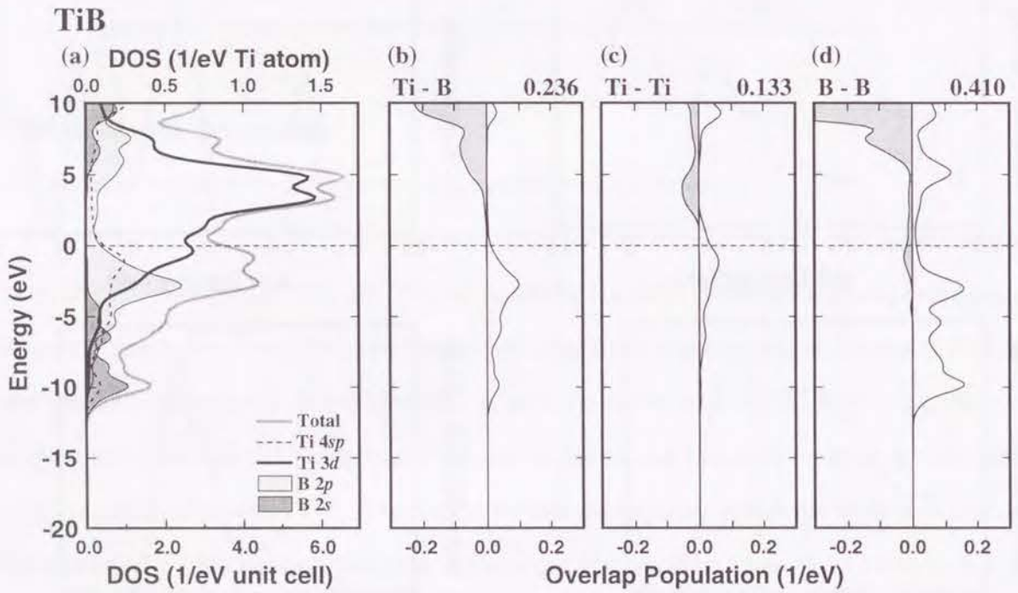

Fig. 3-15 Total and partial density of states and the overlap population diagrams for TiB.
(a) Total and partial density of states
(b) overlap population diagram for the Ti-B bond (c) for the Ti-Ti bond (d) for the B-B bond.

only total DOS and the general feature of total DOS and the position of E_F in this work agree with their result.

In comparison with TiB, a similar overlap between the B-2s and 2p bands, which is the origin of the B-B bond, can be seen. The bottom of the valence band in TiB_2 is stretched to lower energy of -14 eV. The broadness of the valence band is due to the increase of the coordination number of the B atoms, i.e., every B atom in TiB_2 has three nearest neighbor B atoms in graphite-like B layers, but every B atom in TiB has two nearest neighbor B atoms in zigzag B chains. The Ti-B bond is formed in the same way as TiB. The bond overlap population of the Ti-Ti bond written in Fig. 3-16 (c) is an average for the intralayer and interlayer Ti-Ti bonds. The bond overlap population of the intralayer and interlayer Ti-Ti bonds are 0.107 and 0.010, respectively. Although the interlayer Ti-Ti distance is only 7% longer than the intralayer one, the interlayer Ti-Ti bond is much weaker than the intralayer one because of the strong Ti-B bonds formed between the Ti layers. The general feature of our PDOS is agree with the previous calculations by the use of LMTO method [4]. However, there is a discrepancy about the total DOS near E_F. The recent result using LMTO method by Tian *et al.* [5] shows that a pseudogap exists near E_F and the DOS at E_F is very small in spite of metallic behavior of TiB_2. Furthermore, Wang *et al.* [6] calculated the electronic structures of the

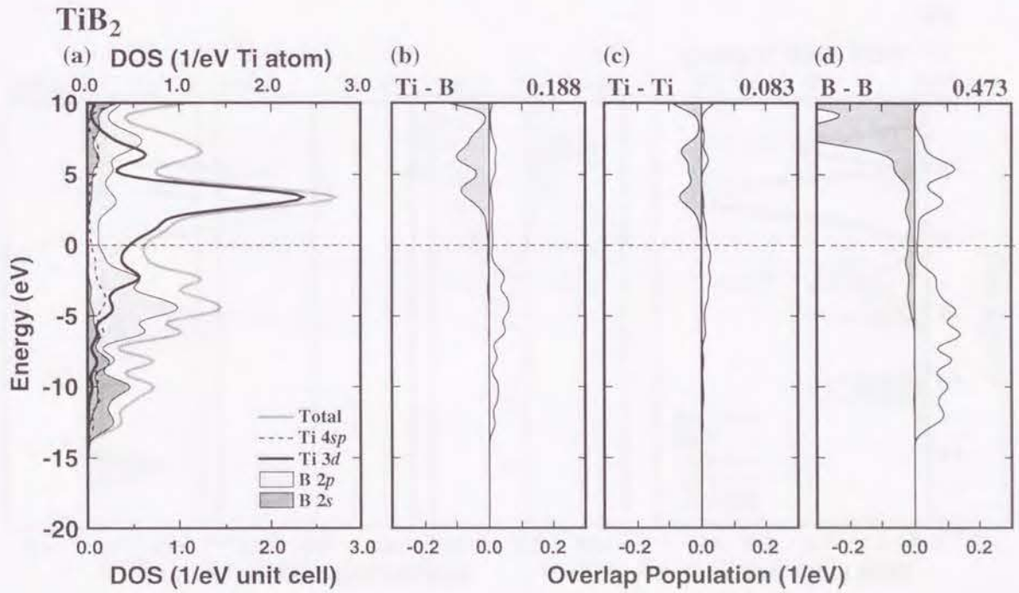

Fig. 3-16 Total and partial density of states and the overlap population diagrams for TiB_2.
(a) Total and partial density of states
(b) overlap population diagram for the Ti-B bond (c) for the Ti-Ti bond (d) for the B-B bond.

AlB_2 type transition-metal diborides using the same method as Tian and found that there was a pseudogap like TiB_2 in the all diborides and concluded that the total DOS of these diborides was characterized by the pseudogap. However, in our present calculations, a pseudogap between the Ti-3d and X-*n*p band can be seen in not TiB_2 but TiC and TiN. According to Pasturel *et al.* [68], which was refereed by Wang *et al.*, a pseudogap arises from strong chemical interactions and is a sing of enhancement of the cohesive energy. As is seen in the overlap population diagram of TiB_2, the B-2p band has bonding contribution to not only the Ti-B bonding but also the B-B and Ti-Ti bondings. Therefore the B-B and Ti-Ti bondings reduce the interaction between the Ti and B atoms. On the other hand, in TiC and TiN, the C-2p and N-2p band have bonding contribution almost only to the Ti-C and Ti-N bondings, respectively. These out results suggests that a pseudogap is not a feature of TiB_2. The feature of DOS near E_F of TiB_2 in this calculation is in better agreement with the suggestion by Pasturel *et al.* and metallic behavior of TiB_2 than that of the previous works using LMTO method.

Several authors have reported a series of calculations for the rock-salt type structure compounds including TiC, TiN and TiO [7-14], TiC and TiN [15-20], TiC and TiO [21,22], TiO [69,70]. Besides, many calculations for TiC have been performed using band-structure calculation [23-27], cluster

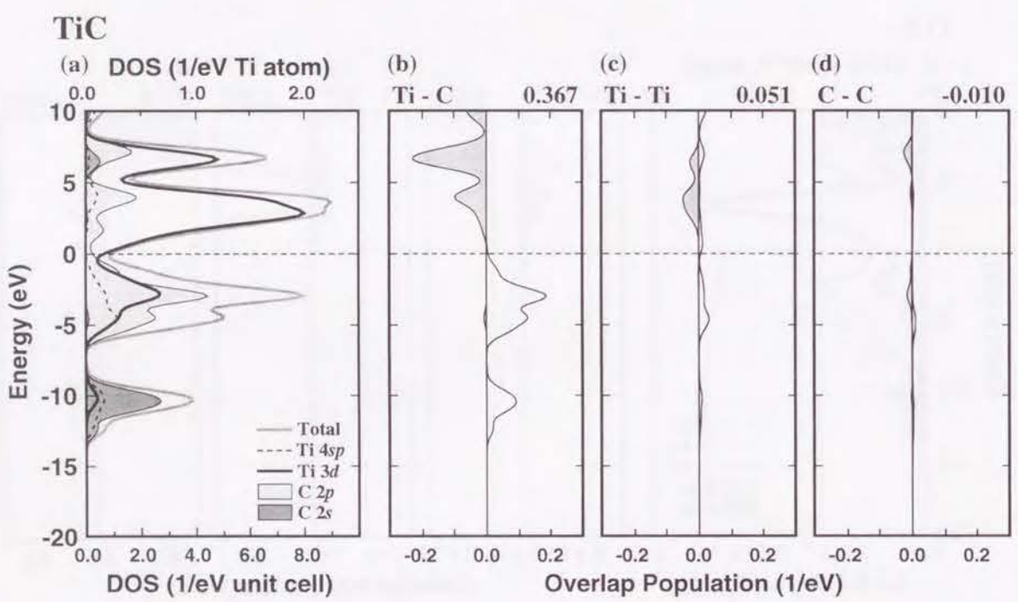

Fig. 3-17 Total and partial density of states and the overlap population diagrams for TiC.
(a) Total and partial density of states
(b) overlap population diagram for the Ti-C bond (c) for the Ti-Ti bond (d) for the C-C bond.

method [28-34] or tight binding calculation [35,36]. Total and partial DOSs of TiC in this work are shown in Fig. 3-17. In TiC, there are two large bands below E_F. The upper band located from -5 to 0 eV is mainly composed of the C-2p orbitals interacting with the Ti 3d, 4s and 4p. The lower band located at about -10 eV is mainly composed of the C-2s orbitals. The component of the Ti-3d, 4s and 4p orbitals in the C-2s band is smaller than that in the C-2p band. These two valence bands have large bonding contribution for the Ti-C bonding. The Ti-3d band above E_F is antibonding for the Ti-C bonding. The Ti-Ti bond shows weak bonding character because of small bonding contribution of the upper valence band.

The shapes of the PDOS in TiN are similar to those in TiC. However comparing with TiC, the components of the Ti-3d,4s and 4p states in the N-2p band are smaller than those in the C-2p band, E_F moves upwards and lies across the lower part of the Ti-3d band which has antibonding contribution to the Ti-N bonding. Because of the decrease of the Ti-3d, 4s and 4p components in the N-2p band and the occupation of the antibonding orbitals in the Ti-3d band, the Ti-N bond is weaker than the Ti-C bond. Ti_2N is only one Ti_2X compound in present calculations. The Ti-3d band in Ti_2N is broader than that in TiN, which indicates that the Ti-Ti interaction in Ti_2N is stronger than that in TiN. Therefore, the Ti-Ti bond in Ti_2N is three times as strong as that in TiN. The local structure

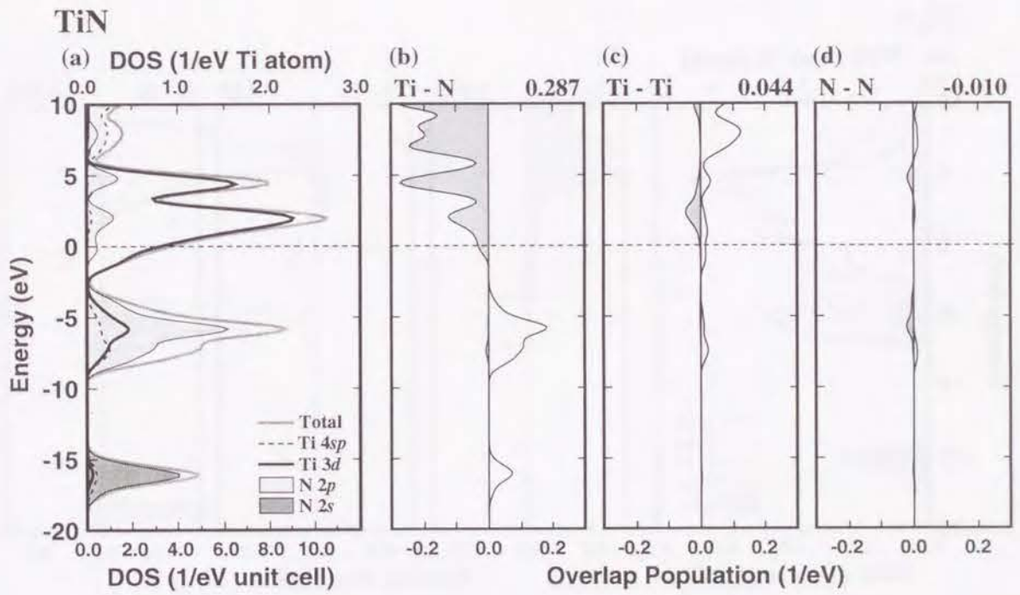

Fig. 3-18 Total and partial density of states and the overlap population diagrams for TiN.
(a) Total and partial density of states
(b) overlap population diagram for the Ti-N bond (c) for the Ti-Ti bond (d) for the N-N bond.

around the N atoms in Ti_2N, the distorted octahedron, is similar to that in TiN. The occupation of the Ti-3d band in Ti_2N is lager than that in TiN, while the antibonding contribution of the Ti-3d band to the Ti-N bonding is still small because of the small magnitude of the antibonding component. Therefore, the Ti-N bond in Ti_2N is as strong as that in TiN.

In TiO, the O-2p band is located at -10 eV and there is a clear separation between the Ti-3d and O-2p band. Comparing the O-2p band with the X-2p in the other compounds, the component of the Ti-3d, 4s and 4p orbitals in the O-2p band is very small. Therefore, the covalent interaction for the Ti-O bonding is much smaller than that for the Ti-C or Ti-N bonding. The O-2s band located at -23 eV has small antibonding contribution for the Ti-O bonding because of the repulsive interaction between the O-2p and Ti-3p orbitals. The Ti-3d band located above E_F has antibonding contribution to the Ti-O bonding. The antibonding nature of the Ti-3d band for the Ti-X bonding is the common feature in the compounds with the second-row elements. However, the antibonding orbitals are empty in TiB, TiB_2 and TiC and nearly empty in Ti_2N and TiN. Therefore it has no significant contribution to the Ti-X bonding. In the case of TiO, it is partially occupied and reduces the strength of the Ti-O bonding.

It is well know that TiC and TiN contain C and N vacancies, respectively. On the other hand,

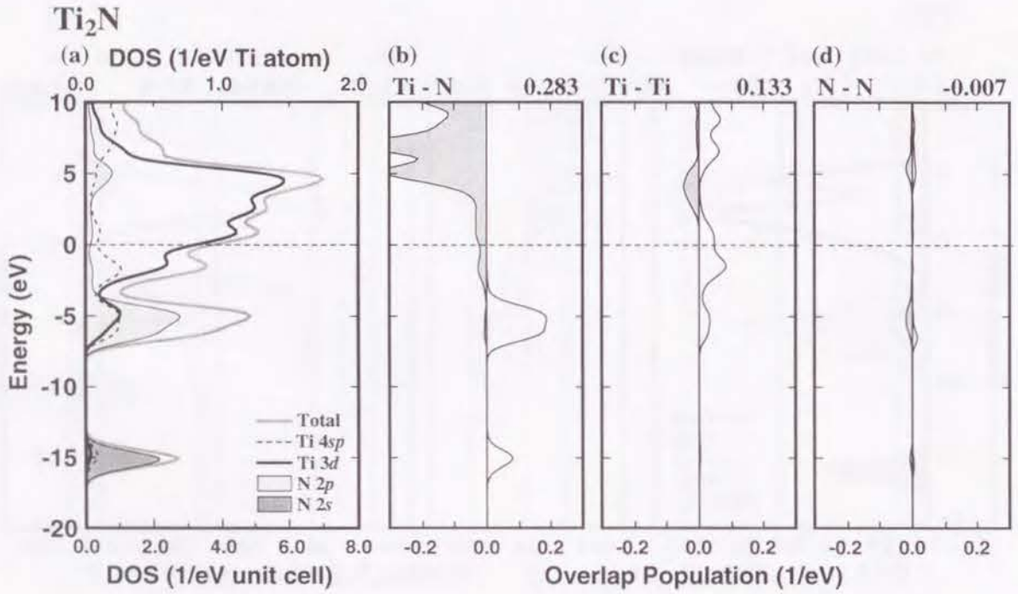

Fig. 3-19 Total and partial density of states and the overlap population diagrams for Ti_2N.
(a) Total and partial density of states
(b) overlap population diagram for the Ti-N bond (c) for the Ti-Ti bond (d) for the N-N bond.

TiO_x can be formed with $0.8<x<1.3$ containing vacancies both at Ti and O sites. In many theoretical works for TiC, TiN or TiO [10,12,13,17,19,22,25-27,31,33,35,71-77], the question of the vacancy in these compounds were discussed. Several theoretical works were successful in interpretation of experimental spectrum of non-stoichiometric TiC, TiN or TiO using the calculated DOS [12,17,19,22,25,27,31,71,72,77]. With respect to the chemical bonding in the non-stoichiometric compounds, several authors pointed out the importance of the Ti-Ti bonds around the vacancy [10,12,13,22,25-27,35,73,76]. While the importance of the Ti-Ti bond is widely accepted, it is still an unsettled question whether the Ti-Ti bonds around the vacancy can compensate the loss of the Ti-X bonds. Our results for stoichiometric TiC, TiN and TiO can not be used to quantitative discuss about the change of the chemical bonding induced by the vacancy. However, the overlap population diagram is applicable to discuss the difference of the nature of the vacancy between TiC, TiN and TiO qualitatively. In TiC and TiN, the Ti vacancy induces the loss of the covalent bonding of Ti-X and Ti-Ti bonds, but forms no new covalent bondings, because the C-C distance is too long. In TiO, the loss of the covalent bonding of the Ti-O bond is much smaller than that of the Ti-C or Ti-N bonds. Furthermore, because E_F moves downward with increase of the Ti vacancy, the decrease of the occupation of Ti-3d band makes the Ti-Ti bond weak, but the Ti-O bond become stronger

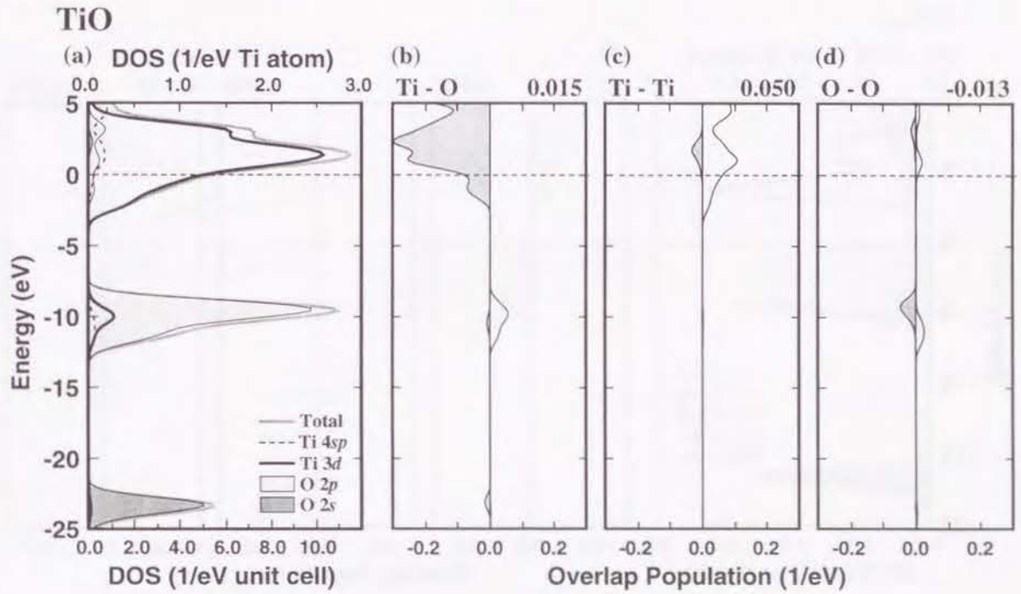

Fig. 3-20 Total and partial density of states and the overlap population diagrams for TiO.
(a) Total and partial density of states
(b) overlap population diagram for the Ti-O bond (c) for the Ti-Ti bond (d) for the O-O bond.

because of the decrease of the antibonding contribution in Ti-3d band. Therefore, the loss of the covalent bondings induced by the Ti vacancy in TiO is smaller than that in TiC or TiN. This view seems to be one of the reason why the Ti vacancy can be introduced in TiO.

With respect to TiO_2, there are two very early theoretical works [78,79] and more than ten theoretical calculations have been performed in a decade [80-92]. The PDOS of TiO_2 in present calculation shows that the Ti-3d band above E_F is completely unoccupied. The O-2p band is located from -6 to 0 eV and broader than that in TiO. The lowest valence band at -16 eV is the O-2s band. These features for PDOS agree with recent theoretical works. Although TiO_2 is generally considered as an ionic compound, there is Ti components in the O-2p band which is a sign of the covalent interaction between the Ti and O. Some authors pointed out a covalent character in the Ti-O bond because of the significant interaction between the Ti and O in the valence band [84,86,87]. In comparison with TiO, there is no occupation of the antibonding orbitals of the Ti-3d band. However, the antibonding contribution in the O-2s or 2p bands established by the Ti-3p - O 2s and p interaction reduces the Ti-O covalent bonding. Therefore, the Ti-O bond is quite weaker than the Ti-X bond in the other compounds.

The general features of PDOS in TiSi and $TiSi_2$ are similar to those in TiB and TiB_2, i.e., there

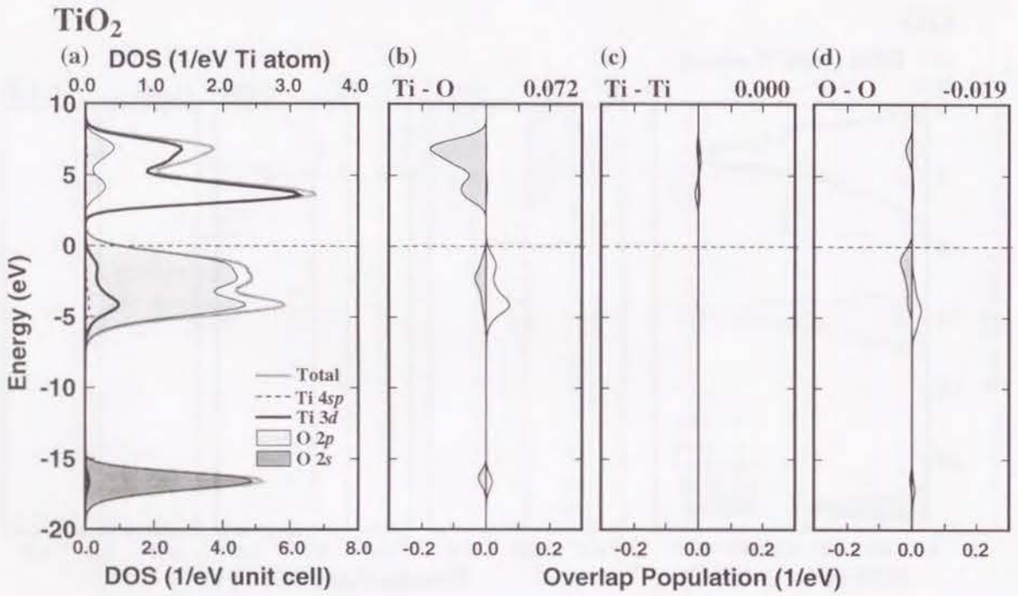

Fig. 3-21 Total and partial density of states and the overlap population diagrams for TiO_2.
(a) Total and partial density of states
(b) overlap population diagram for the Ti-O bond (c) for the Ti-Ti bond (d) for the O-O bond.

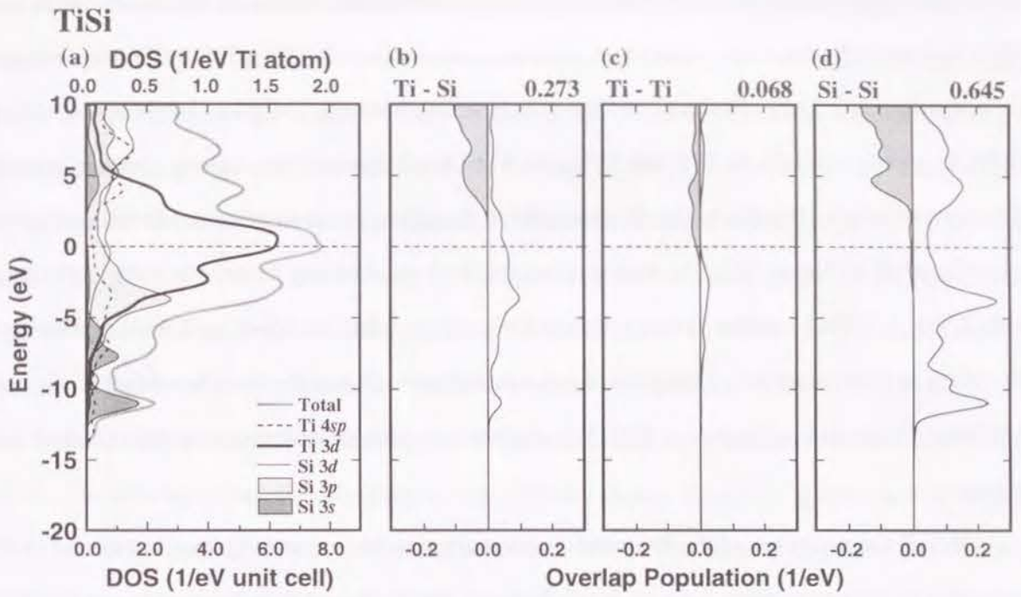

Fig. 3-22 Total and partial density of states and the overlap population diagrams for TiSi.
(a) Total and partial density of states
(b) overlap population diagram for the Ti-Si bond (c) for the Ti-Ti bond (d) for the Si-Si bond.

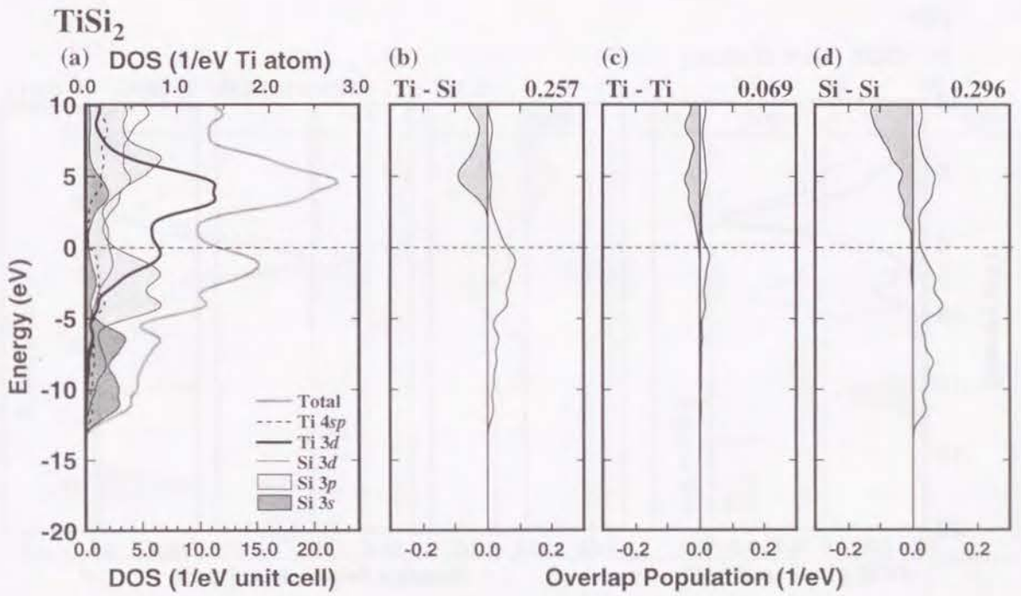

Fig. 3-23 Total and partial density of states and the overlap population diagrams for $TiSi_2$.
(a) Total and partial density of states
(b) overlap population diagram for the Ti-Si bond (c) for the Ti-Ti bond (d) for the Si-Si bond.

is no separation in the valence band and an overlap between Si-3s and Si-3p bands can be seen. These features agree with previous band structure calculations for $TiSi_2$ [50,93-95]. Regarding the Ti-Si bonding, the Ti-Si covalent bonding mainly arises from the Si-2p band interacting with the Ti-3d, 4s and 4p orbitals. In TiSi and $TiSi_2$, the Si-Si bond displays very strong covalent bonding. However, although $TiSi_2$ has higher Si composition than TiSi, the strength of the Si-Si bond in $TiSi_2$ is less than half of that in TiSi. The reason is that the Si-Si neighboring distance in $TiSi_2$ is distributed from 2.533 to 2.794Å and the value of the bond overlap population of Si-Si in $TiSi_2$ is an average of the values at these distances. Therefore, it is a mistake to think that the Si-Si bond in $TiSi_2$ is not so dominant chemical bonding as in TiSi. We shall discuss this point later using the covalent bond density.

In TiP, the positions of the P-3p and 3s band are similar to that of C-2p and 2s band in TiC, respectively. However, there is no clear gap between the Ti-3d and P-3p band as is seen in TiC or TiN. The strong Ti-P bond is formed by the interaction between the P-3s and 3p and the Ti-3d, 4s and 4p orbitals. E_F is located across the lower part of the Ti-3 band. The Ti-3d band around E_F still has bonding contribution to the Ti-P bond, but almost no contribution to the Ti-Ti bond.

The band structure of TiS has been calculated using KKR method by J. Nakahara *et al.* [96]

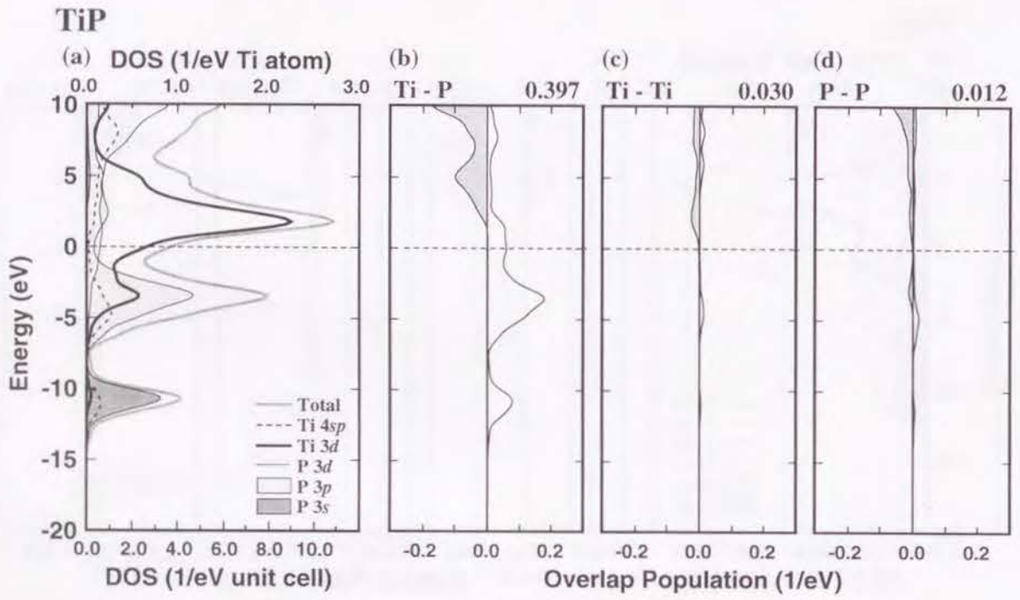

Fig. 3-24 Total and partial density of states and the overlap population diagrams for TiP.
(a) Total and partial density of states
(b) overlap population diagram for the Ti-P bond (c) for the Ti-Ti bond (d) for the P-P bond.

and many electronic structure calculations for TiS_2 have been performed using band structure or cluster calculations [37-48]. In TiS, the S-3p band is located from -9 to -3 eV and interacts with the Ti-3d, 4s and 4p orbitals. The lowest band around -15 eV is the S-3s band slightly interacting the Ti-3d, 4s and 4p orbitals. E_F is located in the lower part of the Ti-3d band. The Ti-S bond displays strong covalent bonding which arises from the S-3p and 3s bands interacting with the Ti 3d, 4s and 4p. In TiS_2, the S-3p and 3s band are located from 0 to -6 eV and from -10 to -15 eV, respectively. E_F is lying at a minimum in the DOS between the Ti-3d and S-3p band. These features for DOS agree with previous works. Regarding the Ti-S bond, several authors [38,39,41,45,48] pointed out that from PDOS or charge distributions there was strong covalent bonding between the Ti and S atoms. The overlap population diagram in Fig. 3-26 (b) shows that the Ti-S bond in TiS_2 displays strong covalent bonding. The bond overlap population of the Ti-S bond is largest in the Ti-X bond in the all compounds. Every S atom in TiS_2 has only three Ti atoms, but the X atoms in the other compounds have more than five Ti atoms. Therefore, the bond overlap population, which is a measure of the covalent bond strength of the single bond, becomes large value for the Ti-S bond in TiS_2. The bond overlap population of the S-S bond written in Fig. 3-26 (d) is the average value for all types of the S-S bond. The bond overlap population of the intralayer S-S bond is 0.017. That of

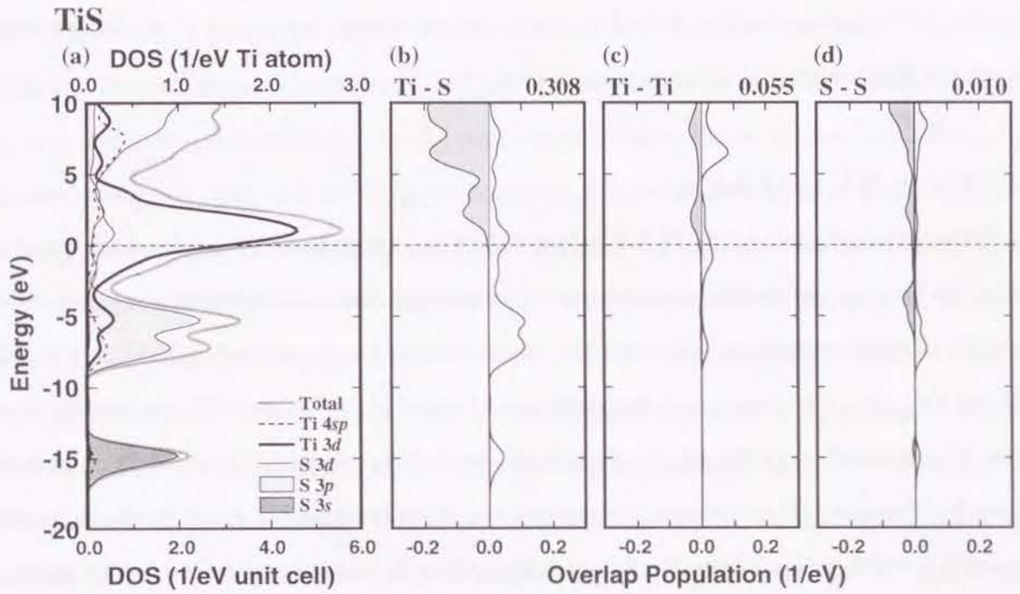

Fig. 3-25 Total and partial density of states and the overlap population diagrams for TiS.
(a) Total and partial density of states
(b) overlap population diagram for the Ti-S bond (c) for the Ti-Ti bond (d) for the S-S bond.

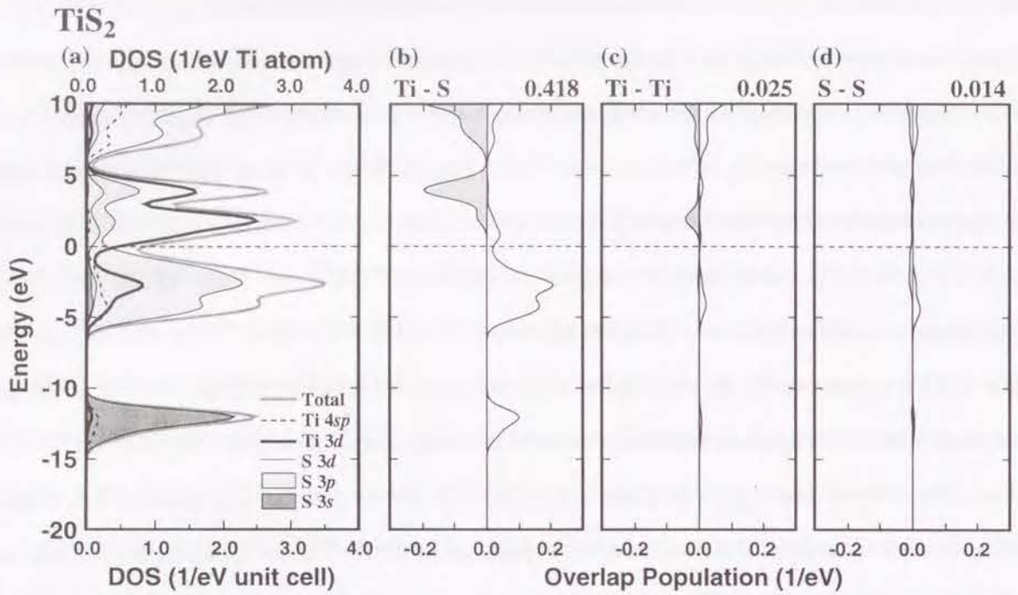

Fig. 3-26 Total and partial density of states and the overlap population diagrams for TiS_2.
(a) Total and partial density of states
(b) overlap population diagram for the Ti-S bond (c) for the Ti-Ti bond (d) for the S-S bond.

the interlayer S-S bond without the Ti layers is 0.025 and that of the interlayer S-S bond across the Ti layers is slightly negative value of -0.003. However, this negative value is not significant because the strong Ti-S bond are formed. Therefore, the covalent bonding between the Ti and S layer is very strong, but that between the S layers is quite weak.

3.5.3 he Ti-X, Ti-Ti and X-X bonding

The general feature of the Ti-X bonding in the Ti compounds with the second-row elements is that the bonding and antibonding band are separated and there is non-bonding region between them. E_F of these compounds is located between the bonding and antibonding band in TiB, TiB_2, TiC and TiO_2 or at the lower part of the antibonding band in Ti_2N, TiN and TiO. On the other hand, in the Ti compounds with the third-row elements, the Ti-X bonding band is broader and stretched above E_F. Therefore, E_F is located crossing the top of the bonding band and bonding character around E_F is still bonding. Generally, E_F moves upwards with rising atomic number of the transition metal in these compounds. From the change of the occupation of bonding and antibonding orbitals, it is expected that across the series of the 3d transition metal (TM) compounds with the second-row

elements, the strength of the TM-X bond is decreased because of the increase of the occupation of the antibonding orbitals. On the other hand, across the series of 3d transition metal compounds with the third-row elements, it is expected that the TM-X bond becomes stronger because of the increase of the occupation of the bonding orbitals and at the latter part of the series, with beginning of the occupation of antibonding orbitals, the TM-X bond becomes weaker. Actually, Takao *et al.* [95] made first-principles molecular orbital calculations for transition metal disilicides using DV-Xa method with model clusters composed of about 20 atoms and found that the strength of TM-Si bond increased with rising atomic number of TM from Sc to Co and decreased at Ni. But their results also show that the change of the bond overlap population is due to not only the change of the occupation of bonding and antibonding orbitals but also the change of the magnitude of bonding and antibonding components. For the systematic calculations throughout the series in Periodic Table, the estimation from the overlap population diagram gives us the trend of the chemical bonding. However, in order to discuss more quantitatively, it is necessary to perform the calculation.

It is generally considered that an overlap of the PDOS indicates the covalent interaction. In most of the titanium compounds studied here, PDOS shows that the Ti-3d orbitals strongly interact with the X-*n*p band but the component of Ti-4s and 4p orbitals in the X-*n*p band is less than half as small as that of the Ti-3d. These features agree with previous works concluding that the origin of the Ti-X bonding is the strong interaction between the Ti-3d and X-*n*p orbitals. The overlap populations for valence orbitals between the Ti and X atoms are presented in Table 3-2 and 3-3. As is pointed out in several works, the overlap populations between the Ti-3d and X-*n*p orbitals are quite large. However, although the Ti-4p component in X-*n*p band is not so large as the Ti-3d, the overlap populations between the Ti-4p and X-*n*p orbitals are as large as those between the Ti-3d and X-*n*p orbitals. The overlap population between two orbitals defined by equation (2-9) can be obtained by the product of coefficients of two orbitals and the overlap integral between two orbitals defined by equation (2-7). The overlap of PDOS is related to the magnitude of the coefficients, but the overlap integrals represent the spatial overlap between two orbitals and are independent of the overlap of PDOS. As an example, the overlap integrals between the Ti and C atom in TiC are presented in Table 3-4. The overlap integrals between the Ti-4p and C-2p is twice as large as that between the Ti-3d and C-2p. Consequently, the overlap population between the Ti-4p and X-*n*p is quite large in spite of the small overlap in PDOS. Therefore, it is not always true to estimate the

Table 3-2 Overlap populations of the Ti-X bond for valence orbitals in the titanium compounds with the second-row elements.

	Ti - X 2s			Ti - X 2p		
	3d-2s	4s-2s	4p-2s	3d-2p	4s-2p	4p-2p
TiB	0.036	0.018	0.052	0.104	0.048	0.099
TiB_2	0.020	0.008	0.026	0.068	0.025	0.059
TiC	0.032	0.019	0.052	0.142	0.053	0.107
Ti_2N	0.035	-0.001	0.030	0.141	0.045	0.086
TiN	0.022	0.012	0.036	0.112	0.051	0.101
TiO	0.009	0.005	-0.004	0.058	0.024	0.013
TiO_2	0.009	0.004	0.003	0.103	0.015	0.022

Table 3-3 Overlap populations of the Ti-X bond for valence orbitals in the titanium compounds with the third-row elements.

	Ti - X 3s			Ti - X 3p			Ti - X 3d		
	3d-3s	4s-3s	4p-3s	3d-3p	4s-3p	4p-3p	3d-3d	4s-3d	4p-3d
TiSi	0.018	0.009	0.028	0.065	0.035	0.068	0.041	0.009	0.020
$TiSi_2$	0.021	0.009	0.026	0.063	0.033	0.062	0.037	0.008	0.059
TiP	0.020	0.016	0.042	0.112	0.061	0.114	0.047	0.003	0.010
TiS	0.014	0.003	0.012	0.090	0.056	0.090	0.051	0.005	0.015
TiS_2	0.008	0.007	0.026	0.143	0.073	0.143	0.032	0.005	0.013

Table 3-4 Overlap integrals for valence orbitals between Ti and C atoms in TiC.

TiC	Ti-3d	Ti-4s	Ti-4p
C-2s	0.048	0.082	0.134
C-2p	0.174	0.157	0.334

interaction between orbitals by using the overlap in PDOS. In titanium compounds studied in this work, the strong Ti-X bond arises from the interaction of not only the Ti-3d - X-*n*p but also the Ti-4p - X-*n*p orbitals.

The Ti-Ti bond is weak in the all compounds studied. Even the highest value of the bond overlap population, 0.133, in TiB and Ti_2N, is about as half as that of metal Ti, 0.240, in spite of almost the same Ti-Ti distance. Therefore, the chemical bonding can not be estimate by only bond distances even for the same type bond. The PDOSs show that the *n*p-band of X atoms interacts with the Ti-3d, 4s and 4p orbitals and the overlap population diagrams show that the *n*p-band of X atoms have larger bonding contribution to the Ti-X bonding than the Ti-Ti bonding. Consequently, the Ti-3d, 4s and 4p orbitals in the *n*p-band of X atoms contribute to the Ti-X bonding and this Ti-X interaction reduces the Ti-Ti interaction.

The X-X bond is significant in TiB, TiB_2, TiSi and $TiSi_2$. These strong bonding can be expected from their bond distancs. Namely, the X-X distances in TiB, TiB_2 and TiSi are close to the covalent X-X distance and nearest Si-Si distance in $TiSi_2$ is only 10% longer than Si-Si covalent distance. On the other hand, the X-X distances in other compounds are more than twice longer than the covalent X-X distance. The common feature of PDOS in these silicides and borides is the interaction between valence s and p orbitals of the B or Si atoms which is origin of the strong B-B or Si-Si bondings. Therefore, there is no separation which can be seen between s and p bands ofthe B and S atoms in the valence band of other compounds.

3.5.4 Net charge

The net charges of the Ti and X atoms around the center of the model clusters for all the Ti compounds are plotted in Fig. 3-27. Comparing the net charges among the compounds with the same stoichiomety, the net charge is increased with rising atomic number of the X atoms in the second or third-row elements. This results agree with expectation from their electronegativities. As seen in the PDOSs of these compounds, the positions of the X-*n*s and *n*p bands are moved downward with rising the atomic number of the X atoms in the second or third-row elements. Besides, with rising the atomic number, the decrease of the component of Ti-3d, 4s and 4p orbitals in the X-*n*s and *n*p band can be seen. These results indicate that the nature of the chemical bonding between the Ti-X bonding changes from covalent to ionic in the series of borides to oxides or in the series of

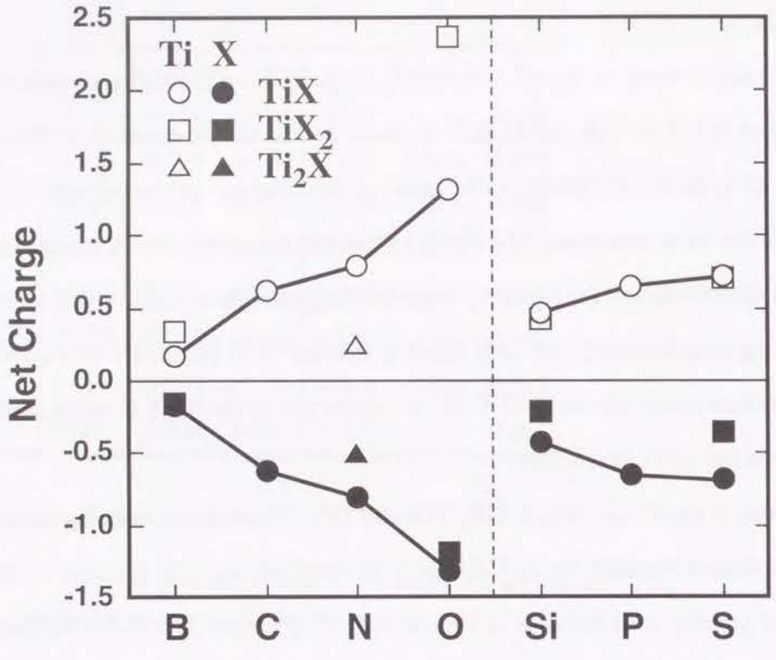

Fig. 3-27 Net charges for all model clusters studied in this work as a function of the atomic number of the second or third-row elements. Open marks denote the net charge of Ti and filled marks denote X atom (X=B, C, N, O, Si, P or S).

silicides to sulfides. In this work, only in the case of TiO and TiO_2 which are considered ionic compounds the model clusters were embedded in Madelung potential generated by approximately 5,000 point charges and the net charges of the Ti atom obtained from the model clusters for TiO and TiO_2 are 1.32 and 2.38, respectively. In order to estimate the influence of Madelung potential, we have performed the calculation of the TiO and TiO_2 using neutral model clusters without the Madelung potential and obtained almost the same value of the net charge as that with Mardelung potential, i.e. 1.28 for TiO and 2.29 for TiO_2. This result suggests that the model clusters employed in present calculations are large enough to calculate the electronic structure of the bulk compounds without point charges for Madelung potential around the model clusters.

3.5.5 Bond overlap population and covalent bond density

The bond overlap population and the covalent bond density of the Ti-X, Ti-Ti and X-X bonds in all compounds studied in this work are shown in Fig. 3-28 and 3-29, respectively. The bond overlap population represents the strength of the covalent bonding between atoms. However the covalent bond density, which the strength and the number of the bonds are taken into account on, gives us the strength of the covalent bonding in the unit volume. A clear difference between the bond overlap population and the covalent bond density can be seen on the X-X bonds in TiB, TiB_2, TiSi and $TiSi_2$. The bond overlap population of B-B and Si-Si bonds in these compounds are larger than that of the Ti-B and Ti-Si bonds, respectively. Especially, in TiSi, the bond overlap population of the Si-Si bond is about three times greater than that of the Ti-Si bond. However, since the number of the Ti-X, Ti-Ti and X-X is not equal to each other, the strongest bond is not always dominant chemical bonding in compounds. Burdett *el al.* [3] found the strong B-B bond was formed in TMB_2 and the strength of the B-B bond increased with rising the atom number of TM. However, their

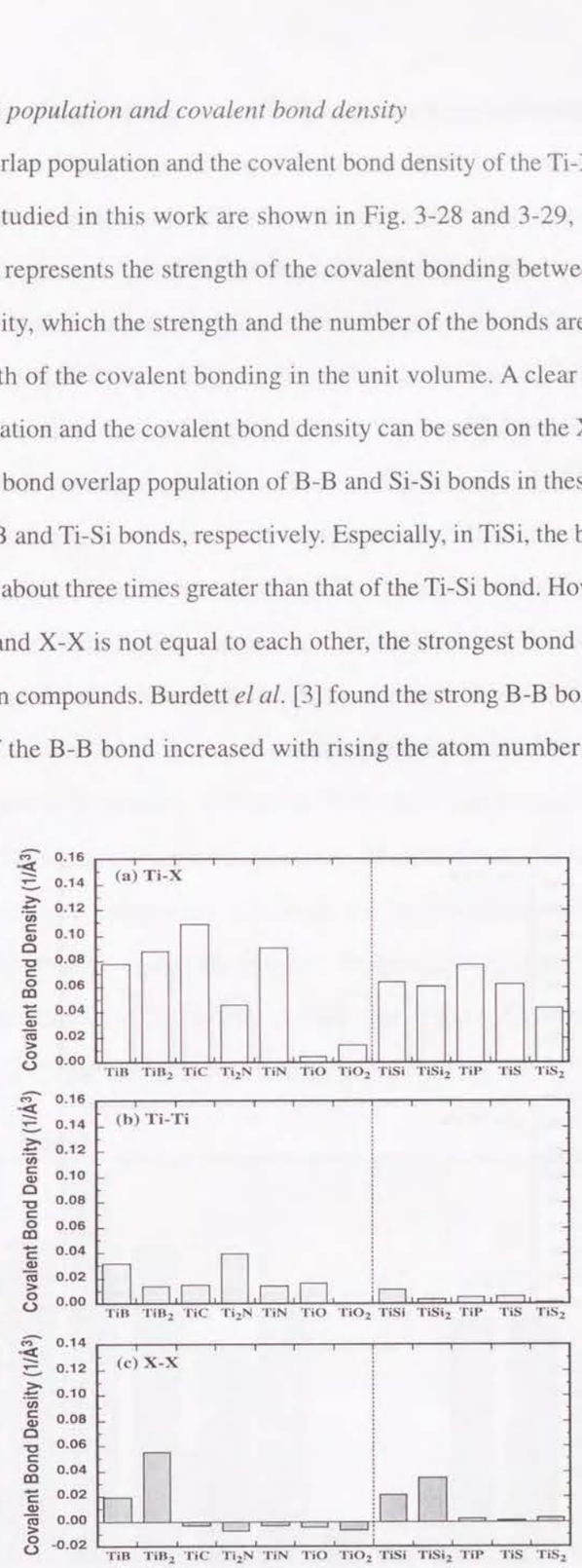

Fig. 3-28 Bond overlap populations for all model clusters studied in this work.
(a) for the Ti-X bond (b) for the Ti-Ti bond (c) for the X-X bond (X=B, C, N, O, Si, P or S).

calculated variation in the stabilization energy of TMB_2 was explained by the occupation of bonding or antibonding orbitals for the TM-B bonding. The orbitals occupied from Ti to the right in 3d transition metal series are antibonding character for the TM-B bonding, but bonding character for the B-B bonding. These results suggest that although the B-B bond is stronger than the TM-B bond, the TM-B bond is more dominant in the stabilization of TMB_2 than the B-B bond. As seen in Table 3-1, the number of the B-B or Si-Si bond in the unit cell of TiB, TiB_2, TiSi and $TiSi_2$ is quite smaller than that of Ti-B or Ti-Si bond. Therefor, the covalent bond densities of these borides and silicides show that the Ti-B and Ti-Si bonds are more dominant for their stability than the B-B and Si-Si bonds, respectively. The similar difference between the bond overlap population and the covalent bond density can be seen for the Ti-S bond in TiS_2. The bond overlap population of the Ti-S bond in TiS_2 is the largest in the Ti-X bonds. However, the number of Ti-S bond in the unit volume is the smallest as seen in Table 3-1. Consequently, the covalent bond density of the Ti-S bond is not so large in spite of the largest bond overlap population.

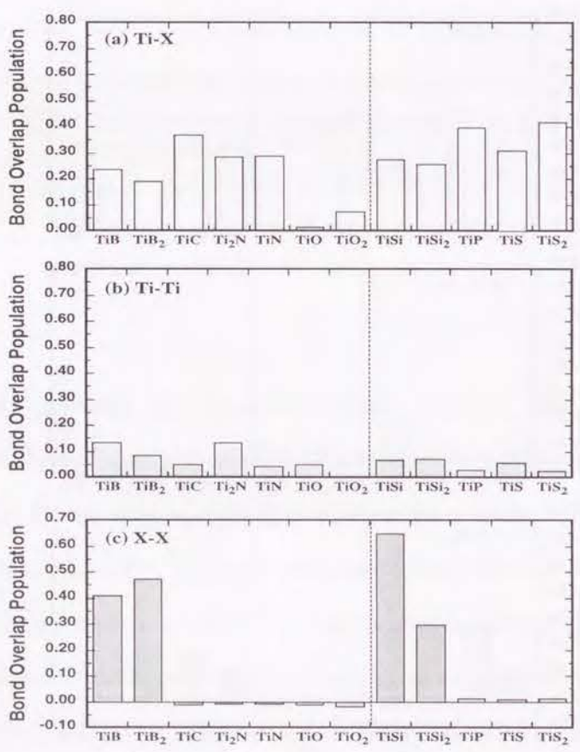

Fig. 3-29 Covalent bond densities for all model clusters studied in this work.
(a) for the Ti-X bond (b) for the Ti-Ti bond (c) for the X-X bond (X=B, C, N, O, Si, P or S).

Comparing the Si-Si bond in TiSi and $TiSi_2$, the bond overlap population indicates that the Si-Si bond in TiSi is more than twice stronger than that in $TiSi_2$, but the covalent bond density is opposite. In TiSi, there is one nearest neighbor distance of 2.216Å and in $TiSi_2$ neighboring distance are distributed in the range of 2.533 to 2.794Å. Therefore the bond overlap population in TiSi is larger because of the shorter nearest neighbor distance. However, with respect to the number of the Si-Si bonds in the unit cell volume presented in Table 3-1, the value of 0.1179/Å^3 in $TiSi_2$ is about three times as large as the value of 0.0336/Å^3 in TiSi. Consequently, the covalent bond density of the Si-Si bond in $TiSi_2$ is larger than that in TiSi, which agrees with what is expected from the composition of Si.

From electronegativities of the elements studied here, X (X=B, C, N and O in the second-row; Si, P and S in the third-row), the nature of the chemical bonding between Ti and X is expected to change from covalent to ionic across the second and third-row series. However the change of the bond overlap population of the Ti-X bond does not correspond to this view of the chemical bonding, because the Ti-Ti and X-X bonds as well as the Ti-X bond contribute to the chemical bonding in these compounds. In order to estimate the covalency of compounds, it is necessary to take account of all types of the bonds in compounds. The bond overlap populations of the Ti-X, Ti-Ti and X-X bonds can not be summed up each other, because the bond overlap population represents only the strength of the single bond and the number of each type of the bonds is different. However, since

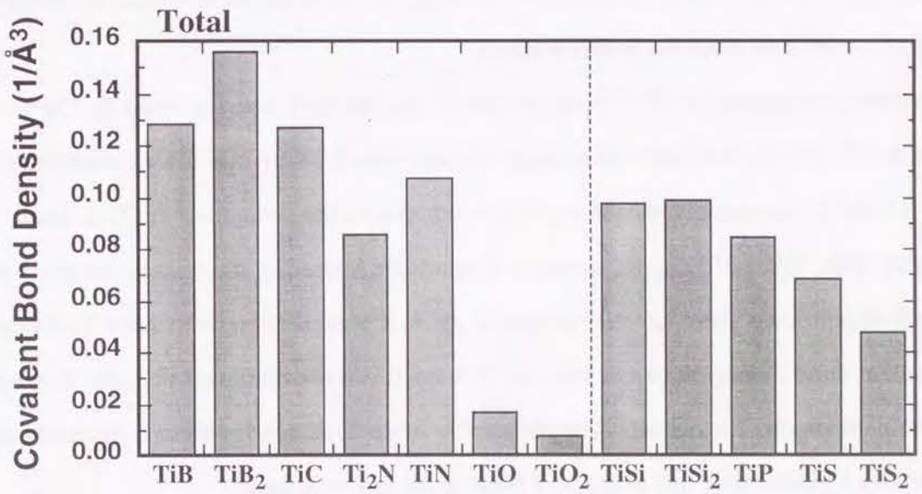

Fig. 3-30 Total covalent bond densities for all model clusters studied in this work.

the value of the covalent bond density is normalized by the unit volume of 1Å^3, the total covalent bond density can be evaluated by summing up the covalent bond densities of the Ti-X, Ti-Ti and X-X bonds. The total covalent bond density of all compounds studied in this work is shown in Fig. 3-30. Across the series of the compounds with the second or third-row elements, the total covalent bond density is decreased. This result suggests that the covalency of these titanium compounds corresponds to simple expectation of the interaction between Ti and X atoms from their electronegativities. The total covalent bond density of TiB_2 and TiC shows that the covalency of TiB_2 or TiC is higher than other compounds and their high covalency seems to be related to their high hardness or high melting point.

3.6 Conclusion

We have performed the first principles molecular orbital calculations using model clusters in order to study the chemical bonding of titanium compounds with the second and third-row elements. Furthermore, the covalent bond density has been applied to comparison the contribution of the Ti-X, Ti-Ti and X-X bonds to the covalent bonding among the compounds with different crystal structures. Main results can be summarized as follows:

(1) The dominant covalent bonding in titanium compounds studied in this work is the Ti-X bond without TiO. The Ti-X bond mainly arises from the interaction of not only the Ti-3d - X-*n*p but also the Ti-4p and X-*n*p states. The Ti-X bonding character around E_F in the compounds with the second-row elements is almost non-bonding. On the other hand, that in the compounds with the third-row elements is still bonding.

(2) In all the compounds, the Ti-Ti bond is quite weaker the Ti-Ti bond in metal Ti. The reason is that the Ti-3d, 4s and 4p orbitals strongly interact with the X-*n*p orbitals and contribute to the Ti-X bond. Consequently, the strong Ti-X bond reduces the strength of the Ti-Ti bond.

(3) In TiB, TiB_2, TiSi and $TiSi_2$, the strong X-X bonds are formed by the strong interaction among the X-*n*s and X-*n*p. Although the strength of the X-X bond is stronger than the Ti-X bond, the covalent bond density indicates that the Ti-X bond is more dominant than the X-X bond in these compounds. The reason is that the number of the Ti-X bond in these compounds is more than twice greater than that of the X-X bond in the unit volume.

(4) The charge transfer occurs from the Ti to X atom in all the Ti compounds. Comparing the net charges number of Ti-S bond in the unit volume is smallest as seen in Table 3-1. Consequently, the covalent bond density of the Ti-S bond is not so large in spite of the largest bond overlap population.

(5) Considering only the interaction between Ti and X atoms, the Ti-X bonding character is expected to change from covalent to ionic and the covalent bond strength decreases with rising the atomic number of X atoms. However, the bond overlap population and covalent bond density of the Ti-X bond do not monotonously decreases across the second or third-row series, because the Ti-Ti and X-X interaction also exist. The total covalent density which is the sum of the covalent bond densities of the Ti-X, Ti-Ti and X-X bonds shows monotonous decrease across the second or third-row series. This result suggests that the covalency of these titanium compounds corresponds to simple expectation of the interaction between Ti and X atoms from their electronegativities.

References

[1] P. G. Perkins and A. V. Sweeney, *J. Less-Common Metals* **47**, 165 (1976)

[2] D. R. Armstrong, *Theoret. Chim. Acta* **64**, 137 (1983).

[3] J. K. Burdett, E. Canadell and G. J. Miller, *J. Am. Chem. Soc.* **108**, 6561 (1986).

[4] V. M. Anishchik and N. N. Dorozhkin, *Phys. Stat. Sol. B* **160**, 173 (1990).

[5] D. C. Tian and X. B. Wang, *J. Phys., Condens. Matter.* **4**, 8765 (1992).

[6] X. B. Wand, D. C. Tian and L. L. Wang, *J. Phys., Condens. Matter.* **6**, 10185 (1994).

[7] V. Ern and A. C. Switendick, *Phys. Rev* **137**, A1927 (1965).

[8] V. A. Gubanov, E. Z. kurmaev and G. P.Shveikin, *J. Phys. Chem. Solids* **38**, 201 (1977).

[9] A. Neckel, P. Rastl, R. Eibler, P. Weinberger and K. Schwarz, *J. Phys. C* **9**, 579 (1976).

[10] A. L. Ivanovsky, V.A. Gubanov, G. P. Shveikin and E. Z. Kurmaev, *J. Less-Common Metals* **78**, 1 (1981).

[11] L. M. Sheludchenko, Y. N. Kucherenko and V. G. Aleshin, *J. Phys. Chem. Solids* **42**, 733 (1981).

[12] A. L. Ivanovsky, V. I. Anisimov, D. L. Novikov, A. I. Lichtenstein and V. A. Gubanov, *J. Phys. Chem. Solids* **49**, 465 (1988).

[13] V. P. Zhukov, V. A. Gubanov, O. Jepsen, N. E. Christensen and O. K. Andersen, *J. Phys. Chem. Solids* **49**, 841 (1988).

[14] S. Kim and R. S. Williams, *J. Phys. Chem. Solids* **49**, 1307 (1988).

[15] L. I. Johansson, P. M. Stefan, M. L. Shek and A. Nørlubd Christensen, *Phys. Rev. B.* **22**, 1032 (1980).

[16] H. Obara, Y. Endoh, Y. Ishikawa and T. Komatsubara, *J. Phys. Soc. Japan* **49**, 928 (1980).

[17] P. Marksteiner and P. Weinberger, *Phys. Rev. B* **33**, 812 (1986).

[18] A. L. Ivanovsky, V. I. Anisimov, A. I. Lichtenstein and V. A.Gubanov, *J. Phys. Chem. Solids* **49**, 479 (1988).

[19] V. A. Pai, A. P. Sathe and V. R. Marathe, *J. Phys., Condens. Matter.* **2**, 9363 (1990).

[20] A. G. Nargizyan and S. N. Rashkeev, *Z. Phys. B, Condens. Matter* **82**, 217 (1991).

[21] L. M. Huisman, A. E. Carlsson, C. D. Gelatt, Jr. and H. Ehrenreich, *Phys. Rev. B* **22**, 991 (1980).

[22] V. A. Gubanov, A. L. Ivanovsky, G. P. Shveikin and D. E. Ellis, *J. Phys. Chem. Solids* **45**, 719 (1984).

[23] H. Ihara, Y. Kumashiro and A. Itoh, *Phys. Rev. B* **12**, 5465 (1975).

[24] H. R. Trebin and H. Bross, *J. Phys. F: Met. Phys.* **14**, 1453 (1984).

[25] J. Redinger, R. Eibler, P. Herzig, A. Neckel, R Podloucky and E. Wimmer, *J. Phys. Chem. Solids* **46**, 383 (1985).

[26] J. Redinger, R. Eibler, P. Herzig, A. Neckel, R Podloucky and E. Wimmer, *J. Phys. Chem. Solids* **47**, 387 (1986).

[27] V. P. Zhukov and V. A. Gubanov, *J. Phys. Chem. Solids* **48**, 187 (1987).

[28] T. Hori, H. Adachi and S. Imoto, *Trans. JIM* **18**, 31 (1977).

[29] V. A. Gubanov, A. L. Ivanovsky, G. P. Shveikin and J. Weber, *Solid State Commun.* **29**, 743 (1979).

[30] A. L. Ivanovsky, V. A. Gubanov, V. P. Zhukov and G. P. Shveikin, *Phys. Stat. Sol. B* **98**, 79 (1980).

[31] V. A. Gubanov, E. Z. Kurmaev and D. E. Ellis, *J. Phys. C* **14**, 5567 (1981).

[32] J. E. Lowther, *J. Less-Common Metals* **99**, 291 (1984).

[33] J. E. Lowther and A. Andriotis, *J. Phys. Chem. Solids* **48**, 713 (1987).

[34] A. L. Ivanovsky, D. L. Novikov, V. I. Anisimov and V. A. Gubanov, *J. Phys. Chem. Solids* **49**, 487 (1988).

[35] A. H. Cottrell, *Mater. Sci. Technol.* **10**, 22 (1994).

[36] A. H. Cottrell, *Mater. Sci. Technol.* **10**, 788 (1994).

[37] H. W. Myron and A. J. Freeman, *Phys. Rev. B* **9**, 481 (1974).

[38] P. Krusius, J. von Boehm and H. Isomäki, *J. Phys. C* **8**, 3788 (1975).

[39] A. Zunger and A. J. Freeman, *Phys. Rev. B* **16**, 906 (1977).

[40] D. W. Bullett, *J. Phys. C* **11**, 4501 (1978).

[41] H. Isomäki, J. von Boehm and P. Krusius, *J. Phys. C* **12**, 3239 (1979).

[42] P. Krusius, H. Isomäki and J. von Boehm, *J. Phys. C* **12**, 3253 (1979).

[43] H. Isomäki and J. von Boehm, *Physica B & C* **99**, 255 (1980).

[44] S. P. Freidman, V. P. Zhukov and V. A. Gubanov, *Solid State Commun.* **36**, 559 (1980)

[45] C. Umrigar, D. E. Ellis, Ding-Sheng Wang, H. Krakauer and M. Posternak, *Phys. Rev. B* **26**, 4935 (1982).

[46] G. A. Benesh, A. M. Woolley and C. Umirigar, *J. Phys. C* **18**, 1595 (1985).

[47] T. Yamasaki, N. Suzuki and K. Motizuki, *J. Phys. C* **20**, 395 (1987).

[48] J. Dijkstra, C. F. van Bruggen and C. Haas, *J. Phys., Condens. Matter.* **1**, 3280 (1989).

[49] L. Pauling, *J. Amer. Chem. Soc.* **69**, 542. (1947).

[50] P. J. W. Weijs, M. T. Czyżyk , J. C. Fuggle, W. Speier, D. D. Sarma and K. H. J. Buschow, *Z. Phys. B, Condens. Matter.* **78**, 423 (1990).

[51] B. F. Decker and J. S. Kasper, *Acta Cryst.* **7**, 77 (1954).

[52] L. N. Kugai, *Inorg. Mater.* **8**, 669 (1972).

[53] S. Shimada, J. Watanabe, K. Kodaira and T. Matsushita, *J. Materials Sci.* **24**, 2513 (1989).

[54] A. N. Christensen, A. Alamo and J. P. Landesman, *Acta Crystallogr. C* **41**, 1009 (1985).

[55] E. Etchessahar, J. P. Bars and J. Debuigne, *J. Less-Common Metals* **134**, 123 (1987).

[56] D. Taylor, *Trans. J. Br. Ceram. Soc.* **83**, 5 (1984).

[57] C. J. Howard, T. M. Sabine and F. Dickson, *Acta Crystallogr. B* **47**, 462 (1991).

[58] V. N. Gurin, Z. P. Terentéva, I. R. Kozlova and A. P. Obukhov, *Inorg. Mater.* **8**, 1686 (1972).

[59] W. Jeitschko, *Acta Crystallogr. B* **33**, 2347 (1977).

[60] P. -O. Snell, *Acta Chem. Scand.* **21**, 1773 (1967).

[61] O. Yu. Pankratova, V. A. Novakovskii, V. A. Vladimirova and R. A. Zvinchuk, *Russ. J. Inorg. Chem.* **31**, 926 (1986).

[62] J. R. Dahn, W. R. McKinnon, R. R. Haering, W. J. L. Buyers and B. M. Powell, *Can. J. Phys.*

58, 207 (1980).

[63] L. I. Johansson, P. M. Stefan, M. L. Shek and A. N. Christensen, *Phys. Rev. B* **22**, 1032 (1980).

[64] Y. Tezuka, S. Shin, T. Ishii, T. Ejima, S. Suzuki and S. Sato, *J. Phys. Soc. Jpn.* **63**, 347 (1994).

[65] W. Speier, E. V. Leuken, J. C. Fuggle, D. D. Sarma, L. Kumar, B. Dauth and K. H. J. Buschow, *Phys. Rev. B* **39**, 6008 (1989).

[66] G. K. Wertheim, F. J. DiSalvo and D. N. E. Buchanan, *Solid State Commun.* **13**, 1225 (1973).

[67] P. Mohn and D. G. Pettifor, *J. Phys. C* **21**, 2829 (1988).

[68] A. Pasturel, C. Colinet and P. Hicter, *Physica B* **132**, 177 (1985).

[69] L. M. Mattheiss, *Phys. Rev. B* **5**, 290 (1972).

[70] J. H. Binks and J. A. Duffy, *J. Solid State Chem.* **87**, 195 (1990)

[71] J. Klima, G. Schadler, P. Weinberger and A. Neckel, *J. Phys. F: Met. Phys.* **15**, 1307 (1985).

[72] G. Hörmandinger, J. Redinger and P. Weinberger, *Solid State Commun.* **68**, 467 (1988).

[73] F. Schlapansky, P. Herzig, R. Eibler, G. Hobiger and A. Neckel, *Z. Phys. B, Condens. Matter* **75**, 187 (1989).

[74] P. K. Khowash and D. E. Ellis, *J. Appl. Phys.* **65**, 4815 (1989).

[75] P. K. Khowash and D. E. Ellis, *Phys. Rev. B* **39**, 1908 (1989).

[76] G. Hobiger, P. Herzig, R. Eibler, F. Schlapansky and A. Neckel, *J. Phys., Condens. Matter* **2**, 4595 (1990).

[77] S. R. Barman and D. D. Sarma, *Phys. Rev. B* **49**, 16141 (1993).

[78] K. Vos, *J. Phys. C* **10**, 3917 (1977).

[79] N. Daude, C. Gout and L. Jouanin, *Phys. Rev. B* **15**, 3229 (1977).

[80] N. I. Medvedeva, V. P. Zhukov, M. Y. Khodos and V. A. Gubanov, *Phys. Stat. Sol. B* **160**, 517 (1990).

[81] K. M. Glassford, N. Troullier, J. L. Martins and J. R. Chelikowsky, *Solid State Commun.* **76**, 635 (1990).

[82] J. W. Halley, M. T. Michalewicz and N. Tit, *Phys. Rev. B* **41**, 10165 (1990).

[83] V. A. Gubanov and N. I. Medvedeva, *Physica B* **172**, 285 (1991).

[84] B. Silvi, N. Fourati, R. Nada and C. R. A. Catlow, *J. Phys. Chem. Solids* **52**, 1005 (1991).

[85] M. A. Khan, A. Kotani and J. C. Parlebas, *J. Phys., Condens. Matter.* **3**, 1763 (1991).

[86] B. Poumellec, P. J. Durham and G. Y. Guo, *J. Phys., Condens. Matter.* **3**, 8195 (1991).

[87] K. M. Glassford, J. R. Chelikowsky, *Phys. Rev. B* **46**, 1284 (1992).

[88] K. C. Mishra, K. H. Johnson and P. C. Schmidt, *J. Phys. Chem. Solids* **54**, 237 (1993).

[89] L. B. Lin, S. D. Mo and D. L. Lin, *J. Phys. Chem. Solids* **54**, 907 (1993).

[90] S. D. Mo, L. B. Lin and D. L. Lin, *J. Phys. Chem. Solids* **55**, 1309 (1994).

[91] J. K. Burdett, *Acta Cryst. B* **51**, 547 (1995).

[92] P. Reinhardt, B. A. Heβ and M. Causá, *Int. J. Quantum Chem.* **58**, 297 (1996).

[93] J. H. Weaver, A. Franciosi and V. L. Moruzzi, *Phys. Rev. B* **29**, 3293 (1984).

[94] L. F. Mattheiss and J. C. Hensel, *Phys. Rev. B* **39**, 7754 (1988).

[95] N. Takao, I. Tanaka and H. Adachi, *Intermetalics* **4**, S113 (1996).

[96] J. Nakahara, H. Franzen and D. K. Misemer, *J. Chem. Phys.* **76**, 4080 (1982).

Chapter 4
Chemical bonding of transition metal carbides

4.1 Introduction

TiC and VC in the rock-salt type structure possess very high melting points and extreme hardness. The rock-salt type structure is one of the most simple structure and very applicable to theoretical calculations. As mentioned in Chapter 3, a considerable number of theoretical calculations for TiC and VC have been performed by band-structure calculation, cluster method or tight binding calculation. In steel industry, transition metal carbides play very important role to control or to improve various properties of steel. In contrast to many previous theoretical works for TiC and VC, there are a few theoretical calculations for the electronic structure of chromium, manganese and iron carbides, since these carbides exhibit much more complicated structures than the rock-salt type structure. Especially, the unit cells of Cr_7C_3 and $Cr_{23}C_6$ contain 40 and 116 atoms, respectively and there is no band-structure calculation for these carbides. Regarding chromium carbides, only one calculation have been performed by semiempirical cluster method [1] and it was found that in the low Cr carbide, the Cr-Cr bond is predominant and in the highest Cr carbide the Cr-C bond populations exceed those of the Cr-Cr bond. The electronic structure of Fe_3C have been calculated by band-structure calculations [2, 3] tight binding calculation [4] and extended Hückel molecular orbital method [5]. However, the chemical bonding in Fe_3C was not discussed quantitatively.

It is not so difficult to perform a systematic theoretical calculation for the compounds with the same crystal structures. However, when going form left to right in the 3d transition metal carbides, their crystal structures dramatically change. As mentioned in Chapter 1, the chemical bonding in compounds is so affected by their crystal structures and stoichiometries, that it is difficult to estimate the chemical bonding among compounds with various crystal structures and stoichiometries. There is no previous work to discuss the chemical bonding throughout the series of the 3d transition metal carbides.

In this Chapter, the electronic structures of 3d transition metal carbides, TiC, V_2C, VC, $Cr_{23}C_6$, Cr_7C_3, Cr_3C_2, Mn_3C, Fe_3C, Co_3C and Ni_3C were calculated by first principles molecular orbital calculations using the DV-Xα cluster method. The origin of the covalent bondings were investigated and the chemical bonding and total covalent bonding were quantitatively discussed by the use of

the bond overlap population and the covalent bond density.

4.2 Crystal Structures

TiC and VC have the rock-salt type cubic structure which belongs to the spacegroup , with a=4.3275Å [6] and 4.167Å [7], respectively. There are four metal atoms and C atoms in the unit cell. Every metal and C atoms are located in a octahedron composed of six another kind of atoms at a distance of half of a-axis length. The metal-metal and C-C distances are the same, 3.060 and 2.947Å in TiC and VC, respectively.

The crystal structure of V_2C is Mo_2C type orthorhombic structure which belongs to the spacegroup *Pbcm*, with a= 4.5770Å, b= 5.7420Å and c= 5.0370Å [8]. The V atoms are arranged in slightly distorted hexagonal layers (Fig. 4-1 (c)). The V layers are stacked in the sequence of ABAB... along the a-axis and the arrangement of V atoms is nearly hexagonal close-packed (HCP) except

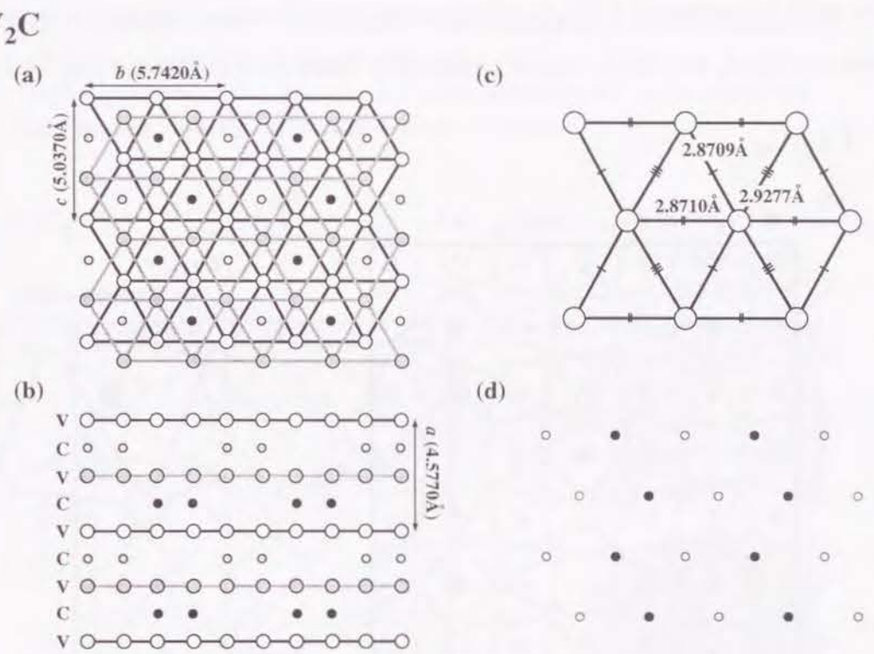

Fig. 4-1 The structure of V_2C.
(a) The (001) projection.
(b) The stacking of the V and C layers.
(c) The arrangement of V atoms in the layer.
(d) The arrangement of C atoms in the layer: C atoms occupy octahedral sites represented with solid circles. Open circles denote unoccupied sites.

their small distortion. The C atoms occupy half of octahedral sites ordered in a layer as seen in Fig. 4-1 (d). Every V atom has three C atoms at a average distance of 2.023Å.

The crystal structure of $Cr_{23}C_6$ is cubic structure which belongs to the spacegroup $Fm\bar{3}m$, with a=10.6595Å [9]. There are four Cr_1 atoms on 4*a* site, eight Cr_2 atoms on 8*c* site, 32 Cr_3 atoms on 32*f* site, 48 Cr_4 atoms on 48*h* site and 24 C atoms on 24*e* site in Wyckoff notation in the unit cell. Every C atom is surrounded by eight Cr atoms at an average distance of 2.124Å forming a square antiprism (Fig. 4-2 (b)). These square antiprisms are joined by sharing their corners and edges with right angles. The Cr_1 and Cr_2 atoms has no nearest neighbor C atoms. The Cr_1 atoms are located at FCC sites and surrounded only 12 Cr atoms at a distance of 2.561Å. Every Cr_2 atom has 4 first and 12 second nearest neighbor Cr atoms at a distance of 2.437Å and 2.927Å, respectively. Every Cr_3 atom has 10 nearest neighbor Cr atoms at an average distance of 2.586Å and three C atom at a distance of 2.113Å. Every Cr_4 atom has 12 nearest neighbor Cr atoms at an average distance of 2.638Å and two C atoms at a distance of 2.130Å.

The crystal structure of Cr_7C_3 is orthorhombic structure which belongs to the spacegroup *Pnma* with a=4.526Å, b=7.010Å and c=12.142Å [10]. There are five different sites for Cr and two

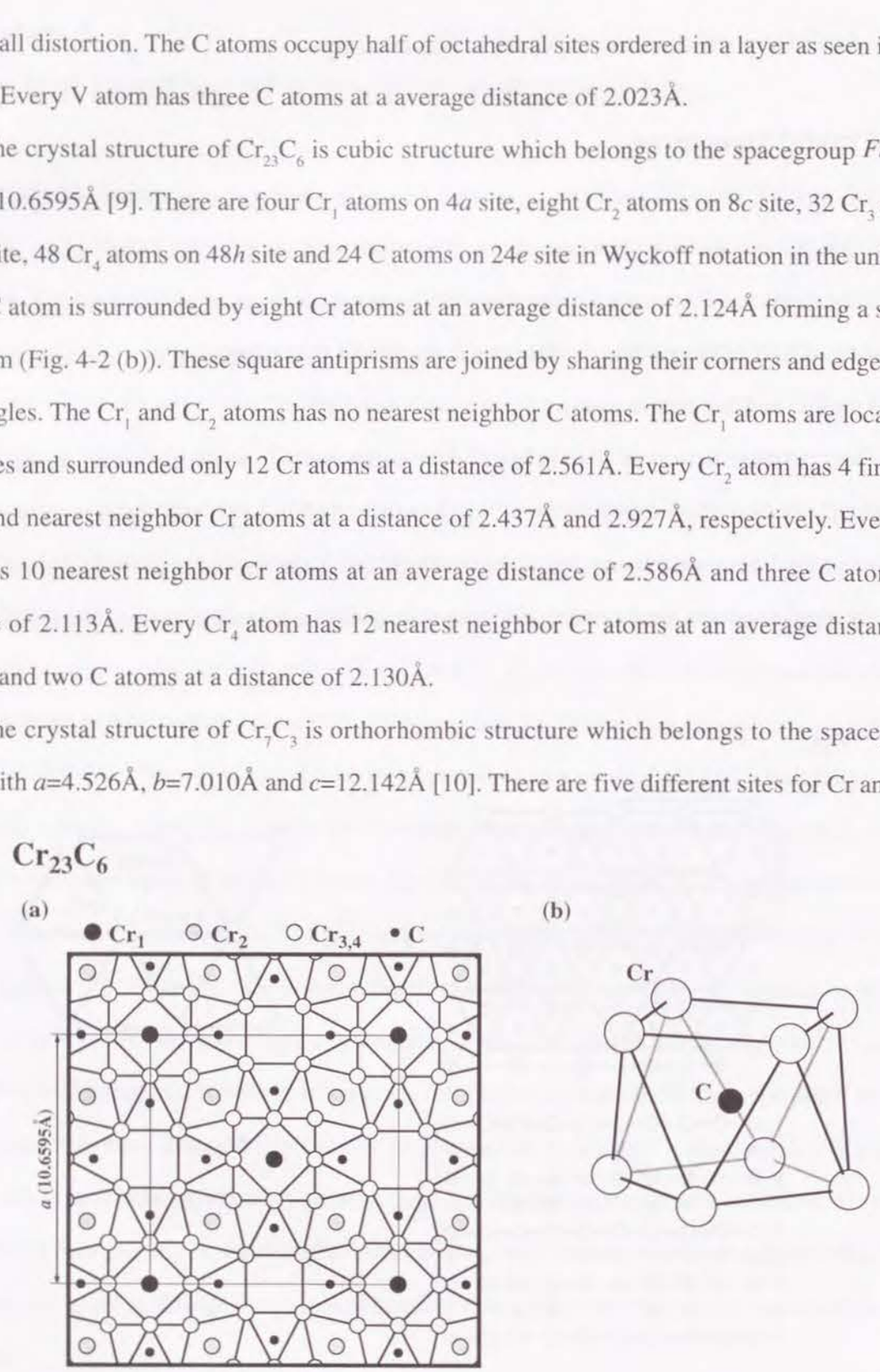

Fig. 4-2 The structure of $Cr_{23}C_6$.
(a) The {100} projection.
(b) Local structure around C atom: a square antiprism composed of eight Cr atoms and one C atom.

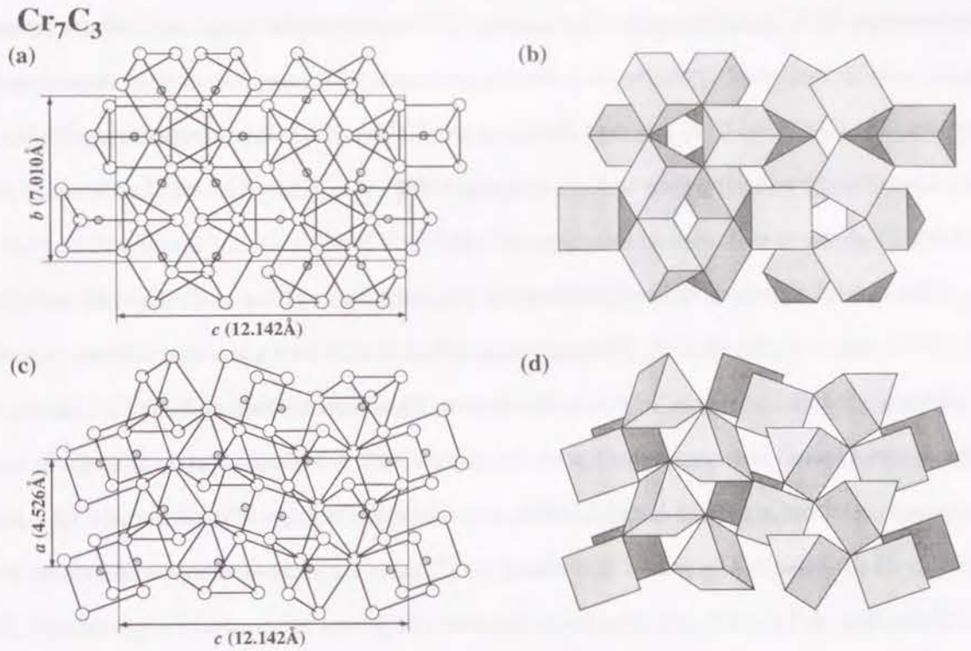

Fig. 4-3 The structure of Cr_7C_3.
(a) The (100) projection. Large and small circles denote Cr and C atoms, respectively.
(b) The same view as (a) drawn with only trigonal prisms.
(c) The (010) projection. Large and small circles denote Cr and C atoms, respectively.
(d) The same view as (c) drawn with only trigonal prisms.

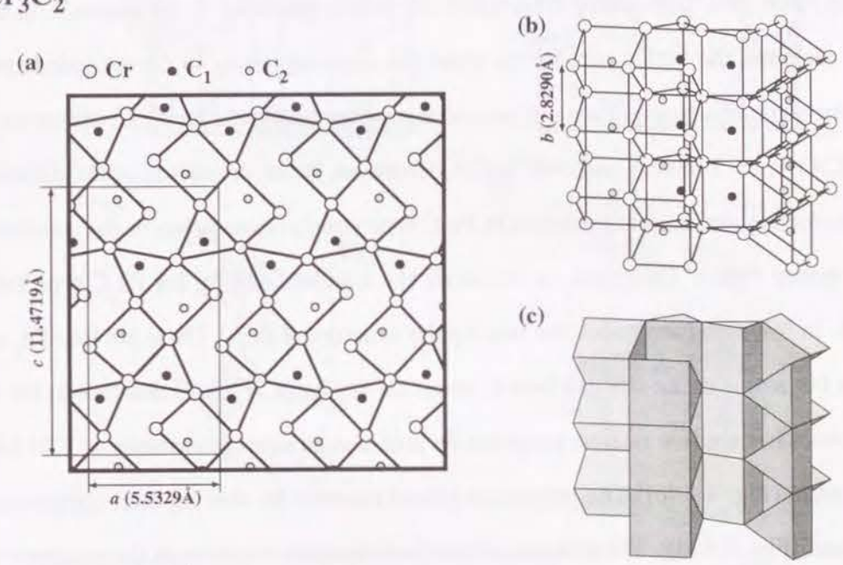

Fig. 4-4 The structure of Cr_3C_2.
(a) The (010) projection.
(b) The stacking of trigonal prisms in the dirction of [010].
(c) The same view as (b) drawn with only trigonal prisms.

different sites for C in the unit cell. The number of Cr and C atoms in the unit cell are 28 and 12, respectively. Both C_1 and C_2 atoms are located in a trigonal prism composed of six nearest neighbor Cr atoms. The Cr-C_1 and Cr-C_2 average distances are 2.048Å and 2.054Å, respectively. The trigonal prisms are joined by sharing their corners and edges (Fig. 4-3). Every Cr atom has 11 or 12 nearest neighbor Cr atoms at distances in the range of 2.493 to 2.755Å.

The crystal structure of Cr_3C_2 belongs to the same spacegroup as Cr_7C_3 with a=5.5329Å, b=2.8290Å and c=11.4719Å [11]. There are three different sites for Cr and two different sites for C. All atoms are located on 4*c* site in Wyckoff notation. Therefore, the unit cell has 12 Cr and eight C atoms. Every C atom are surrounded by six Fe atoms forming a trigonal prism. The Cr-C_1 and Cr-C_2 average distances are 2.085Å and 2.050Å, respectively. The crystal structure of Cr_3C_2 consists of joining of the prisms. The prisms containing the C_1 atom are stacked along the b-axis by sharing their plains (Fig. 4-4 (b),(c)). All other joints between the prisms are corner or edge sharing. The Cr atoms on Cr_1, Cr_2 and Cr_3 site have 11, 10 and 9 Cr atoms at an average distance of 2.687, 2.702 and 2.640Å, respectively.

Mn_3C, Fe_3C and Co_3C have Fe_3C type orthorhombic structure which belongs to the spacegroup *Pnma*, with a=5.080Å, b=6.772Å and c=4.530Å in Mn_3C [12], with a=5.0896Å, b=6.7443Å and c=4.5248Å in Fe_3C [13] and a=5.033Å, b=6.731Å and c=4.483Å in Co_3C [14], respectively. Regarding Mn_3C and Co_3C, there is no report for atomic positions in the unit cell. In many works for these carbides, the lattice parameters were given in *cab* setting in the extended symbol *Pmcn* which is the same spacegroup *Pnma*. If the *cab* setting are employed for Fe_3C, the lattice parameters are a=4.5248Å, b= 5.0896Å and c=6.7443Å. However, in the crystallographic database [15] the lattice parameters and atomic positions in Fe_3C type structure are given in the standard setting of the spacegroup *Pnma*. Therefore, in this work the standard setting for Fe_3C type structure was employed. In following sentences, we take up the structure of Fe_3C. There are four Fe_1 atoms on 4*c* site, eight Fe_2 atoms on 8*d* site and four C atoms on 4*c* site in Wyckoff notation in the unit cell.

Every C atom has six first nearest neighbor Fe atoms at an average distance of 2.018Å forming a trigonal prism (Fig. 4-5 (c)).The prisms are joined together by sharing their corners and edges to make a layer (Fig. 4-5 (d)). These layers are stacked along the b-axis with the sequence of ABAB... The Fe_1 has 12 nearest neighbor Fe atoms at an average distance of 2.630Å and two nearest neighbor C atoms at an average distance of 1.978Å. The Fe_2 has 11 nearest neighbor Fe atoms at an average

distance of 2.591Å and two nearest neighbor C atoms at an average distance of 2.038Å. These Fe-Fe distances in Fe_3C are close to the Fe-Fe distance of 2.579Å in FCC-Fe (γ-Fe).

The crystal structure of Ni_3C is trigonal structure which belongs to the spacegroup $R\bar{3}c$, with a=4.553Å and c=12.92Å [16] (Fig. 4-6). The arrangement of Ni atoms is HCP and C atoms occupy one third of octahedral sites ordered to keep their adjacent sites empty. Consequently, C atoms are arranged in hexagonal layers. The Ni-C distance is 1.861Å. Every Ni atom has 12 nearest neighbor Ni atoms at an average distance of 2.632Å and two nearest neighbor C atoms.

In the 3d transition metal carbides, there is virtually no C-C direct bonding because the C-C distances are about 100% greater that the C-C covalent bond length of 1.54Å. In all carbides studied in this work without $Cr_{23}C_6$, every C atom has six nearest neighbor metal atoms. These neighboring metal atoms form a octahedron in TiC, VC, V_2C and Ni_3C or a trigonal prism in Cr_7C_3, Cr_3C_2, Mn_3C, Fe_3C and Co_3C. However, in the case of trigonal prisms, every C atom has not only the first nearest neighbor but also the second or third nearest neighbor atoms which are not farther enough

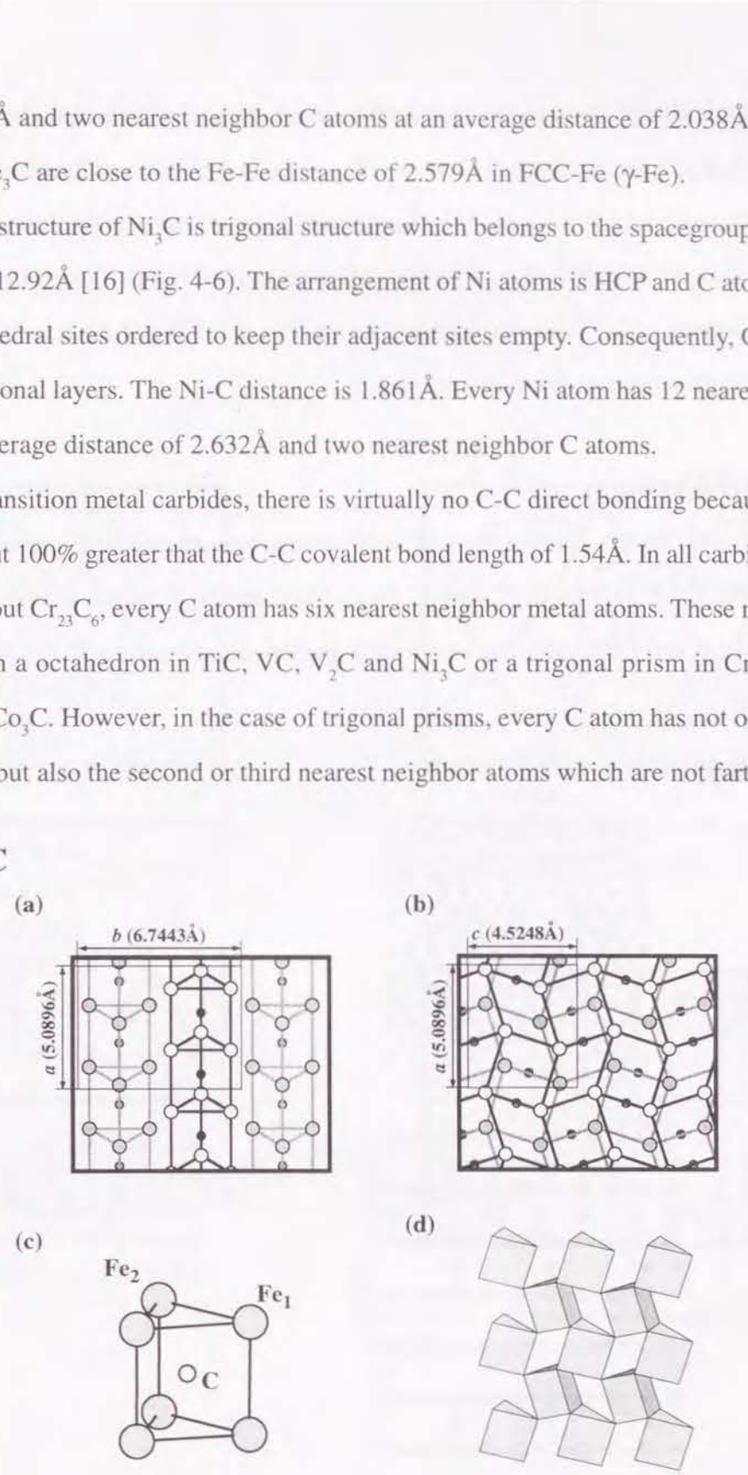

Fig. 4-5 The structure of Fe_3C (cementite).
(a) The (001) projection. (b) The (010) projection.
(c) Local structure around carbon atom: a trigonal prism composed of six Fe atoms and one carbon atom.
(d) The arrangement of the trigonal prisms in the layer.

to neglect their contribution to the chemical bonding. In Cr_7C_3, both C_1 and C_2 atoms have two second and a third nearest neighbor Cr atoms (Fig. 4-7). In Cr_3C_2, every C_1 atom has two farther Cr atoms at a distance of 2.290Å and 2.618Å and every C_2 atom has one second nearest neighbor Cr atoms at a distance of 2.260Å (Fig. 4-8). Every C atom in Fe_3C has two second nearest neighbor Fe atoms at a distance of 2.372Å in the adjacent layers (Fig. 4-9). Therefore, it is impossible to decide exact coordination number for these carbides.

4.3 Model Clusters

The model clusters composed of 64 to143 atoms were employed in present calculations for TiC, V_2C, VC, $Cr_{23}C_6$, Cr_7C_3,Cr_3C_2, Mn_3C, Fe_3C, Co_3C and Ni_3C shown in Fig. 3-7 and 3-8. With respect to Mn_3C and Co_3C which have the same crystal structure as Fe_3C, the atomic positions in

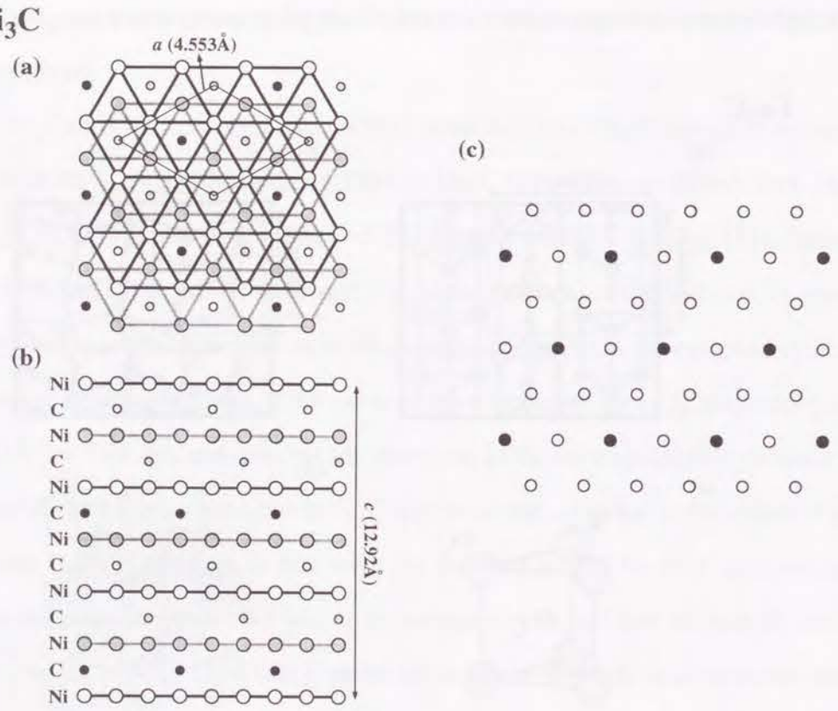

Fig. 4-6 The structure of Ni_3C.
(a) The (001) projection.
(b) The stacking of the Ni and C layers.
(c) The arrangement of C atoms in the layer: C atoms occupy octahedral sites represented with solid circles. Open circles denote unoccupied sites.

the unit cell were not reported. In this work, the coordinates of atoms in Mn_3C and Co_3C were generated with the use of the atomic positions of Fe_3C. The atomic orbitals used in the present calculations are 1s-4p for 3d transition metals and 1s-2p for C atom.

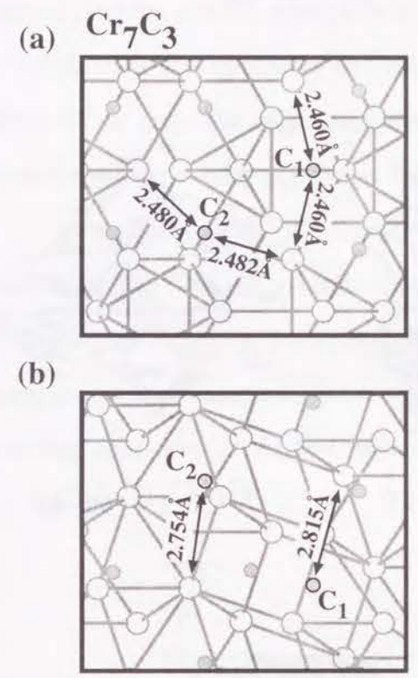

Fig. 4-7 The 2nd and 3rd nearest neighbor Cr atoms on C_1 and C_2 sites in Cr_7C_3.
(a) The 2nd nearest neighbor Cr atoms.
(b) The 3rd nearest neighbor Cr atoms.

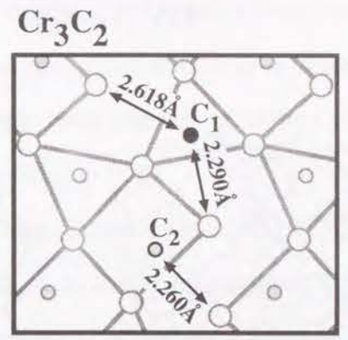

Fig. 4-8 The 2nd and 3rd nearest neighbor Cr atoms on C_1 and C_2 sites in Cr_3C_2.

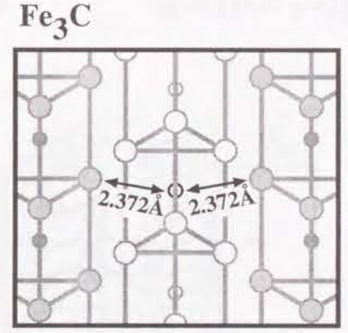

Fig. 4-9 The 2nd nearest neighbor Fe atoms on C site in Fe_3C.

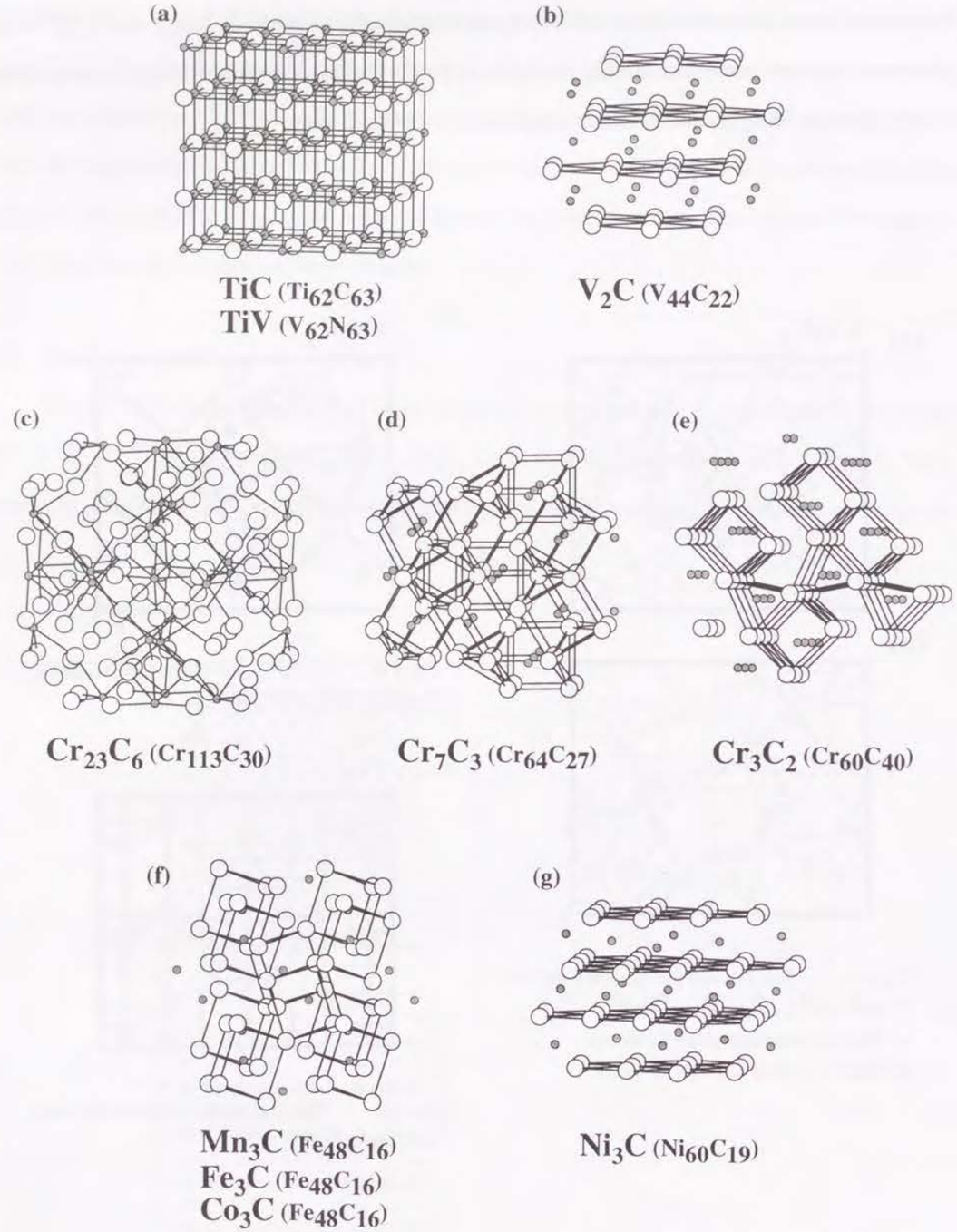

Fig. 4-10 The structure of model clusters employed in this work.
Large circles denote metal atoms and small circles denote C atoms.
(a) $Ti_{62}C_{63}$ cluster for TiC and $V_{62}C_{63}$ cluster for VC.
(b) $V_{44}C_{22}$ cluster for V_2C. (c) $Cr_{113}C_{30}$ cluster for $Cr_{23}C_6$.
(d) $Cr_{64}C_{27}$ cluster for Cr_7C_3.(e) $Cr_{60}C_{40}$ cluster for Cr_3C_2.
(f) $M_{48}C_{16}$ cluster for M_3C (M=Mn, Fe or Co).
(g) $Ni_{60}C_{19}$ cluster for Ni_3C.

4.4 Results

4.4.1. Density of states and overlap population diagram

The total and partial density of states (TDOS and PDOS) and the overlap population diagrams for the metal-C (M-C) and metal-metal (M-M) bonds of these model clusters are shown in Figs. 4-11 to 4-20. The DOS curves are made by broadening the discrete energy levels by Gaussian function of 1.0 eV full width at half-maximum (FWHM). The overlap population diagrams are obtained by convoluting the overlap population at each molecular orbital with Gaussian function of 1.0 eV FWHM. These curves of DOS and overlap population diagrams are shifted so as to set the Fermi level (E_F) at zero. The value written in each panel is the bond overlap population obtained by summing up the overlap population at each molecular orbital up to E_F.

In comparison with TiC and VC with the rock-salt type structure, the shapes of DOS resemble each other. The C-2s and 2p bands interacting with the M-3d, 4s and 4p orbitals have large bonding contribution for the M-C bonding. E_F in TiC lies between the Ti-3d and C-2p bands and the Ti-3d band is almost unoccupied. On the other hand, the V-3d band is partially occupied. However, the bonding character for the M-C bonding around E_F is nearly non-bonding, the increase of the

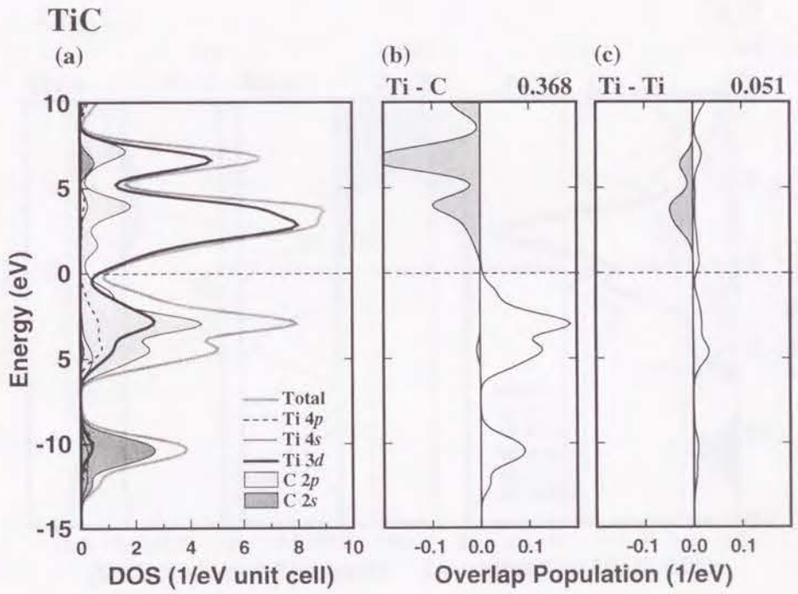

Fig. 4-11 Total and partial density of states and the overlap population diagrams for TiC.
(a) Total and partial density of states.
(b) Overlap population diagram for the Ti-C bond (c) for the Ti-Ti bond.

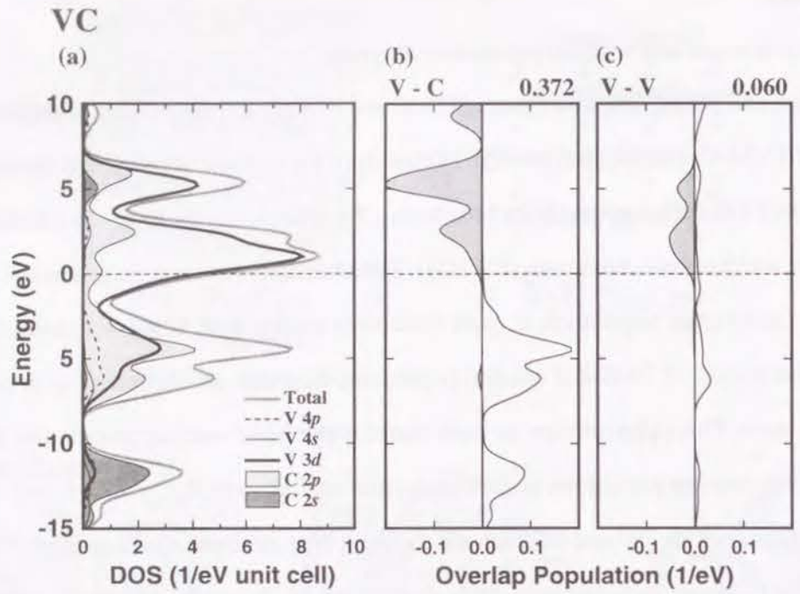

Fig. 4-12 Total and partial density of states and the overlap population diagrams for VC.
(a) Total and partial density of states.
(b) Overlap population diagram for the V-C bond (c) for the V-V bond.

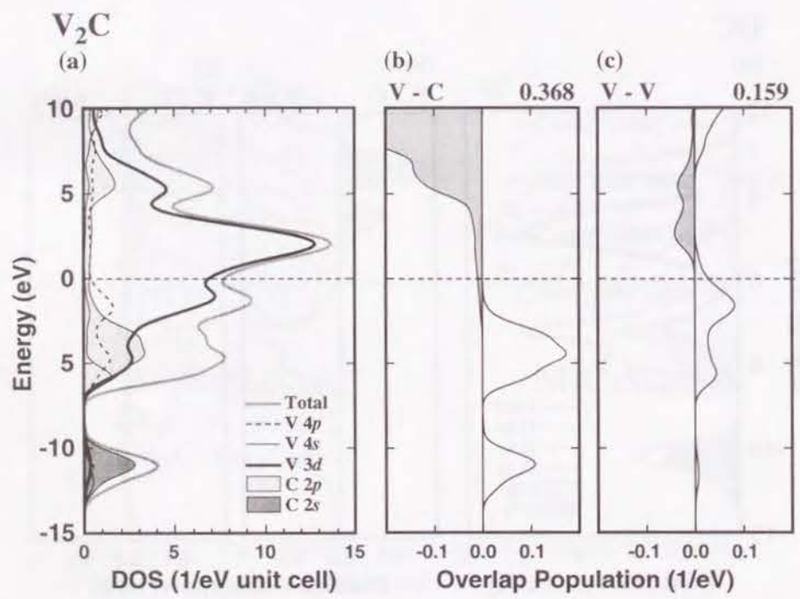

Fig. 4-13 Total and partial density of states and the overlap population diagrams for V_2C.
(a) Total and partial density of states.
(b) Overlap population diagram for the V-C bond (c) for the V-V bond.

occupation of the M-3d band does not have significant influence on the M-C bonding. The M-M bonds in TiC and VC show weak bonding character because of small bonding contribution of the C-2p band. In V_2C, there is no deep minimum of DOS between the C-2p and V-3d band which is seen in VC. The strong V-C bond is formed in the same way as VC and the strength of the V-C bond is almost equal to that in VC. Regarding the V-V bonding, the V-V bond mainly arise from the V-3d band located from -6 to 1 eV and the antibonding component located above E_F has no contribution to the V-V bonding. Although the average V-V distance of 2.861Å in V_2C is only 3% shorter than that of 2.947Å in VC, the strength of the V-V bond in V_2C is about three times larger than that in VC.

In $Cr_{23}C_6$, Cr_7C_3 and Cr_3C_2, there are several different Cr or C sites in their crystal structure. On DOS and PDOS, all different sites are taken into account. The overlap population diagrams of the Cr-C bonding are presented for C_1 site in Cr_7C_3 and. Cr_3C_2 Those of the Cr-Cr bonding are presented for Cr_1 sites in Cr_3C_2 and Cr_7C_3 and for Cr_3 site for $Cr_{23}C_6$. In these chromium carbides, the positions of the C-2s and 2p bands are similar to each other. The C-2s and 2p bands interact with the Cr-3d, 4s and 4p orbitals and have large bonding contribution to the Cr-C bonding. Regarding

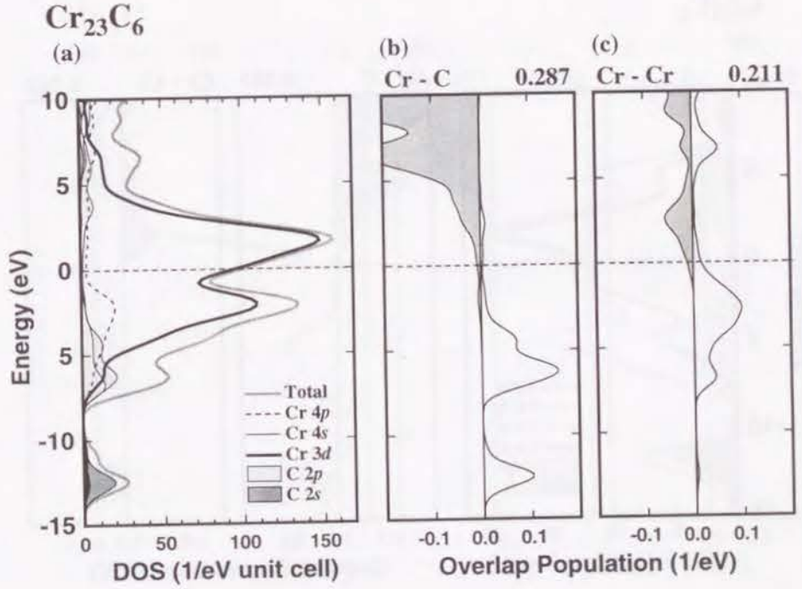

Fig. 4-14 Total and partial density of states and the overlap population diagrams for $Cr_{23}C_6$.
(a) Total and partial density of states.
(b) Overlap population diagram for the Cr-C bond (c) for the Cr-Cr bond.

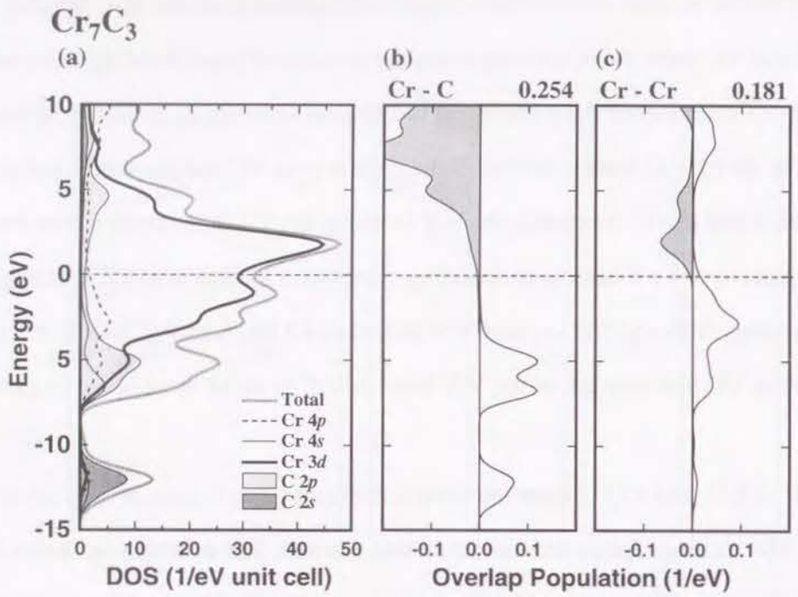

Fig. 4-15 Total and partial density of states and the overlap population diagrams for Cr_7C_3.
(a) Total and partial density of states.
(b) Overlap population diagram for the Cr-C bond (c) for the Cr-Cr bond.

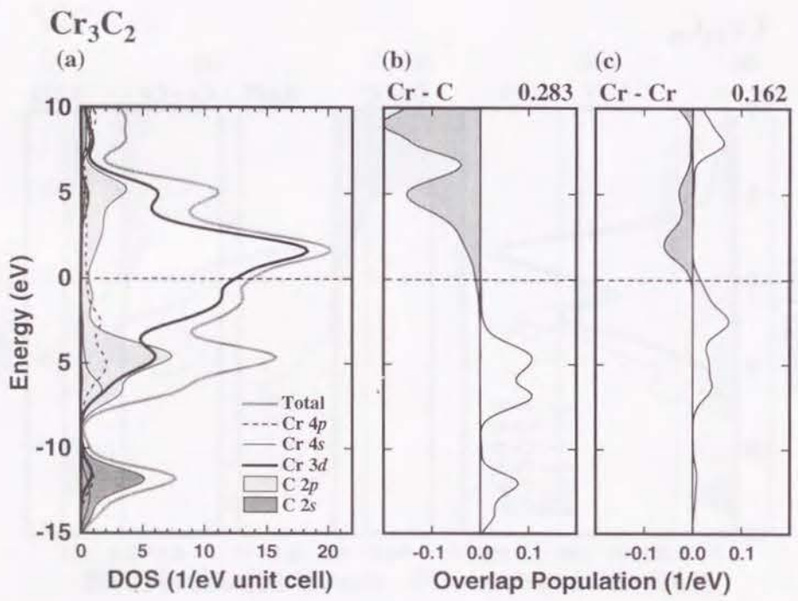

Fig. 4-16 Total and partial density of states and the overlap population diagrams for Cr_3C_2.
(a) Total and partial density of states.
(b) Overlap population diagram for the Cr-C bond (c) for the Cr-Cr bond.

the Cr-Cr bonding, E_F in these three carbides lies between the bonding and antibonding band. When going from $Cr_{23}C_6$ to Cr_3C_2, in other words with increase of the C content, the magnitude of the C-2s and 2p band increases, but the width of the C-2s and 2p bands do not change. The width of the Cr-3d band slightly decreases in the series from $Cr_{23}C_6$ to Cr_3C_2.

In Mn_3C, Fe_3C and Co_3C with Fe_3C type structure, there are two different sites for metal atoms. The overlap population diagrams in these carbides are shown about 8*d* site for the M-M bond. The DOS curves in these carbides resemble each other. However, with increasing atomic number of the M atoms, the M-3d band is shifted downwards and becomes narrower. On the contrary, the position of the C-2s and 2p bands are constant. The M-C bond mainly arises from the C-2s and 2p band interacting with the M-3d, 4s and 4p orbitals and the bonding character around E_F is nearly non-bonding. Therefore, the strength of the M-C bond does not depend on the M atoms. Regarding the M-M bonding, with increasing atomic number of the M atoms, the bonding and antibonding band move downwards and more electrons occupy the antibonding orbitals. As a result, the strength of the M-M bond decreases. Although the crystal structure of Ni_3C is different from the Fe_3C type structure, similar tendency can be seen for the change of the M-3d band in the series of Mn_3C to

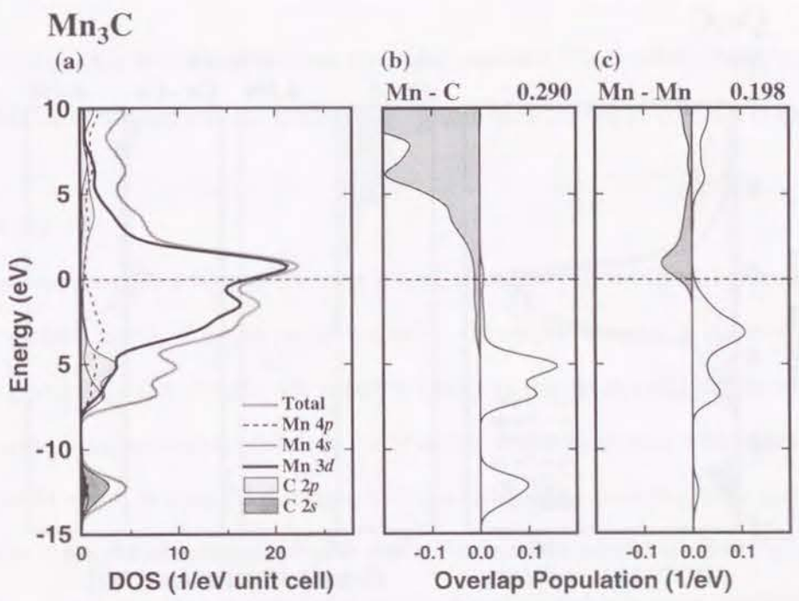

Fig. 4-17 Total and partial density of states and the overlap population diagrams for Mn_3C.
(a) Total and partial density of states.
(b) Overlap population diagram for the Mn-C bond (c) for the Mn-Mn bond.

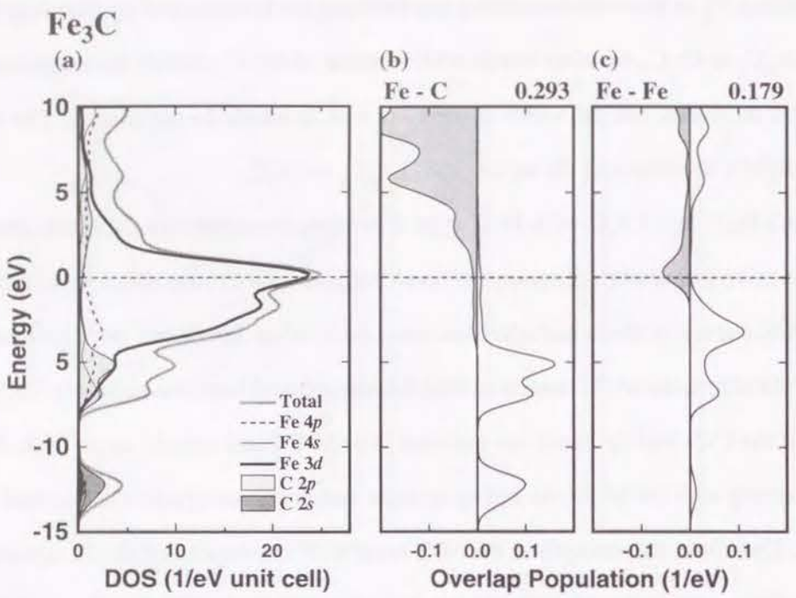

Fig. 4-18 Total and partial density of states and the overlap population diagrams for Fe_3C.
(a) Total and partial density of states.
(b) Overlap population diagram for the Fe-C bond (c) for the Fe-Fe bond.

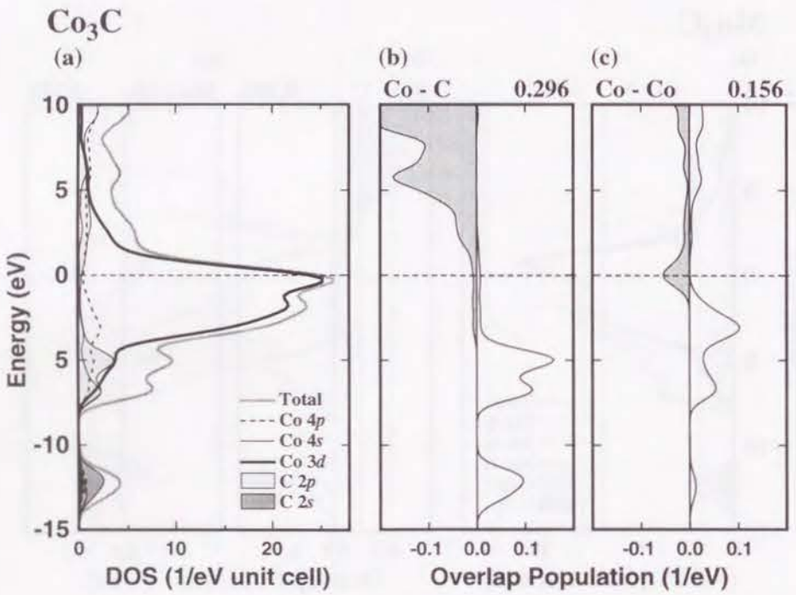

Fig. 4-19 Total and partial density of states and the overlap population diagrams for Co_3C.
(a) Total and partial density of states.
(b) Overlap population diagram for the Co-C bond (c) for the Co-Co bond.

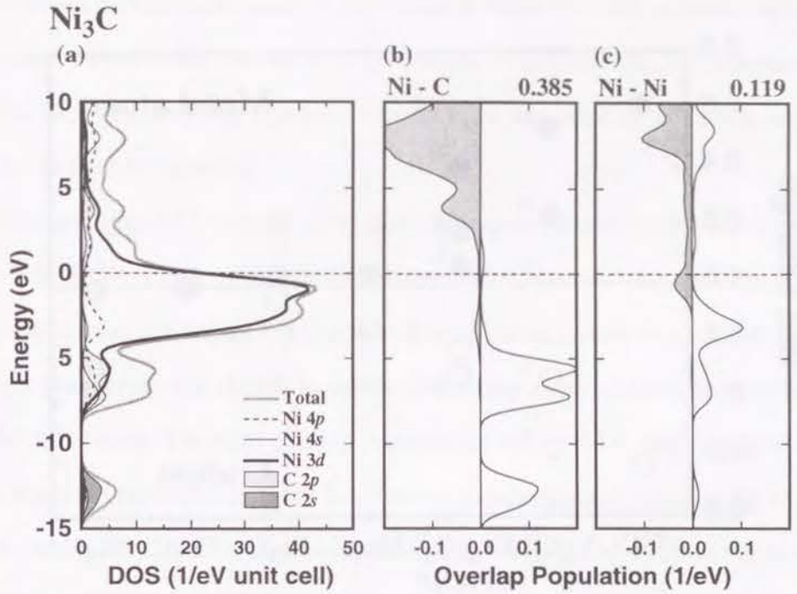

Fig. 4-20 Total and partial density of states and the overlap population diagrams for Ni_3C.
(a) Total and partial density of states.
(b) Overlap population diagram for the Ni-C bond (c) for the Ni-Ni bond.

Ni_3C. The Ni-3d band is lowest and narrowest in these carbides. The bonding character of the M-C bonding is still non-bonding, but the antibonding contribution for the M-M bond is the largest.

4.4.2 Net Charge

The net charges of the M and C atoms around the center of the model clusters for all the carbides are plotted in Fig. 4-21. In earlier carbides, the charge transfer occur from the M to C atom. When going from left to right, the absolute values of the net charges decreases. This result indicates that the ionic interaction between the M and C atoms decreases with increasing atomic number of the M atom. In later 3d transiton metalcarbides, Co_3C and Ni_3C, the direction of the charge transfer changes. In comparison with earlier 3d transiton metal carbides, TiC and VC, the amount of the charge transfer in later 3d transiton metal carbides is quite small and the ionic interaction is not significant.

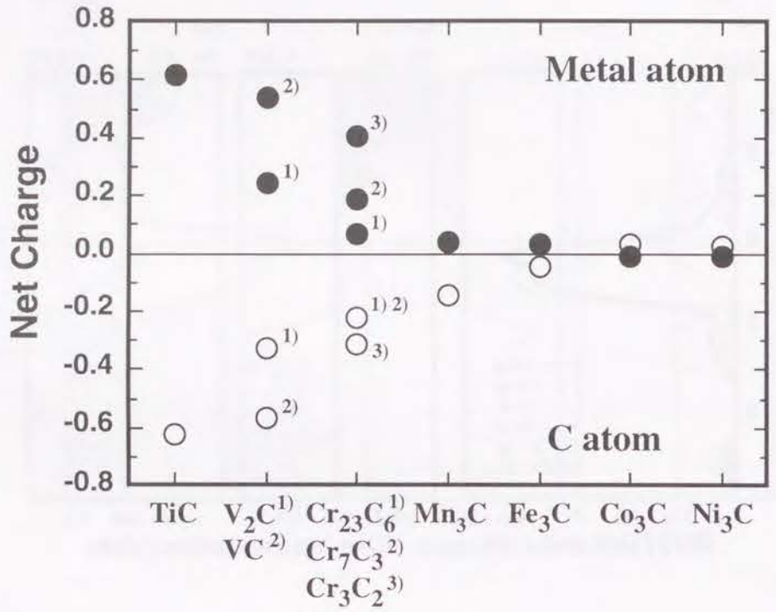

Fig. 4-21 Net charges for all model clusters studied in this work as a function of the atomic number of metal atoms. Filled and filled marks denote the net charge of metal and C atoms, respectively.

4.5 Discussion

4.5.1 M-C bond

With respect to the M-C bonding, similar features can be seen in all carbides studied in this work. The C-2s and 2p bands interact with the M-3d, 4s and 4p orbitals and have large bonding contribution. The antibonding component is located above E_F and the bonding character around E_F is nearly non-bonding. The number of the first nearest neighbor M atoms on the C site in 3d transition metal binary carbides is six except $Cr_{23}C_6$ structure. However, as mentioned above, the C atom located in a trigonal prism composed of six metal atoms has not only the first nearest neighbor metal atoms but also farther metal atoms which have contribution to the chemical bonding. In order to compare the chemical bonding for the C atoms located in different local structures, the total bond overlap populations are evaluated by summing up the bond overlap populations for the M-C bonds around the C atoms and plotted in Fig. 4-22. Irrespective of the atomic number of M atoms or the C content, the total bond overlap populations are almost constant. This result indicates that the covalent

bondings formed around the C atom in 3d transition metal carbides is almost independent of the sort of M atom or C content. One of the reason is that throughout the 3d transition metal carbides from TiC to Ni_3C, the bonding character around E_F is non-bonding and there is no antibonding contribution to the M-C bonding.

PDOSs in Figs. 4-11 to 4-20 show that the largest overlap in PDOS is the M-3d - C-2p overlap and the M-4s and 4p orbitals have less than as half overlap with the C-2p band as the M-3d orbitals. As discussed in Chapter 3, it is generally considered that an overlap of the PDOS indicates the covalent interaction, but the M-4p orbitals have larger spatial overlap with the C-2p orbitals than the M-3d orbitals. The total overlap populations for the M-C bonds around the C atom for valence orbitals are presented in Table 4-1. The overlap population between the M-3d and C-2p is the largest without Co_3C, but the overlap population between the M-4p and C-2p orbitals is as large as that between the M-3d and C-2p orbitals. Therefore, the M-C covalent bonding mainly arises from the interaction not only between the M-3d and C-2p but also between the M-4p and C 2p orbitals.

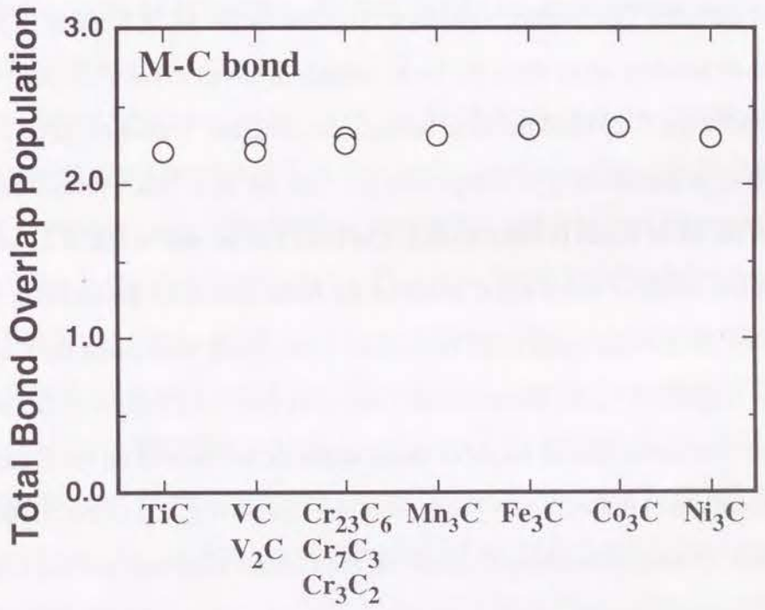

Fig. 4-22 Total bond overlap populations on C sites for the M-C bonding.

Table 4-1 Overlap populations of the M-C bond for valence orbitals.

	M– C 2s			M– C 2p		
	3d-2s	4s-2s	4p-2s	3d-2p	4s-2p	4p-2p
TiC	0.193	0.116	0.314	0.851	0.316	0.642
V_2C	0.280	0.078	0.283	0.955	0.320	0.584
VC	0.211	0.124	0.319	0.869	0.315	0.639
$Cr_{23}C_6$	0.239	0.081	0.342	0.832	0.372	0.687
Cr_7C_3	0.241	0.076	0.338	0.815	0.347	0.700
Cr_3C_2	0.209	0.097	0.324	0.791	0.355	0.698
Mn_3C	0.232	0.075	0.347	0.806	0.365	0.701
Fe_3C	0.208	0.083	0.361	0.736	0.388	0.729
Co_3C	0.195	0.097	0.374	0.685	0.419	0.725
Ni_3C	0.208	0.120	0.369	0.751	0.401	0.637

4.5.2 M-M bond

In TiC and VC which have the highest C content in carbides studied here, the M-M bond is weaker than other carbides. The overlap population diagrams for the M-M bonding in TiC and VC show the weak M-M bonding arises from the M-3d orbitals involved in the C-2p band and the M-3d band located above the C-2p band has little bonding contribution. Transition metal carbides are generally considered as interstitial type compounds in which the M-C bonds formed around the C atom do not break the M-M bonds in metal matrix. The trend can be seen in Fig. 4-23 which shows the number of nearest neighbor metal and C atoms on the metal sites in all the carbides. If there are different metal sites, the average value of all metal sites is presented. With rising the C content, the number of nearest neighbor C atoms monotonically increases and is the highest at TiC and VC. On the other hand, the number of nearest neighbor metal atoms do not depend on the C content. With respect to the chromium carbides, when going from the lowest ($Cr_{23}C_6$) to the highest (Cr_3C_2) carbide, the number of nearest neighbor C atoms on the Cr sites increases and the bond overlap population of the Cr-Cr bond written in Figs. 4-14 to 4-16 (c) decreases. These results suggest that the M-C bonding around the metal atoms reduces the strength of the M-M bond, because the M-3d, 4s and 4p orbitals involved in the C-2p band are employed in forming the M-C bonding and have

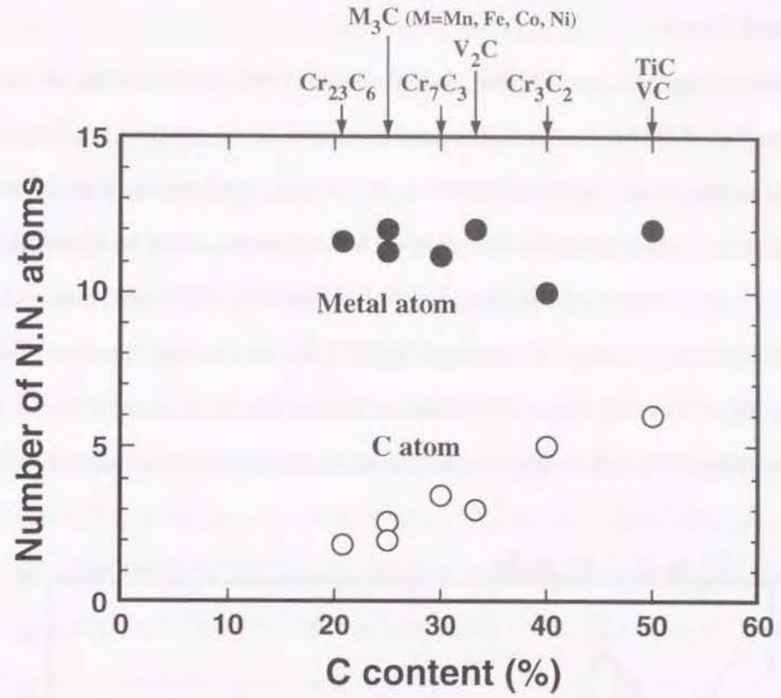

Fig. 4-23 Number of nearest neighbor atoms on metal sites as a function of the C content.

small contribution to the M-M bonding. We shall discuss this point more quantitatively later using the covalent bond density.

Another factor which has influence on the M-M bonding is the atomic number of metal atoms. With respect to the position of E_F in the overlap population diagrams for the M-M bonding, E_F is located in the upper side of the bonding band in V_2C and is located between the bonding and antibonding bands in the chromium carbides. Therefore, the antibonding band does not contribute to the M-M bonding in these carbides. On the other hand, later 3d transition metal carbides from Mn_3C to Ni_3C, with increasing atomic number of the metal atoms, E_F is shifted upwards and more electrons occupy the antibonding orbitals. Consequently, the strength of the M-M bond decreases because of the increase of the antibonding contribution. When going from left to right in the 3d transition metal carbides, the bonding contribution for the M-M bonding increases from Ti to Cr, and with beginning of the occupation of the antibonding band, the bonding contribution decreases from Mn to Ni. In contrast to the M-C bonding, the strength of the M-M bonding strongly depends on the sort of the M atom and the C content in carbides.

4.5.3 Covalent Bond Density

As described in Chapter 3, the covalent bond density is evaluated by taking account of the strength and the number of the bonds and represents the strength of the covalent bonding in the unit volume irrespective of the crystal structure. Therefore, the covalent bond density is useful to estimate the covalent bonding more quantitatively . The covalent bond densities of the M-C and M-M bonds and the C content are shown in Fig. 4-24. Thecovalent bond density of the M-C bonds changes in proportion to the C content, because the covalent bonding formed around the C atom is almost independent of the sort of M atoms and the C content as seen in Fig. 4-22. As seen in Fig. 4-23, the number of the nearest neighbor metal atoms on metal sites is distributed in the range of 10 to 12 and

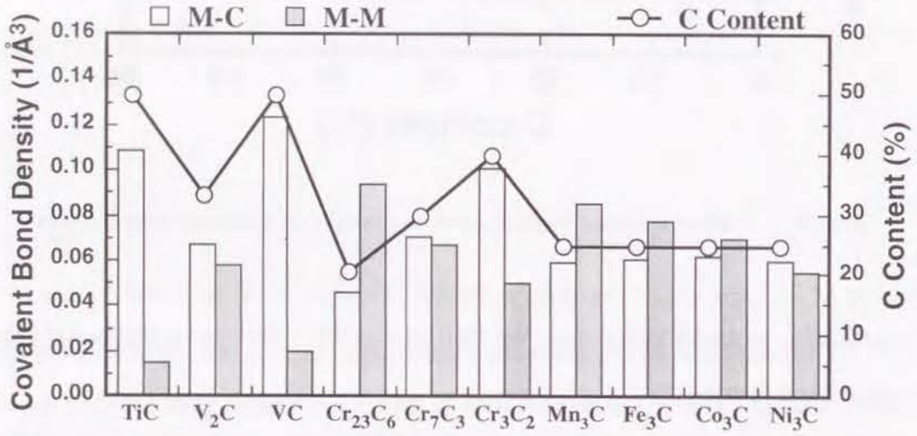

Fig. 4-24 Covalent bond densities for the M-C and M-M bonding and the C content.

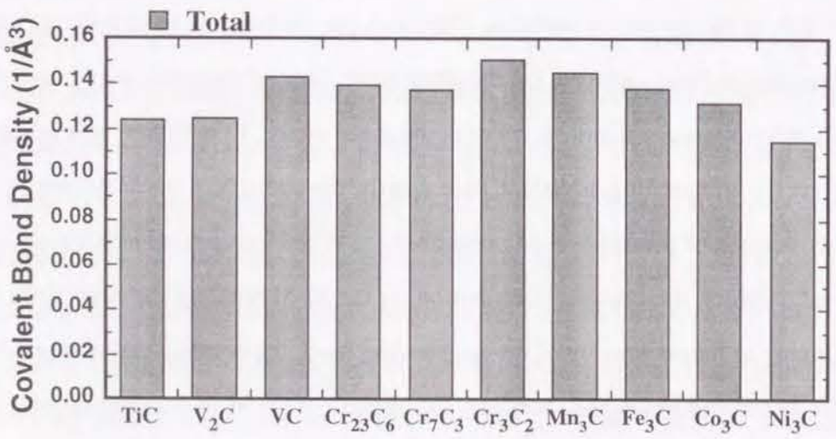

Fig. 4-25 Total covalent bond densities.

independent of the C content, which indicates that the increase of the C content in carbides does not directly reduce the number of the M-M bonds. However, as discussed above, the strength of the M-M bonding strongly depends on the sort of the metal atom and the C content in carbides. These features are clearly seen in Fig. 4-24. In the carbide which has higher C content, the covalent bond density of the M-M bond becomes smaller. Regarding the dependence of the sort of M atom, comparing from Mn_3C to Ni_3C with the same C content, the covalent bond density of the M-M bond decreases with increasing atomic number of the M atom. Comparing the M-C and M-M bonding, in low C carbides, the dominant chemical bonding is the M-M bonding. If the C content exceed about 30%, the dominant chemical bonding change to the M-C bonding.

Total covalent bond density which is sum of the covalent bond densities of the M-C and M-M bonds are shown in Fig. 4-25. The total covalent bond density is the highest around the chromium carbides. However, comparing with other compounds discussed in Chapter 3, all the carbides can be considered to possess strong covalent bonding. In 3d transition metal carbides, TiC and VC have quite higher melting points than other carbides. However, the total covalent bond density of TiC and VC is not large very much. The net charges in Fig. 4-21 show that TiC and VC have larger ionic interaction between the metal and C atoms than other carbides. Therefore, these results suggest that high melting point in TiC and VC arises from not only the covalent bonding but also the ionic bonding.

4.6 Conclusion

We have performed the first principles molecular orbital calculations using model clusters in order to study the chemical bonding of 3d transition metal carbides, TiC, V_2C, VC, $Cr_{23}C_6$, Cr_7C_3, Cr_3C_2, Mn_3C, Fe_3C, Co_3C and Ni_3C. Main results can be summarized as follows:

(1) In all the carbides, the strong metal-C (M-C) bond is formed by the interaction of the C-2s and 2p bands with the M-3d, 4s and 4p orbitals. The strength of the M-C bonding is almost independent of the sort of the M atoms and the C content in the carbides.

(2) The strength of the metal-metal (M-M) bonding decreases with the increase of the C content in the carbides. In later 3d transition metal carbides, from Mn to Ni, the M-M bonding decreases with increasing atomic number of the M atoms because of the increase of the antibonding contribution.

(3) In low C carbides, the dominant chemical bonding is the M-M bonding. If the C content exceed about 30%, the dominant chemical bonding change to the M-C bonding. The total covalent bond density increases from TiC to Cr_3C_2 and decreases going to right. However, the change is not so large and the 3d transition metal carbides can be considered to have large amount of the covalent bonding.

(4) From TiC to Fe_3C, the charge transfer occur from the M to C atom and the direction is opposite in Co_3C and Ni_3C. The amount of charge transfer decreases with increasing atomic number of the M atom. Especially, in later carbides from Mn_3C to Ni_3C, the amount of the charge transfer is quite small, which indicates that the ionic interaction is not significant in these carbides.

References

[1] A. L. Ivanovskii, D. L. Novikov, S. N. Shamin, V. A. Guvabov and E. Z. kurmaev, *Izv. Akad. Nauk SSSR, Ser. neorg. Mater.* **21**, 1149 (1985).

[2] E. J. Garba and R. L. Jacobs, *J. Phys. Chem. Solids* **50**, 101 (1989).

[3] J. Häglund and G. Grimvall, *Phys. Rev. B* **44**, 2914 (1991).

[4] A. H. Cottrell, *Mater. Sci. Technol.* **9**, 277 (1993).

[5] S. Yamamoto, Y. Kobayashi, N. Inoyama and A. Kirihata, *Proceedings of the 4th International Symposium on the Physical Metallurgy of Cast Iron*, edited by G. Ohira, T. Kusakawa and E. Niyama (Pittsburgh, Pennsylvania: Materials Research Sociery), p. 103 (1990).

[6] S. Shimada, J. Watanabe, K. Kodaira and T. Matsushita, *J. Materials Sci.* **24**, 2513 (1989).

[7] K. E. Spear and J. M. Leitnaker, *High Temp. Sci.* **1**, 401 (1969).

[8] K. Yvon, W. Rieger and H. Nowotny, *Mh. Chem.* **97**, 689 (1966).

[9] H. L. Yakel, *Acta Crystallogr. B* **43**, 230 (1987).

[10] M. A. Rouault, P. Herpin and M. R. Fruchart, *Ann. Chim., Sci. Mater.* **5**, 461 (1970).

[11] S. Rundqvist and G. Runnsjo, *Acta Chem. Scand.* **23**, 1191 (1969).

[12] K. Kuo and L. E. Persson, *J. Iron Steel Inst.* **178**, 39 (1954).

[13] E. J. Fasiska and G. A. Jeffrey, *Acta Cryst.* **19**, 463 (1965).

[14] S. Nagakura, *J. Phys. Soc. Jpn.* **16**, 1213 (1961).

[15] P. Villars and L. D. Calvert (ed.), *Pearson's Handbook of Crystallographic Data for Intermetallic Phases*, Materials Park, Oh 44073, American Society for Metals p. 1520 (1985).

[16] S. Nagakura, *J. Phys. Soc. Jpn.* **13**, 1005 (1958).

Chapter 5
Effect of solute atoms on the chemical bonding of Fe_3C (cementite)

5.1 Introduction

Fe_3C (cementite) is a metastable compound at all temperatures in the Fe-C binary system. It precipitates by cooling from *g* Fe-C solid solution or by annealing after quenching. Since it plays very important role in steel technology, a considerable number of experimental studies have been made on its structure, precipitation behaviour and so on. Usually Fe_3C contains some alloying elements such as Cr and Mn when it is present in steel. The influence of the solute atoms on various properties of Fe_3C has been studied experimentally, i.e., the lattice parameter [1], magnetic behaviour [2,3], mechanical property [4]. On the theoretical side, in view of these structural features, nearly fifty years ago the chemical bonding of Fe_3C was discussed without detailed electronic structure calculations. Petch [5] suggested that Fe_3C structure is more dominated by the Fe-Fe bonding than by the Fe-C bonding. On the other hand, Pauling [6] suggested that the Fe-C bonding was twice as strong as the Fe-Fe bonding.

As mentioned in the preceding chapter, in contrast to a considerable number of theoretical works for the groups IV and V transition metal carbides with the rock-salt type structure such as TiC and VC, there are only a few calculations on other transition metal carbides since they exhibit complicated crystal structures. The band-structure of Fe_3C was calculated in two works [7,8]. Tight binding calculation of a series of iron carbides was done by Cottrell [9]. As regards solute atoms in Fe_3C, the influence of additional elements on the graphitization of Fe_3C was discussed by the use of cohesive energy obtained by extended Hückel molecular orbital method [10] But they suggested that the Fe-C bonding could be changed by additional elements.

In this chapter, we have calculated the electronic structure of Fe_3C containing 3d transition metal (Ti, V, Cr, Mn, Co and Ni) as solute atoms by first principles molecular orbital calculations using the DV-X*a* cluster method. We quantitatively discuss the change of the chemical bonding induced by the solute atoms. In order to understand the relationship between the bond strength and the solution hardening or softening behaviour, the calculated results are compared with the experimental Vickers hardness of Fe_3C containing Cr, Mn, or Ni reported by Inoue *et al.* [4].

5.2 The Crystal Structure of Fe_3C

The crystal structure of Fe_3C was first studied by Westgren and Phragmén [11,12] . The position of atoms was first established by Lipson and Petch [13] and afterwards a large number of studies have been made to determine the lattice parameters and the positions of atoms exactly [14-18]. In many works for Fe3C, the lattice parameters were given in *cab* setting in the extended symbol *Pmcn* which is the same spacegroup *Pnma*. If the *cab* setting are employed for Fe_3C, the lattice parameters are a=4.5248Å, b= 5.0896Å and c=6.7443Å. The primary slip plane [19] , plane defects [20] and the orientation relation ship with ferrite [21,22] were usually discussed using the *cab* setting. In Chapter 4, we employed the standerd setting, a=5.0896Å, b=6.7443Å and c=4.5248Å, because in crystallographic databases, the lattice parameters and atomic positions are given in the standard setting. In this chapter, we shall discuss the variation of Vickers hardness of the Fe_3C solid

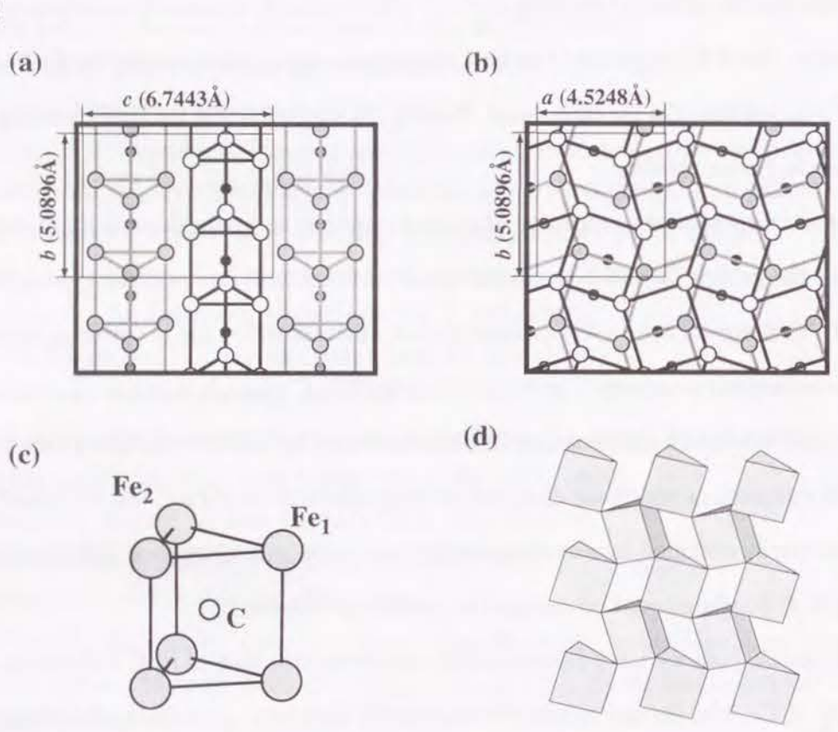

Fig. 5-1 The structure of Fe_3C (cementite) in the *cab* setting.
(a) The (100) projection.
(b) The (001) projection.
(c) Local structure around carbon atom: a trigonal prism composed of six Fe atoms and one carbon atom.
(d) The arrangement of the trigonal prisms in the layer.

solutions and the primary slip plane of Fe_3C. Therefore, for consistency with previous works, the *cab* setting are employed in following sentences. The crystal structure of Fe_3C in the *cab* setting is shown in Fig. 5-1. It has an orthorhombic unit cell with four C atoms, four Fe_1 atoms and eight Fe_2 atoms [18]. Fe_1 and Fe_2 denote Fe atoms at two different crystallographic sites: 8*d* and 4*c* sites in Wyckoff notation, respectively. Every C atom is surrounded by six Fe atoms at an average distance of 2.018Å forming a trigonal prism (Fig. 5-1(c)). In a trigonal prism of Fe_3C two Fe_1 sites and four Fe_2 sites exist. The Fe_1 has 12 nearest neighbour Fe atoms at an average distance of 2.630Å and tow nearest neighbour C atoms at an average distance of 1.978Å. The Fe_2 has 11 nearest neighbour Fe atoms at an average distance of 2.591Å and two neighbour C atoms at an average distance of 2.038Å. The arrangement of Fe atoms is nearly closed-pack. The Fe-Fe distance in Fe_3C is only 2%(Fe_1) and 0.5%(Fe_2) greater than that in fcc-Fe (γ-Fe), i.e. 2.579Å.

The prisms are joined together by sharing their corners and edges to make a layer (Fig. 5-1(d)). These layers are stacked along the c-axis with the sequence of ABAB... Two types of the layers, A and B, have the same arrangement of trigonal prisms and are mutually related by inversion symmetry. Between these layers in the unit cell, there are 28 Fe-Fe bonds whose average distance is 2.544Å. As seen in Fig. 4-9, there are eight Fe-C bonds with the distance of 2.372Å, which is 18% longer than the nearest neighbour Fe-C bond length. Therefore, the Fe-Fe bonding should be dominant for the adhesion of these layers. There is virtually no C-C direct bonding in Fe_3C because the nearest neighbour distance between C atoms is 3.09Å which is 100% greater that the C-C covalent bond length, 1.54Å.

5.3 Model Clusters

The model cluster, $Fe_{46}C_{10}$-X_2 (X=Ti, V, Cr, Mn, Fe and Co), employed in this calculation for Fe_3C is shown in Fig. 5-2. The $Fe_{46}C_{10}$-X_2 cluster has two layers which are composed of five trigonal prisms by sharing their edges and corners. According to the Mössbauer study by Schaaf *et al* [3], Cr and Mn atoms prefer to occupy the Fe_2 sites in Fe_3C. Therefore, we substituted one Fe_1 atom in each layer with 3d transition metal atoms, i.e. Ti, V, Cr, Mn, Co and Ni. In order to maintain the inversion symmetry of the model cluster, two Fe atoms were substituted by the other metal atoms. The computation time is remarkably saved in this way. Two solute atoms in the cluster are so separated that there is practically no interaction between them.

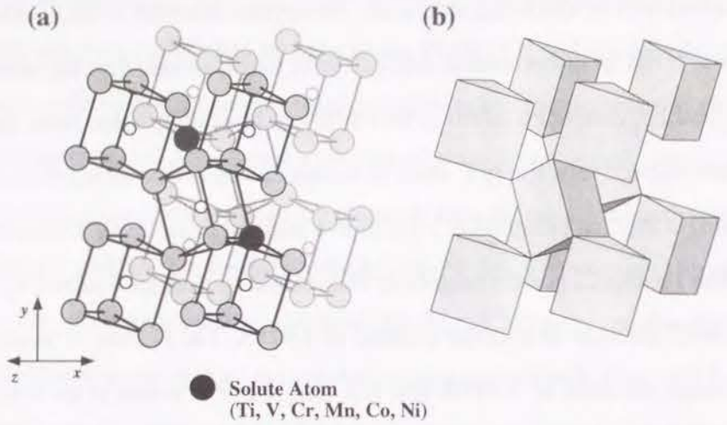

Fig. 5-2 The structure of model cluster employed in this work.
(a) The model cluster, $Fe_{46}C_{10}$-X_2; large gray circles: Fe atoms; large solid circles: solute atoms; small open circles: carbon atoms.
(b) The arrangement of trigonal prisms in the model cluster.

5.4 Results

5.4.1 Pure Fe_3C

Figure 5-3 shows the total and partial density of states (DOS) curves for the valence states of the $Fe_{48}C_{10}$ cluster which is a model of pure Fe_3C. These DOS curves are made by broadening the discrete energy levels by Gaussian function of 1.0 eV FWHM. They are shifted so as to set the Fermi level at zero. The large band around the Fermi level is mainly composed of the Fe 3d orbitals. The lower part of this band which shows two peaks at about -5eV corresponds to the C 2p orbitals interacting with the Fe 3d, 4s and 4p orbitals. The band located at about -12eV is mainly composed of the C 2s orbital interacting with the Fe 3d, 4s and 4p orbitals. The basic features of our DOS agree with those in the use of the LMTO calculation by Häglund *et al* [8].

The metal-metal (M-M) and metal-C (M-C) overlap population diagrams for $Fe_{48}C_{10}$ cluster are shown in Fig. 5-4. They are obtained by convoluting the overlap population at each molecular orbital with Gaussian function of 1.0 eV FWHM. The bond overlap population can be obtained by summing the overlap population on each molecular orbital up to the Fermi level. In this figure Metal-Metal refers to an average of overlap populations between the Fe_2 atom near the center of the cluster and its nearest neighbour Fe atoms. Metal-C refers to an average of overlap populations

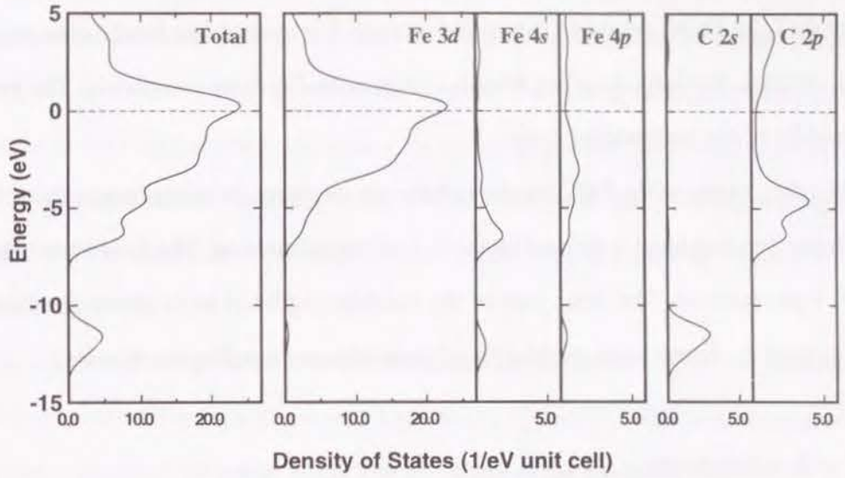

Fig. 5-3 Total and partial density of states for the $Fe_{48}C_{10}$ cluster.

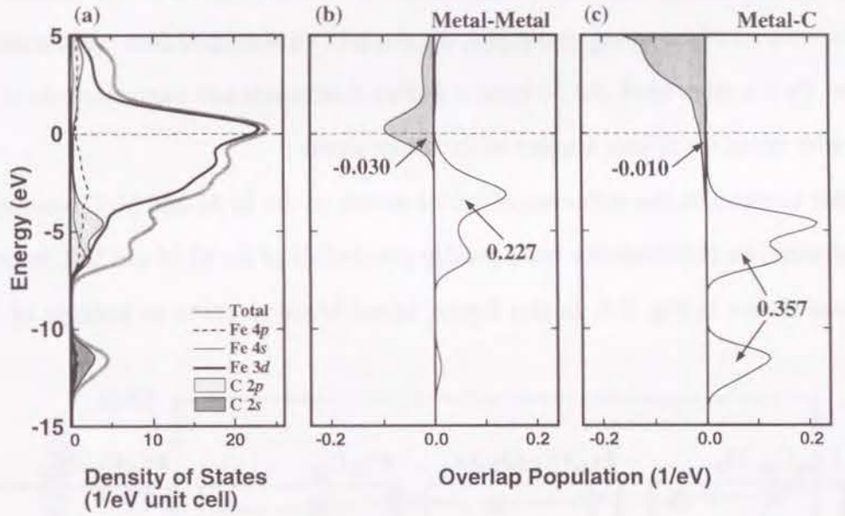

Fig. 5-4 Total and partial density of states and the overlap population diagrams for the $Fe_{48}C_{10}$ cluster for the M-M bond and for the M-C bond.
(a) Total and Partial density of States.
(b) Overlap population diagram for the M-M bond (c) for the M-C bond.

between the C atom in the prism located near the center of the cluster and its nearest neighbour Fe atoms. The values written in each panel are the bonding and the antibonding contributions to the bond overlap population, which were obtained by summing the positive and negative values of the overlap population up to the Fermi level, respectively.

Regarding the M-M bonding, there are a large bonding band and a small antibonding band. The upper part of the bonding band is mainly composed of the Fe 3d orbitals and the lower part is

composed of the C 2p-Fe 3d, 4s and 4p hybridized orbitals. The antibonding band is mainly composed of the Fe 3d orbitals. The large bonding band is occupied by electrons completely. The Fermi level lies at the middle of the antibonding band.

On the other hand, on the M-C bonding, there are two large bonding bands under the Fermi level. The upper bonding band is formed by the C 2p-Fe hybridization. The lower one is formed by the C 2s-Fe hybridization. The large part of the antibonding band exits above the Fermi level. Therefore, around the Fermi level the M-C bond is nearly non-bonding in character.

5.4.2 Fe_3C with solute atoms

The partial density of states of solute-3d and 4sp are plotted for the $Fe_{46}C_{10}$-Ti_2, $Fe_{46}C_{10}$-Cr_2, $Fe_{48}C_{10}$ and $Fe_{46}C_{10}$-Ni_2 clusters in Fig. 5-5. The 4sp band is slightly getting larger with an increase of the atomic number of the solute atoms. But, the shape of the 4sp band does not change with the solute atoms. On the other hand, the 3d band is shifted downwards and more electrons occupy the 3d orbitals with rising the atomic number of the solute atoms.

In order to estimate the influence of solute atoms on the M-M and M-C bondings in the $Fe_{46}C_{10}$-X_2 clusters, we calculated the bond overlap populations of the M-M and M-C bondings and the results are shown in Fig. 5-6. In this figure, Metal-Metal refers to an average of the bond

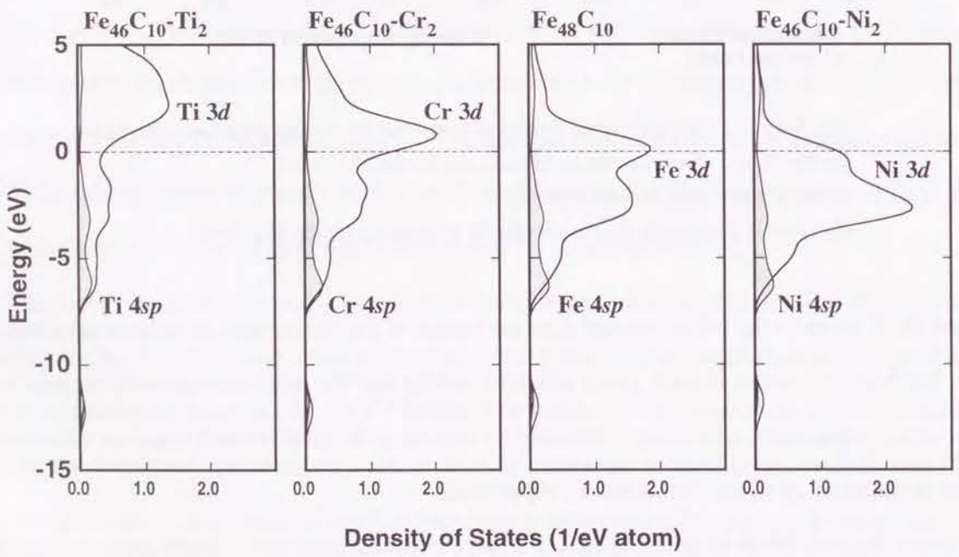

Fig. 5-5 Partial density of states of solute atoms-3d and 4sp.

overlap populations between the solute atom and its nearest neighbour Fe atoms. Metal-C refers to an average of the bond overlap populations between the carbon atom and its nearest neighbour metal atoms in the trigonal prism containing the solute atom. The bond overlap population of M-C is about 0.34 irrespective of the solute atoms. On the other hand, the bond overlap population of M-M strongly depends on the atomic number of the solute atom. It shows the maximum value of 0.22 when the solute is Cr.

The net charge of the solute atoms and C atoms are plotted in Fig. 5-7. In the undoped cluster, small charge transfer from Fe to C is found. The ionicity of the C is -0.3 which is almost independent of the atomic number of the solute atom. The net charge of the solute atom decreases almost linearly with the increase of the atomic number of the solute atom. As a result, a solute atom that has smaller atomic number than Fe, i.e. Ti, V, Cr and Mn becomes more ionic than Fe in Fe_3C. On the other hand, the ionicity of Co and Ni in Fe_3C is less ionic than that of Fe.

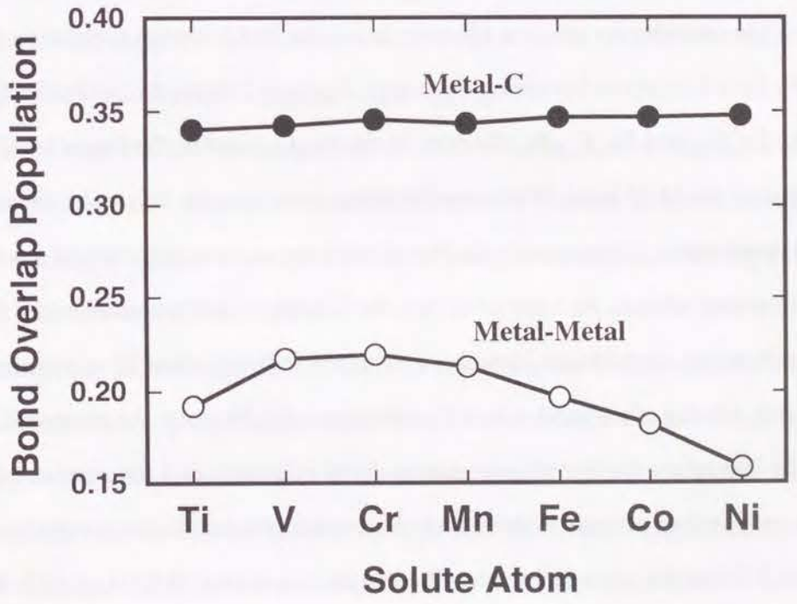

Fig. 5-6 Variation of bond overlap population with the solute atoms.

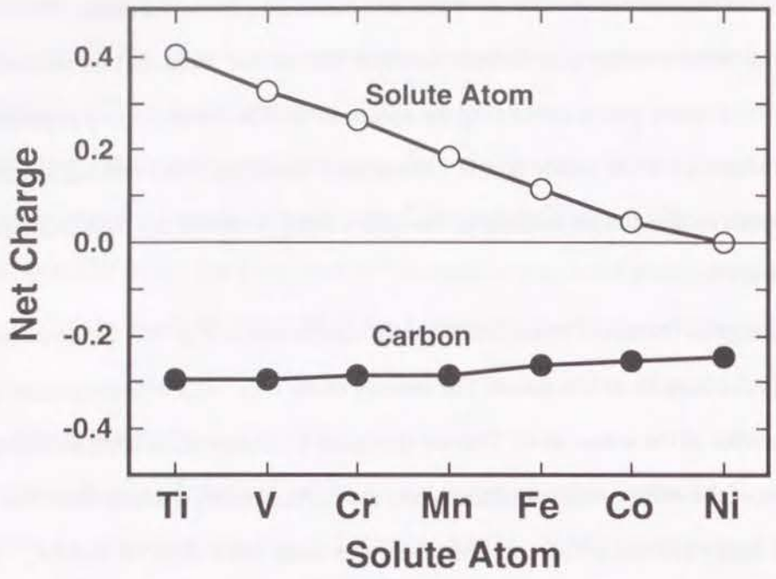

Fig. 5-7 Variation of net charge with the solute atoms.

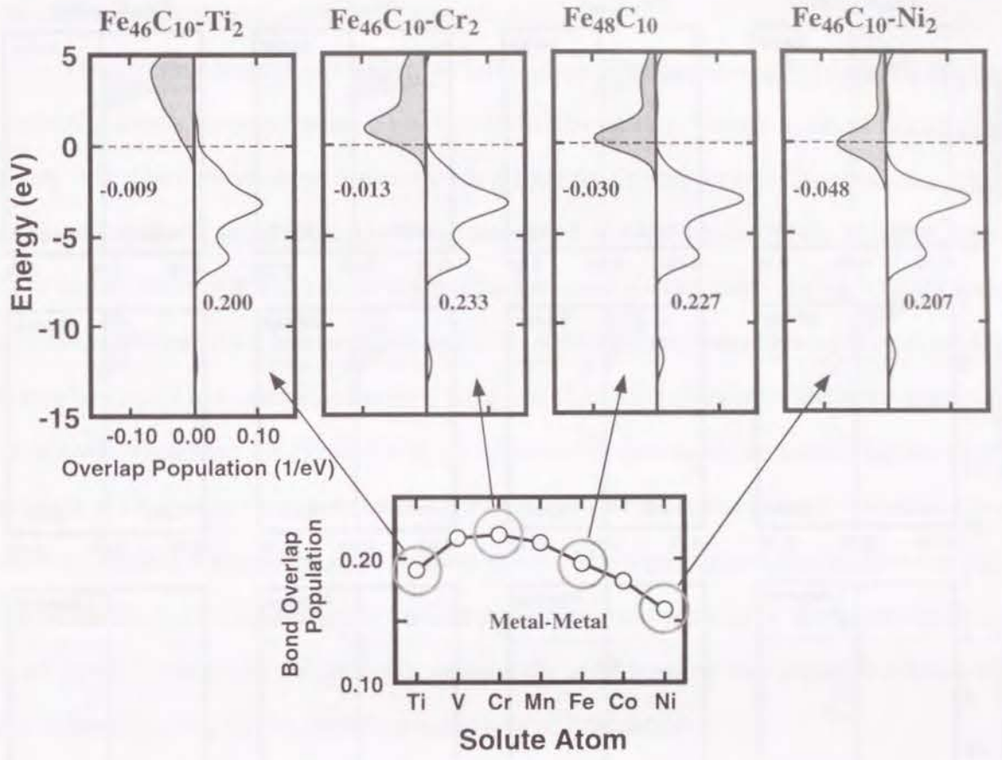

Fig. 5-8 Variation of overlap population of the M-M bond with the solute atoms.

5.5 Discussion

As seen in Fig. 5-6 the solute atoms have larger influence on the M-M bonding than the M-C bonding. In order to consider the solution effect in detail, the M-M overlap population diagram of the clusters with the solute atoms have been examined. Figure 5-8 shows the results for the $Fe_{46}C_{10}$-Ti_2, $Fe_{46}C_{10}$-Cr_2, $Fe_{48}C_{10}$ and $Fe_{46}C_{10}$-Ni_2 clusters. In the $Fe_{48}C_{10}$ cluster, the Fermi level lies in the antibonding band of the M-M bond. When two Ni atoms substitute the Fe atoms, the antibonding band is shifted downwards. Consequently the Fermi level moves up relatively and more electrons occupy the antibonding orbitals. As a matter of fact, the bonding contribution decreases from 0.227 to 0.207 and antibonding contribution increases from 0.030 to 0.048 when Ni substitutes the Fe as shown in Fig. 5-8. On the other hand, when Cr substitutes the Fe atom, the antibonding band is shifted upwards. Therefore the Fermi level moves down relatively and the number of electrons occupying the antibonding orbitals is decreased. As a result, the bonding contribution increases from 0.227 to 0.233 and the antibonding contribution decreases from 0.030 to 0.013. When Ti is doped, the Fermi energy becomes much lower in energy ; It crosses the bonding band. The bonding

contribution therefore decreases concurrently to the decrease in the antibonding contribution. The balance of the bonding and the antibonding contributions is found to determine the atomic number dependence of the bond overlap population drawn in Fig. 5-8.

In order to elucidate the mechanism of the M-M bonding in more detail, the partial overlap populations between atomic orbitals are examined. Figure 5-9 shows the partial overlap population diagram for 3d-3d, 3d-4sp and 4sp-4sp of the M-M bond. The component 3d-4sp is the sum of 3d (solute)-4sp (Fe) and 4sp (solute)-3d (Fe).

Two things can be learned from Fig. 5-9. One is that the anti-boding contribution of the 3d-3d and 3d-4sp increase notably with rising atomic number of the solute atom. It is not the case for the 4sp-4sp antibonding. With the increase of the atomic number of the solute, nuclear potential is deepened together with the increase of the number of electrons : They change the shape and position of the 3d band considerably as shown in Fig. 5-5. The effects are much smaller for the 4sp band. The other point we should emphasize in Fig. 5-9 is the bonding contribution of the 3d-4sp and the

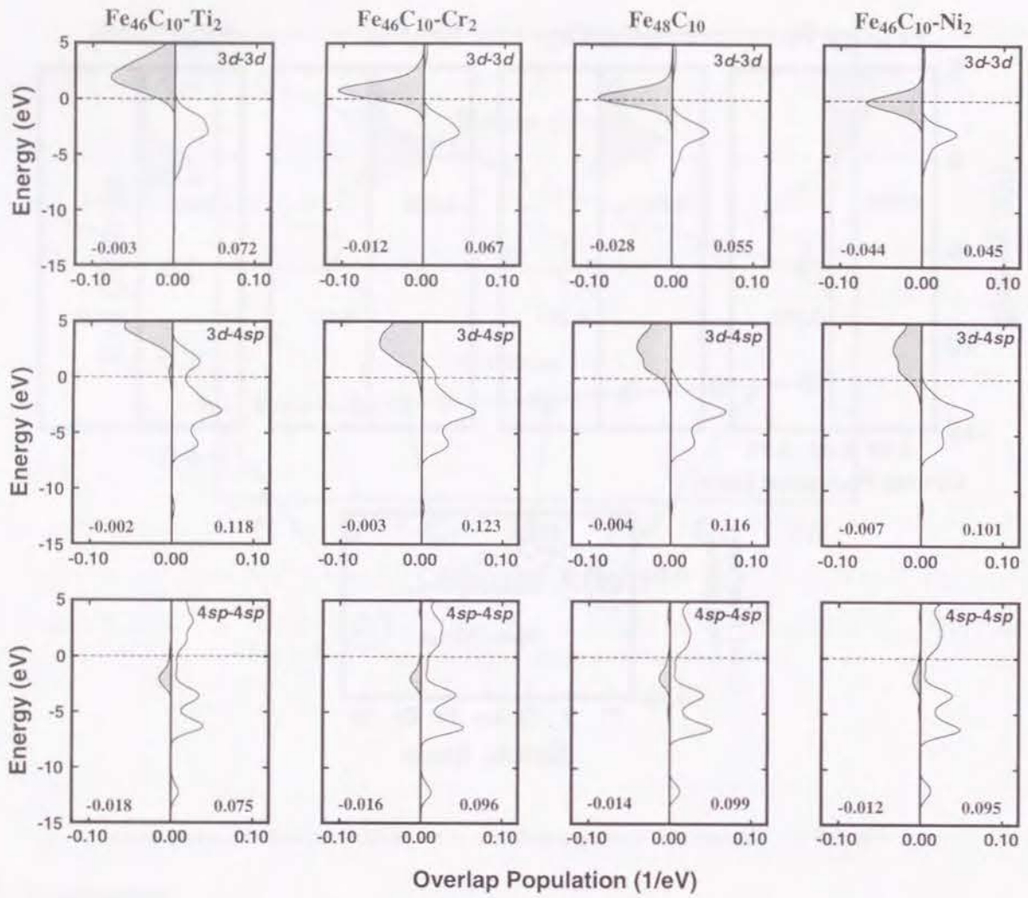

Fig. 5-9 Partial overlap population diagrams of 3d-3d, 3d-4sp and 4sp-4sp for the M-M bond.

4sp-4sp. The magnitude of the 4sp-4sp bonding increases with rising the atomic number of the solute. On the other hand, the bonding contribution of the 3d-3d simply decreases with rising atomic number. This decrease is due to the contraction in the size of the 3d orbitals with the increase of the atomic number of the solute atoms.

In contrast to the M-M bond, the M-C bond exhibits little dependence on the atomic number. As discussed with Fig. 5-4, the bonding band and the antibonding band of the M-C bond are largely separated and molecular orbitals near the Fermi level are nearly of non-bonding character. Therefore, the changes of the number of electrons in both bonding and antibonding orbitals for different solute atoms are very small. This is the reason why the magnitude of the M-C bond is almost independent of the atomic number. As a consequence, the M-M bond is expected to play more important role on

the effect of the solute atoms in Fe_3C than the M-C bond.

The Vickers hardness of Fe_3C-based solid solutions by Inoue *et al.* [4] is shown in Fig. 5-10. Vickers hardness decreases when Ni is doped. On the contrary, Vickers hardness is increased with Cr and Mn. The concentration dependence is greater for Cr than for Mn. The dependence has been explained by the weaking of the M-C bond associated with the increase of the atomic number from Ti to Ni [4], since bulk TiC has the highest hardness and melting point among 3d transition metal carbides. Later transition elements such as Fe, Co and Ni do not form stable carbides in equilibrium. It may be natural to suspect that the M-C bond is weakened with the increase of the atomic number of M even when they are present in Fe_3C. Contrary to this view, we found that the M-C bond strength in Fe_3C does not depend on the atomic number of the solute atom. It is the M-M bond not the M-C bond that shows the great solution effects. The experimental results shown in Fig. 5-10 can be well explained assuming that the Vickers hardness is determined by the magnitude of covalent bond strength around the solute atoms, because the M-M bond overlap population decreases with the order of Cr, Mn, Fe, Ni according to the present calculation.

The primary slip plane of Fe_3C is (001) [19]. The (001) plane is parallel to the layers composed of trigonal prisms (Fig. 5-1(a)). As described previously, the dominant chemical bonds between

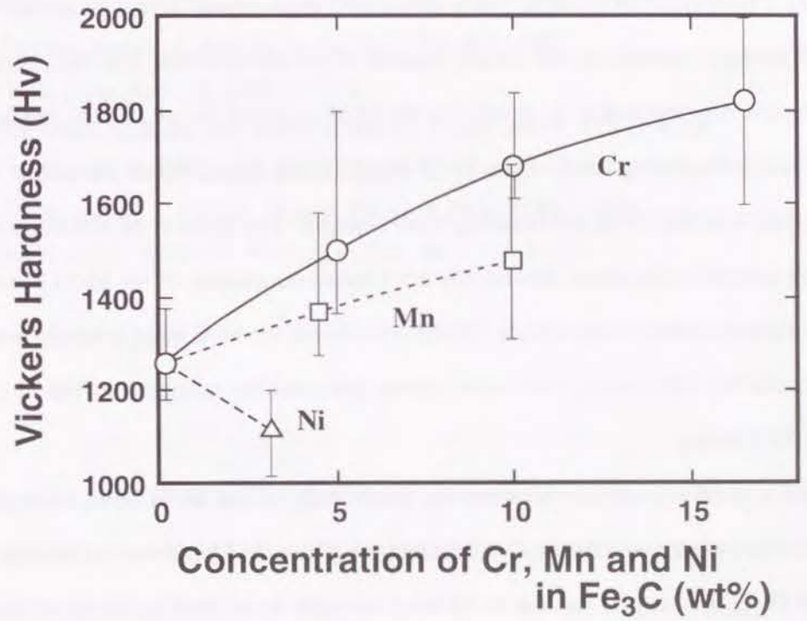

Fig. 5-10 Solute concentration dependence of Vickers hardness reported by Inoue *et al.* (1974).

these layers are the M-M bonds. The strength of the M-M bond rather than that of the M-C bond may determine the critical stress for dislocation motion in Fe_3C. The result of geometric consideration is therefore consistent with our conclusion obtained by electronic calculations.

The importance of the M-M bond has often been ignored in the discussion of properties of transition metal carbides. It is true that the M-C bond is strong in such carbides. However, the magnitude of the M-C bond does not exhibit strong dependence on the atomic number of M in general: as discussed in Chapter 3, a similar trend can be seen even in pure carbides . The M-M bond changes more significantly than the M-C bond with the atomic number of M in these carbides. Similar atomic number dependence can be seen for hydrogen atom in 3d-transition metals. Adachi and Imoto [23] made a series of DV-Xa calculation on H containing metal clusters. They found that the magnitude of the M-H bond strength does not change notably for different kinds of M while the M-M bond varies significantly. They have well correlated the magnitude of the M-M bond strength with the experimental heat of solution of H in these metals.

5.6 Conclusion

In order to understand the effect of solute atoms on the chemical bonding in Fe_3C, first principles molecular orbital calculations have been made using model clusters of $Fe_{46}C_{10}$-X_2 (X=Ti, V, Cr, Mn, Fe and Ni). The strength of the M-C bond shows little change with the solute atoms, but that of the M-M bond strongly depends on the atomic number of the solute atoms. The results can be well explained using overlap population diagrams for the M-M and M-C bonds. The Fermi level lies at the middle of the antibonding band of the M-M bond in pure Fe_3C. When the solute atoms are present, the position of the M-M antibonding band changes. The number of electrons occupying the antibonding orbitals is therefore altered; the net overlap population of the M-M bond decrease with rising the atomic number of the solute. On the other hand, the M-C bond is nearly non-bonding in character around the Fermi level. The solute atoms have smaller influence on the M-C bonding than on the M-M bonding.

We found a good correlation between the magnitude of the M-M bond strength and the experimental Vickers hardness of the Fe_3C solid solutions. Since the M-M bond is dominant between (001) planes in Fe_3C, it is natural that the M-M bond strength shows strong effects on the hardness which is mainly determined by the (001) slip. The present result is contrary to the previous views:

it has been believed that the M-C bond strength rather than the M-M bond determines the hardness of the Fe_3C solid solutions.

References

[1] M. J. Duggin, D. Cox and L. Zwell, *Trans. Metall. AIME* **236**, 1342 (1966).

[2] G. P. Huffman, P. R. Errington and R. M. Fisher, *Phys. Stat. Sol.* **22**, 473 (1967).

[3] P. Schaaf, S. Wiesen and U. Gonser, *Acta. metall. mater.* **40**, 373 (1992).

[4] A. Inoue, T. Ogura and T. Masumoto, *Bull. Jpn. Inst. Met.* **13**, 653 (1974)

[5] N. J. Petch, *J. Iron. Steel Inst.* **149**, 143 (1944).

[6] L. Pauling, *J. Amer. Chem. Soc.* **69**, 542 (1947).

[7] E. J. Garba and R. L. Jacobs, *J. Phys. Chem. Solids* **50**, 101 (1989).

[8] J. Häglund and G. Grimvall, , *Phys. Rev. B* **44**, 2914 (1991).

[9] A. H. Cottrell, *Mater. Sci. Technol.* **9**, 277 (1993).

[10] S. Yamamoto, Y. Kobayashi, N. Inoyama and A. Kirihata, *Proceedings of the 4th International Symposium on the Physical Metallurgy of Cast Iron*, edited by G. Ohira, T. Kusakawa and E. Niyama (Pittsburgh, Pennsylvania: Materials Research Sociery), p. 103 (1990).

[11] A. Westgren and G. Phragmén, *J. Iron Steel Inst.* **105**, 241 (1922).

[12] A. Westgren and G. Phragmén, *J. Iron Steel Inst.* **109**, 159 (1924).

[13] H. Lipson and N. J. Petch, *J. Iron Steel Inst.* **142**, 95 (1940).

[14] D. Meinhardt, *Arch. Eisenhütt.* **30**, 51 (1959).

[15] K. Löhberg, *Arch. Eisenhütt.* **32**, 409 (1961).

[16] D. Meinhardt and O. Krisement, *Arch. Eisenhütt.* **33**, 493 (1962).

[17] F. H. Herbstein and J. Smuts, *Acta Cryst.* **17**, 1331 (1964).

[18] E. J. Fasiska and G. A. Jeffrey, *Acta Cryst.* **19**, 463 (1965).

[19] A. S. Keh, *Acta Met.* **11**, 1101 (1963).

[20] Z. Nishiyama, A. Kore'eda and S. Katagiri, *Trans. JIM* **5**, 115 (1964).

[21] K. W. Andrews, *Acta. Metall.* **11**, 939 (1963).

[22] D. S. Zhuo and G. J. Shiflet, *Metall. Trans. A* **23A**, 1259 (1992).

[23] H. Adachi and S. Imoto, *J. Phys. Soc. Jpn.* **46**, 1194 (1979).

Chapter 6
Chemical bonding at the Fe/TiX (X=C, N or O) interfaces

6.1 Introduction

Some compounds that have good coherence with Fe matrix have been used for precipitation hardening or intragranular ferrite nucleation site in steel industry [1-3]. One group of most popular compounds for the application is composed of the rock-salt type structure compounds, such as TiC or VC. In order to select the compounds for these applications, the lattice-misfit strain at the metal/compounds interface have often been taken into consideration. However, there have been no discussion about the chemical bonding at the interface of these systems.

Metal/oxide ceramics interfaces play key roles for a number of structural and electronic applications. In recent years, to understand the interfaces, several electronic structure calculations have been performed for some model systems, such as the metal/MgO(001) [4-8] and metal/Al_2O_3(0001) interfaces [9, 10, 11]. In these works the equilibrium interfacial distance or the stable configuration of atoms at the interfaces were evaluated by minimization of total energy using supercell models [4, 5, 7, 8] or image-interaction models [6]. Regarding the chemical bondings at the interfaces, the basic feature of the interaction between metal and oxygen atoms was shown by Johnson and Pepper [9]. They made the calculation of (Fe, Ni, Cu, Ag)/Al_2O_3 interfaces using a self-consistent scattered-wave method with small cluster models composed of seven atoms and found that the strength of covalent bondings at the interface was decreased in the series Fe, Ni, Cu and Ag because of the increasing occupation of antibonding orbitals established by the metal-oxygen interaction. Regarding the metal-oxygen bonding, the similar trend was pointed out by Schönberger *et al.* who made more realistic first-principle calculation of (Ti, Ag)/MgO interfaces[5]. However, strength of covalent bondings is determined by the balance of the bonding and antibonding contributions. It is important to discuss not only the occupation of antibonding orbitals but also the variation of bonding contributions due to the presence of metal atoms. In these previous works, little attention has been given to the metal-metal bond at metal/ceramics interfaces except for Heifets *et al* [8] who reported the Ag-Mg bond at the Ag/MgO interface was negligibly small using *ab initio* Hartree-Fock calculation with a supercell model. However, it does not mean that the metal-metal bond is negligible in general.

In this chapter, we have calculated the electronic structure of the Fe/TiC, Fe/TiN and Fe/TiO interfaces by first principles molecular orbital calculations using the DV-Xa cluster method. All of three compounds, TiC, TiN and TiO, have the rock-salt type structure. These interfaces are suitable for the theoretical calculations because their (001) plain has good orientation relationship with BCC-Fe (001) plain with the lattice mismatches of 3 to 7%. We have evaluated the strength of interfacial bonds at the interface. On the basis of these results, the mechanism of the interfacial bond was investivated with interests of the difference among Fe/TiC, Fe/TiN and Fe/TiO interfaces.

6.2 Model Clusters

The orientation relationship often observed between BCC-Fe and rock-salt type carbides or nitrides is $(001)_{Fe}//(001)_{MX}$ and $[110]_{Fe}//[100]_{MX}$ which is called Baker-Nutting orientation relationship [12,13] as shown in Fig. 6-1. According to this relationship, we employed two model clusters shown in Fig. 6-2 for the calculations of the Fe/TiX interfaces. The model clusters are composed of two BCC-Fe metal layers and two TiX compound layers. The left model cluster in Fig. 6-2 is the Fe-on-X model where Fe atoms are present on the top of X atoms. The middle model cluster is the Fe-on-Ti model where Fe atoms are located on the top of Ti atoms. The table in Fig. 6-1 shows lattice parameters of bulk crystals by experiments and the lattice misfit between BCC Fe and TiX

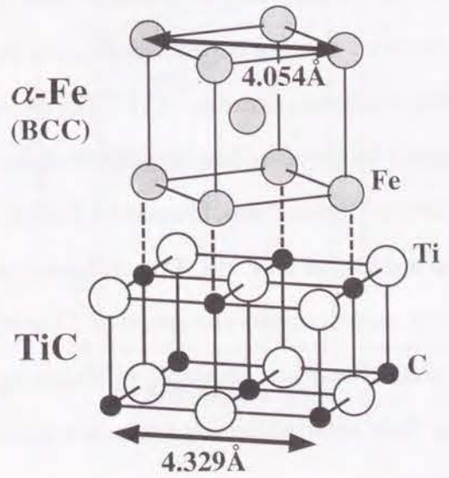

[100]MX // [110]α-Fe

Lattice parameter	Misfit
• TiC (4.329Å)	6.6%
• TiN (4.239Å)	4.5%
• TiO (4.177Å)	3.0%

Fig. 6-1 Baker-Nutting orientation relationship between rock-salt type MX compounds and α–Fe (BCC).

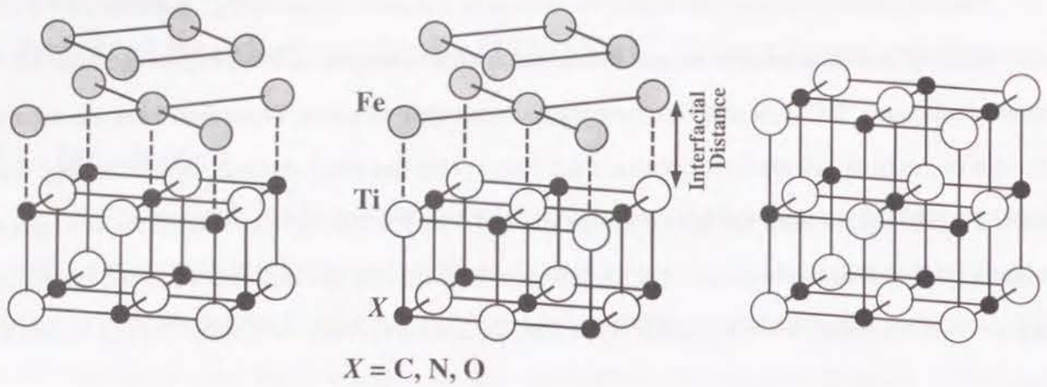

Fig. 6-2 The structure of model clusters employed in this work (*X*=C, N or O).
(a) Fe_9-Ti_9X_9 cluster for the Fe/Ti*X* interfaces where the Fe atoms are on X atoms.
(b) Fe_9-Ti_9X_9 cluster for the Fe/Ti*X* interfaces where the Fe atoms are on Ti atoms.
(c) $Ti_{14}X_{13}$ cluster for bulk Ti*X*.

with the Baker-Nutting orientation relationship. In the present calculation, we expanded the lattice parameter of Fe matrix parallel to the interface so as to fit it with the lattice parameters of TiX for simplicity. Therefore all Fe atoms at the interface are positioned on the top of either Ti or X atoms in these clusters. In order to estimate the influence of the interfacial distance, we have performed the calculation of these models with various interfacial distance between contacting Fe and TiX layers. In Chapter 3, we have already calculated the electronic structure of TiC, TiN and TiO using model clusters composed of 125 atoms and discussed the chemical bonding. However, it is difficult to employ large model clusters for calculations of the Fe/TiX interfaces, because the Fe/TiX interfaces have lower symmery and larger number of metal atoms than bulk TiX. In this chapter, in order to compare with the Fe/TiX interface, we employed model clusters composed of 27 atoms for the calculations of bulk TiX. In the case of TiO, the model cluster was embedded in Madelung potential generated by approximately 2,500 point charges. Spin polarization was taken into account in the calculations of the interfaces containing Fe atoms.

6.3 Results and Discussion

6.3.1 Bulk TiC, TiN and TiO

First of all, we have investigated the chemical bondings in bulk TiC, TiN and TiO. Band structure method has been generally used to calculate the electronic structure of perfect crystalline materials. As described in Chapter 3, several works have already been reported for TiC, TiN and TiO. When valence orbitals are localized in a few ionic shell range, a cluster calculation provides a good approximation for the bulk electronic structure. The cluster calculation is more flexible and useful to be applied for imperfections such as interfaces.

The partial density of states (PDOS) for the valence band and the overlap population diagrams for the Ti-Ti and Ti-X bonds of these model clusters are shown in Figs. 6-3 to 6-5. The PDOS curves are made by broadening the discrete energy levels by Gaussian function of 1.0 eV full width at half-maximum (FWHM). The overlap population diagrams are obtained by convoluting the overlap population at each molecular orbital with Gaussian function of 1.0 eV FWHM. These curves of DOS and overlap population diagrams are shifted so as to set the Fermi level (E_F) at zero. The value written in each panel is the bond overlap population obtained by summing up the overlap population

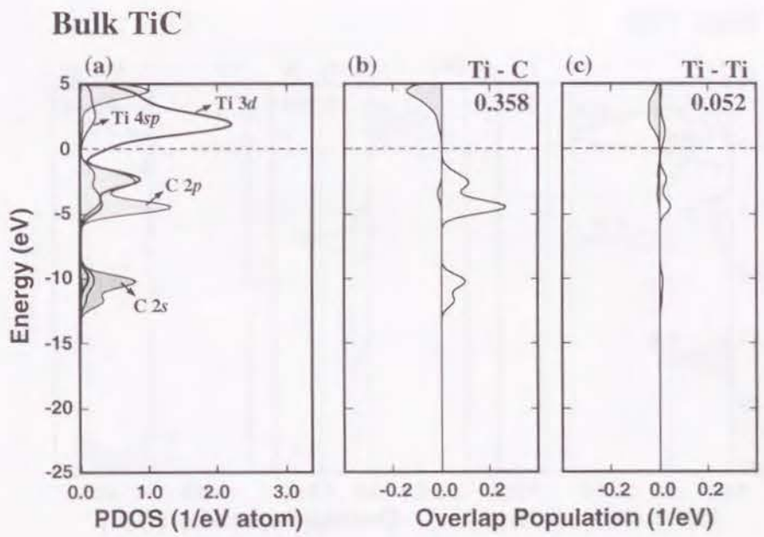

Fig. 6-3 Partial density of states and the overlap population diagrams for bulk TiC for the Ti-C bond and for the Ti-Ti bond.
(a) Partial density of states.
(b) Overlap population diagram for the Ti-C bond (c) for the Ti-Ti bond.

at each molecular orbital up to E_F.

In TiC, there are two large bands below E_F. The upper band located from -5 to 0 eV is mainly composed of the C-2p levels interacting strongly with the Ti 3d, 4s and 4p. The lower band located at about -10 eV is mainly composed of the C-2s levels. The component of the Ti-3d, 4s and 4p orbitals in the C-2s band is smaller than that in the C-2p band. As can be seen in the overlap population diagram, these two bands have large bonding contribution for the Ti-C bonding. The Ti-3d band above E_F is antibonding for the Ti-C bonding.

In TiN, the basic feature of the PDOS and overlap population diagrams is similar to those of TiC. The separation between the Ti-3d and N-2sp bands in TiN is larger than that between the Ti-3d and C-2sp in TiC by 1.8 eV. The Ti orbitals show interaction with the N-2sp orbitals slightly less than the case in TiC. Consequently the magnitude of overlap population for the N-2s and N-2p bands are smaller than the case in TiC.

In TiO, the O-2p band is widely separated from the Ti-3d band. The component of the Ti-3d, 4s and 4p orbitals in the O-2p band is vary small. Therefore, the covalent interaction for the Ti-O bonding is much smaller than that for the Ti-C bonding in TiC or Ti-N bonding in TiN. The O-2s

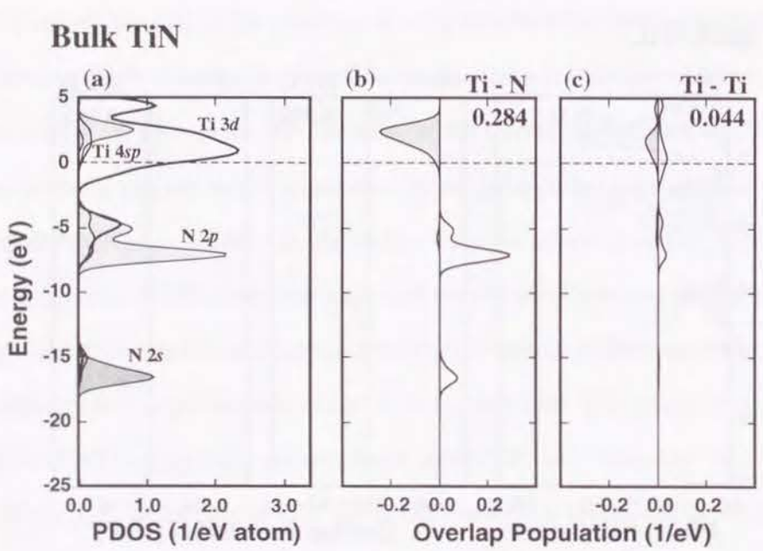

Fig. 6-4 Partial density of states and the overlap population diagrams for bulk TiN for the Ti-N bond and for the Ti-Ti bond.
(a) Partial density of states.
(b) Overlap population diagram for the Ti-N bond (c) for the Ti-Ti bond.

band located at -23 eV has small antibonding contribution for the Ti-O bonding because of the repulsive interaction between the O-2p and Ti-3p core. The Ti-3d band located above E_F contributes to reduce the bonding nature for the Ti-X bond and is considered to be an antibonding band. The antibonding band is empty in TiC and nearly empty in TiN. However, it is partially occupied in the case of TiO. This is the reason why the bond overlap population of Ti-O is much smaller than that of Ti-X in TiC and TiN, and shows rather negative value. The feature of the PDOS for TiC, TiN and TiO in this chapter agree well with that in Chapter 3 calculated using larger model clusters. However, the bond overlap population of Ti-O in Chapter 3 shows small positive value of 0.015. The overlap population diagram for the Ti-O bonding shows that the magnitudes of the bonding contribution in the O-2p band and antibonding contribution in the Ti-3d band are comparable. Therefore, the discrepancy of the bond overlap population is due to the small difference of the magnitude of the bonding and antibonding components and the features of the bonding and antibonding bands in this chapter agree with that in Chapter 3.

The Ti-Ti bond is quite weaker than the Ti-X bond in TiC and TiN. In TiC and TiN, bonding components for the Ti-Ti bond are comprised in the C-2p or N-2p band and the Ti-3d band, though

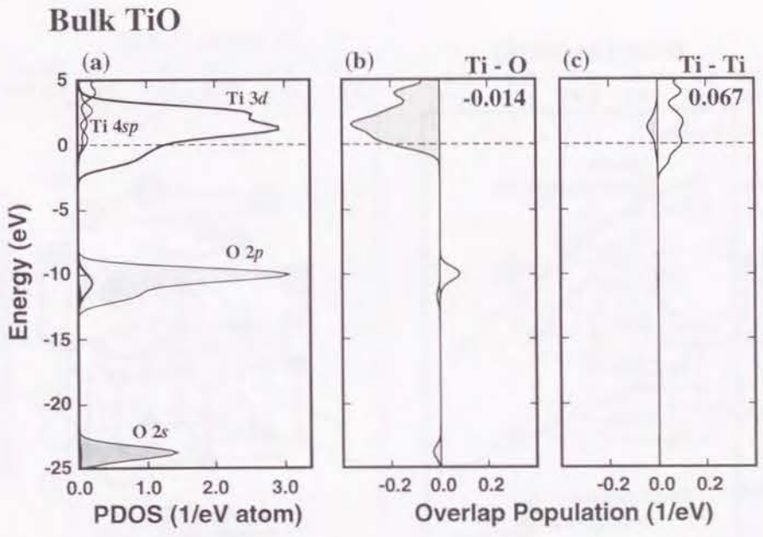

Fig. 6-5 Partial density of states and the overlap population diagrams for bulk TiO for the Ti-O bond and for the Ti-Ti bond.
(a) Partial density of states.
(b) Overlap population diagram for the Ti-O bond (c) for the Ti-Ti bond.

these bonding contributions are very small. On the other hand, in TiO, the Ti-Ti bonding contribution is essentially zero in the O-2p band, but is involved in the Ti-3d band and its magnitude is somewhat larger than that of TiC and TiN.

6.3.2 Preferable position of Fe atoms at the Fe/TiC interface

We have performed the calculations for the Fe/TiC interface with various interfacial distances ranging from 1.6 to 2.4Å. Figure 6-6 and 6-7 show bond overlap populations for Fe-on-C and Fe-on-Ti model, respectively. The label Fe-C and Fe-Ti, respectively, refer to the bond overlap populations for Fe-C and Fe-Ti bonds at the interface. The label Fe-TiC denotes the sum of bond overlap populations for Fe-C and Fe-Ti bonds which corresponds to the magnitude of the total of interfacial bond. The coordination number is taken into account on the Fe-TiC bond; as is seen in Fig. 6-6 and 6-7, the Fe atom has one 1st nearest neighbor (NN) and four 2nd NN atoms of TiX layer at the interface. The bond length between the Fe atom and the 1st NN atom is equal to the interfacial distance. In the range of the interfacial distances, 1.6 to 2.4Å, the 2nd NN are about 1.5 times farther than the first nearest neighbors.

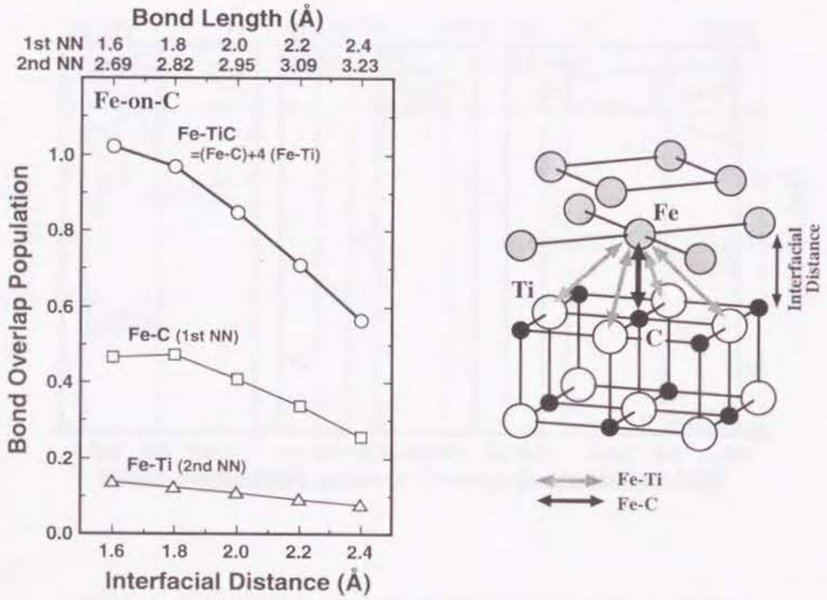

Fig. 6-6 Bond overlap populations of Fe-on-C model for the Fe/TiC interface as a function of the interfacial distance.

In the Fe-on-C model, the Fe atom at the interface has one 1st NN C atom and four 2nd NN Ti atoms. The Fe-C bond strength is increased with the decrease of the interfacial distance and takes the highest value at 1.8Å. The bond overlap population of the Fe-Ti bond is about one fourth of that of the Fe-C bond. However, taking account of the coordination number, the Fe-Ti bond has as large contribution to the Fe-TiC bond as the Fe-C bond.

In the Fe-on-Ti model, the Fe atom at the interface has one 1st NN Ti atom and four 2nd NN C atoms. In comparison with the Fe-on-C model, both 1st and 2nd NN bonds are weaker than those in the Fe-on-Ti model. Therefore, the strength of the Fe-TiC bond in the Fe-on-C model is about twice of that in the Fe-on-Ti model at the same interfacial distance. From metallic radii [14], the Fe-Ti bond length is considered to be longer than the Fe-C. In iron carbide, Fe_3C, the Fe-C and the Fe-Fe bond lengths are 2.018Å and 2.611Å, respectively. At a suitable interfacial distance for the Fe-Ti bond in Fe-on-Ti model, the Fe-C bond length is too long for formation of the Fe-C bond. On the other hand, when the interfacial distance is suitable for the Fe-C bond in the Fe-on-C model, the Fe-Ti bond-length is still within the range of the bonding interaction. Since the number of 2nd NN bonds is four times greater than the 1st NN bonds, the Fe-on-X geometry is expected to be more

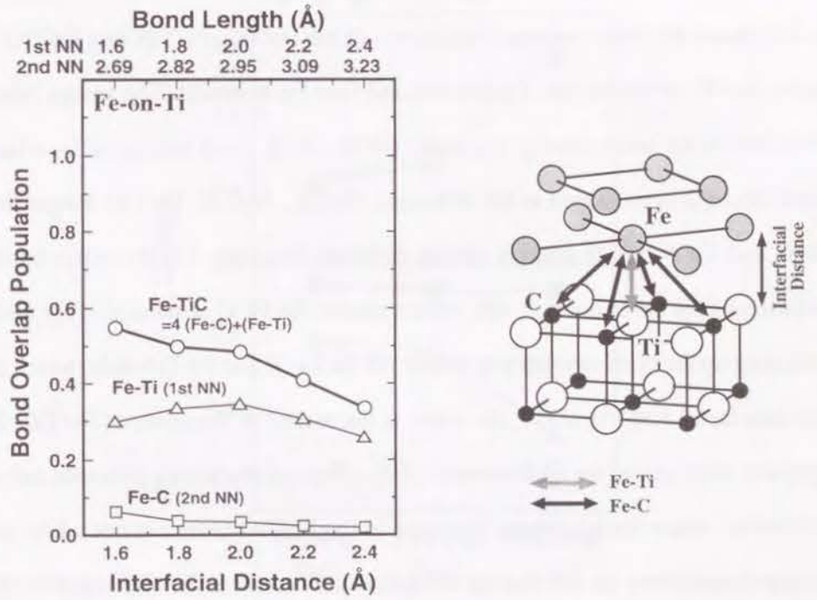

Fig. 6-7 Bond overlap populations of Fe-on-Ti model for the Fe/TiC interface as a function of the interfacial distance.

preferable from the viewpoint of interfacial bond strength. However, the accurate determination of the interfacial distance is rather difficult. The Fe-TiC bond strength calculated in this work does not display a maximum value. In order to estimate the equilibrium interfacial distance, it is necessary to include the bonding interactions near the interface which are ignored in above discussion. They are the Fe-Fe bond in Fe layers and the Ti-C bond in TiC. However, the model clusters employed in this work is not large enough to account them and to quantitatively discuss the strength of these bonds. In the following section, we employ the Fe-on-X models with a fixed interfacial distance of 2.0Å for simplicity and examine the origin of the chemical bonding at these interfaces. The Fe-X distances are 2.018Å, 1.899Å and 2.163Å in Fe_3C, Fe_4N and FeO, respectively. The value 2.0Å for the interfacial distance is determined as an approximate average of Fe-X distances in bulk Fe-X compounds.

TiO layers of the Fe/TiO cluster was embedded in an ionic TiO lattice in the same way as the bulk TiO cluster. In order to estimate the influence of the Madelung potential on the chemical bonding, we have also performed the calculation of the Fe/TiO cluster without the Madelung potential and compare them.

6.3.3 Analysis of the chemical bonding at the Fe/TiC, Fe/TiN, Fe/TiO interfaces

Figure 6-8 shows the bond overlap populations of the Fe/TiC, Fe/TiN and Fe/TiO clusters. At these interfaces, one Fe atom has one Fe-X bond and four Fe-Ti bonds. The marks labeled "4 (Fe-Ti)" in Fig. 6-8 denote the bond overlap population of the Fe-Ti bond multiplied by a factor of four. The Fe-Ti bond strength is increased in the sequence, Fe/TiC, Fe/TiN, Fe/TiO. Regarding the Fe-X bond, the Fe-C and Fe-N bonds display strong covalent bonding. On the other hand, the bond overlap population of the Fe-O bond is -0.1, which means the Fe-O bond is slightly antibonding in character. Summing up the bond overlap populations of the Fe-X and Fe-Ti bonds, which corresponds to the total of interfacial bond strength, the value is decreased in the order of Fe/TiC, Fe/TiN, Fe/TiO. In the present calculation, we take account of the effect of Madelung potential only in the case of Fe/TiO. However, when the Madelung potential in the Fe/TiO cluster is not taken into account, the bond overlap-populations do not change remarkably. Therefore, the difference of the chemical bonding between the Fe-O and the Fe-C, N bond can not be ascribed to the inclusion of the Madelung potential. In the following, we only discuss the chemical bonding of the Fe/TiO cluster with the

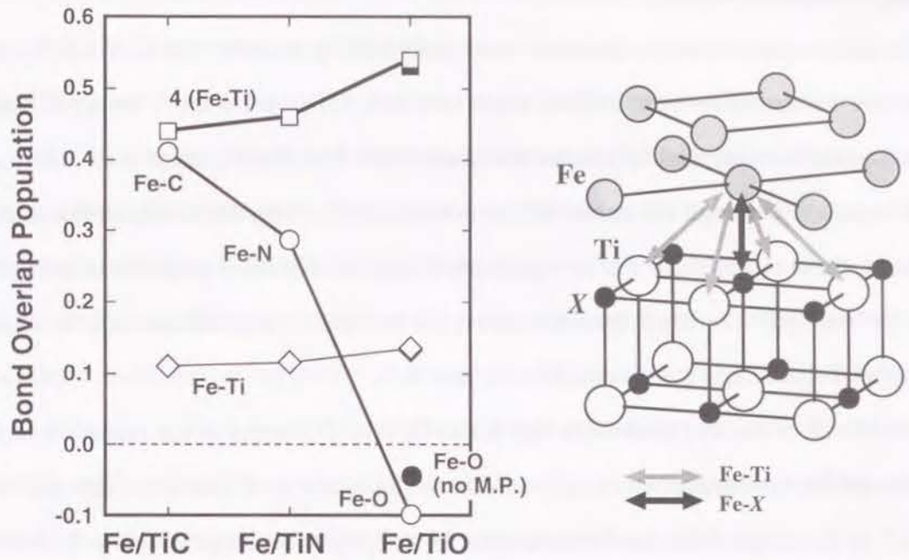

Fig. 6-8 Bond overlap populations at the Fe/Ti*X* interfaces (*X*=C, N or O); Solid marks denote bond overlap populations of the Fe/TiO cluster without the Madelung potential.

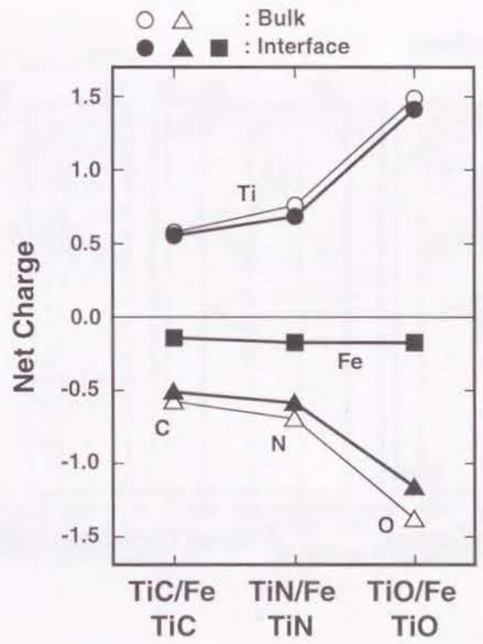

Fig. 6-9 Net charges at the Fe/Ti*X* interfaces and in bulk Ti*X* (*X*=C, N or O); Open marks denote the net charge of Ti and X in bulk TiX and filled marks denote that of Fe, Ti and X at the Fe/TiX interfaces.

Madelung potential for the Fe/TiO interface.

The net charges of atoms in the clusters are plotted in Fig. 6-9. The net charges of Ti atoms at the interfaces are almost the same as those in the bulk TiX. On the other hand, the net charges of X atoms at the interfaces are slightly smaller than that in bulk TiX. The Fe atoms at the interfaces are charged negatively, though the values of the net charges are very small for all the interfaces. Furthermore, these results show that no significant charge transfer takes place between Fe and TiX layers at the interface. Therefore, the ionic interaction between Fe and TiX seems to be small even in the case of TiO which is more ionic than TiC and TiN.

The PDOS of Fe, Ti (3d+4s+4p) and X (X=C, N or O) atoms in the valence band at the interfaces and the overlap population diagrams for the Fe-X and Fe-Ti bonds are shown in Figs. 6-10 to 6-12. In the all interfaces, the Fe component in the up-spin band appears below E_F and has the highest peak at -1.8 eV, while that in down-spin band lies around E_F and has the highest peak at 1.5 eV. The shape of the PDOS of the Ti and X atoms at the interfaces are similar to those in bulk TiX.

At the Fe/TiC interfaces, the Fe band strongly interacts with the C-2p. This causes a large bonding component in the valence band from -7 to 0 eV and a small antibonding component around

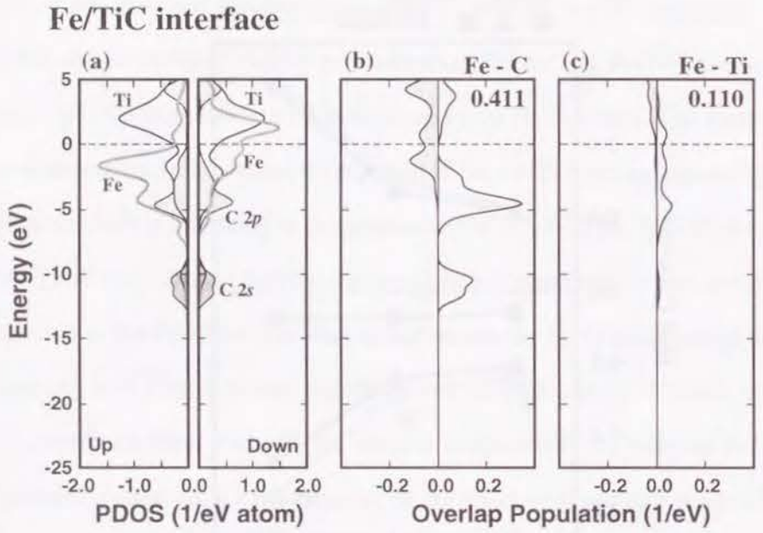

Fig. 6-10 Partial density of states and the overlap population diagrams for the Fe/TiC interface for the Fe-C bond and for the Fe-Ti bond.
(a) Partial density of states (Ti, Fe: 3d+4s+4p, C: 2s, 2p).
(b) Overlap population diagram for the Fe-C bond (c) for the Fe-Ti bond.

E_F with respect to the Fe-C bond. From -13 to -10 eV a small bonding contribution exists mainly composed of the C-2s interacting with Fe orbitals.

The PDOS and overlap population diagrams at the Fe/TiN interface have similar features to those at the Fe/TiC interface. However, the bonding interaction is slightly smaller and the antibonding component is larger than those at the Fe/TiC interface. Therefore, the bond overlap population of the Fe-N bond is smaller than that of the Fe-C bond.

At the Fe/TiO interface, the O-2p band is located at around -10 eV, that is just below the bottom of the Fe band. Regarding the Fe-O bonding, the O-2p band is completely bonding, but the bonding contribution is much smaller than the other two interfaces. In contrast to this, the Fe band is completely antibonding. The antibonding band below E_F is larger than the bonding one. This makes the bond overlap population of Fe-O to be a negative value, -0.098.

As is seen before, the position of the X-2s and 2p bands become lower in the order of, C, N, O. As a result, the bonding interaction becomes smaller in addition to the increment of the number of electrons occupying the antibonding state. This is the reason why the bond overlap population of the Fe-X bond is smaller in the order of, C, N, O.

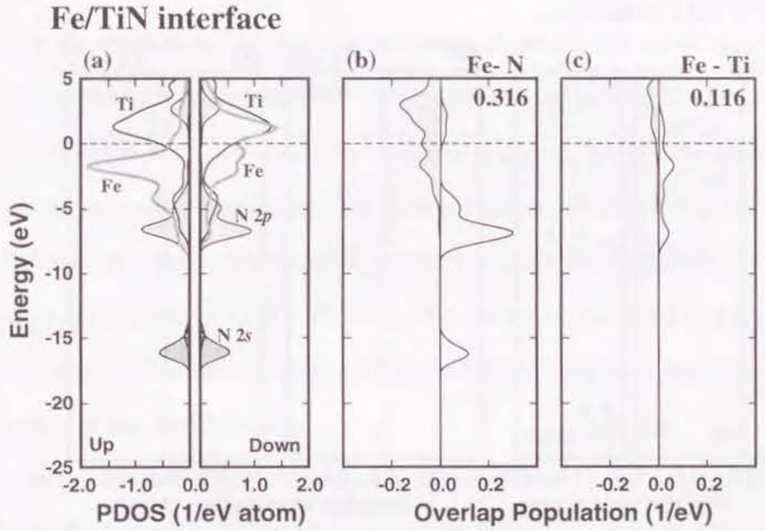

Fig. 6-11 Partial density of states and the overlap population diagrams for the Fe/TiN interface for the Fe-N bond and for the Fe-Ti bond.
(a) Partial density of states (Ti, Fe: 3d+4s+4p, N: 2s, 2p).
(b) Overlap population diagram for the Fe-N bond (c) for the Fe-Ti bond.

Regarding the Fe-Ti bond, at the all interfaces, the Fe band below E_F displays small bonding contribution. At the Fe/TiO interface, the Fe-O bond is of antibonding, therefore, the dominant chemical bonding is the Fe-Ti bond. As mentioned above, previous theoretical calculations pay little attention to the metal-metal bonding at metal/ceramics interfaces. In fact, in the case of Ag/MgO interface, it was reported that the Ag-Mg bond at the interface was negligibly small [8]. In the other calculation for the Ag/MgO interface, it was shown that the Ag band was located at the almost same energy range as the O-2p band, but there was no apparent overlap between the Ag and Mg bands[5]. In the present work, at the Fe/TiO interface, the Fe band interacts with the Ti band around E_F in a certain extent to contribute to the Fe-Ti bonding. In very recent work for the V/MgO interface [15] by the use of DV-Xa molecular orbital calculation, it is suggested that the V-Mg bond displays covalent bonding and the strength of the V-Mg bond is much larger than that of the V-O bond in contrast to the Ag/MgO interface. Therefore, it seems to be important to consider the metal-metal bond formed at the interface between transition metals having unfilled d band and some ceramics.

The TiX compounds act as preferential nucleation site of ferrite (BCC-Fe) when steels are cooled from austenite (FCC-Fe) region. However, the experimental data on the nucleation potency

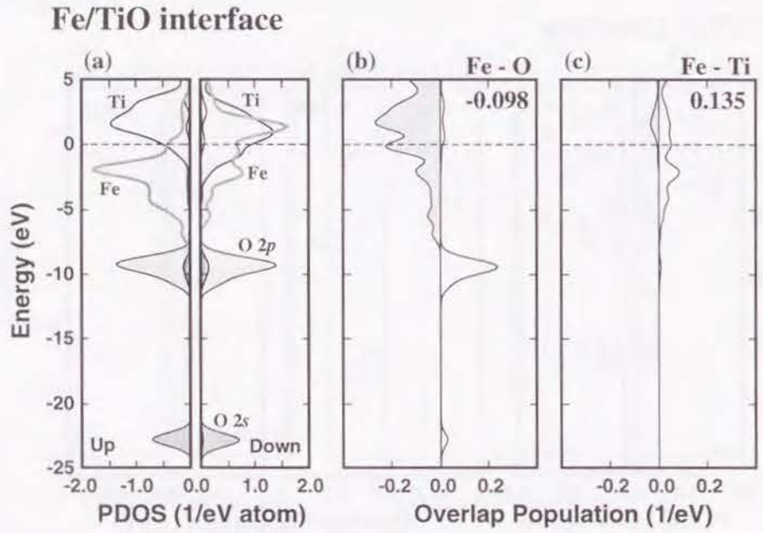

Fig. 6-12 Partial density of states and the overlap population diagrams for the Fe/TiO interface for the Fe-O bond and for the Fe-Ti bond
(a) Partial density of states (Ti, Fe: 3d+4s+4p, O: 2s, 2p).
(b) overlap population diagram for the Fe-O bond (c) for the Fe-Ti bond.

are not well established. Yamamoto *et al.* concluded that TiN was a good ferrite nucleant because of its small lattice mismatch with ferrite [3]. Gregg and Bhadeshia, however, reported that TiO acted as a good nucleant, while TiN did not [16]. Although the mismatch is smaller by 1.5% in Fe/TiO than in Fe/TiN, they were reluctant to accept the lattice matching model. Very recently, Zhang *et al.* investigated the ferrite nucleation effectiveness of pure polycrystal ceramics (TiC, TiN, TiO, VN, AlN and Al_2O_3) [17]. Their results contradicted the data by Gregg and Bhadeshia. They reported that VN, which has the smallest mismatch with ferrite, is the most effective, while TiO, which has the second smallest mismatch, is the least effective. Regarding TiC, TiN and TiO, they reported that the ferrite nucleation effectiveness was decreased in the order of TiC, TiN, TiO. This order is opposite to that expected from the lattice mismatch with ferrite. In other words, the good lattice coherency could not be the major requirement to be a good ferrite nucleant. According to the present calculation, the Fe/TiX interfacial bond strength decreases in the order of TiC, TiN, TiO, which is the same as that in the report by Zhang *et al.* It suggests that the chemical bonding would be more important than the lattice mismatch for the ferrite nucleation in the system Fe/TiX.

6.4 Conclusion

We have performed the first principles molecular orbital calculations using model clusters in order to study the mechanism of chemical bondings at the Fe/TiX (X=C, N or O) interfaces in Baker-Nutting orientation relationship, i.e. $(001)_{Fe}//(001)_{TiX}$ and $[110]_{Fe}//[100]_{TiX}$. We found that, at the all interfaces studied, no significant charge transfer occurs between the Fe atoms and the TiX. Ionic interaction between Fe atoms and TiX is small and covalent bonding is predominant at the interface. At these interfaces, the Fe-on-X geometry is more preferable than Fe-on-Ti because of the long-range interaction of the Fe-Ti bond. The reason is that the Fe-Ti bond is found to be effective even at the 2nd nearest neighbor (NN) sites and the number of 2nd NN bonds is four times greater than that of the 1st NN bonds.

The strength of the Fe-Ti bond is increased in the order of Fe/TiC, Fe/TiN, Fe/TiO. On the other hand, the Fe-X bond is decreased in this order. Especially, at the Fe/TiO interface, the Fe-O bond is slightly antibonding in character. The change of the strength of the Fe-X bond is much larger than that of the Fe-Ti bond. Therefore, the interfacial bond-strength, which is the sum of the strength of the Fe-X and Fe-Ti bonds, decreases in the order of Fe/TiC, Fe/TiN, Fe/TiO.

Several compounds, including TiC, TiN and TiO, have been applied for the intragranular ferrite nucleation site in steels. However, the experimental data on the nucleation potency are not well established. The interfacial bond-strength by the present calculation well agrees with the ferrite nucleation potency, which has most recently been found by experiments which is not expected from the lattice mismatch with ferrite. This suggests that the chemical bonding contribution seems to be larger than the mismatch strain contribution for the ferrite nucleation in these systems.

References

[1] Y. Ito and M. Nakanishi, *J. Japan Weld. Soc.* **44**, 815 (1975).
[2] N. Mori, H. Honma, S. Okita and M. Wakabayashi, *J. Japan Weld.* Soc. **50**, 174 (1981).
[3] K. Yamamoto, T. Hasegawa and J. Takamura, *Tetsu-to-Hagené* **74**, 465 (1988).
[4] C. Li and A. J. Freeman, *Phys. Rev. B.* **43**, 780 (1991).
[5] U. Shönberger, O. K. Andersen and M. Methfessel, *Acta. metall. mater. suppl.* **40**, S1 (1992).
[6] D. M. Duffy, J. H. Harding and A. M. Stoneham, *Acta. metall. mater. suppl.* **40**, S11 (1992).
[7] C. Li, R. Wu and A. J. Freeman, *Phys. Rev. B.* **48**, 8317 (1993).
[8] E. Heifets, E. A. Kotomin and R. Orlando, *J. Phys. Condens. Matter* **8**, 6577 (1996).
[9] K. H. Johson and S. V. Pepper, *J. Appl. Phys.* **53**, 6634 (1982).
[10] K. Nath and A. B. Anderson, *Phys. Rev. B.* **39**, 1013 (1989).
[11] M. Kohyama, S. Kobe, M. Kinoshita and R. Yamamoto, *J. Phys. Chem. Solids* **53**, 345 (1992).
[12] G. Baker and J. Nutting, *Spec. Rept.* **No.64**, 1 (1959).
[13] M. Tanino and T. Nishida, *J. Jpn. Inst. Met.* **29**, 794 (1965).
[14] L. Pauling, *J. Amer. Chem. Soc.* **69**, 542 (1947).
[15] Y. Ikuhara, Y. Sugawara, I. Tanaka and P. Pirouz, *Interface Science* (submitted).
[16] J. M. Gregg and H. K. D. H. Bhadeshia, *Acta Metall. Mater.* **42**, 3321 (1994).
[17] S. Zhang, N. Hattori, M. Enomoto and T. Tarui, *ISIJ int.* 36, 1301 (1996).

Chapter 7
General discussion

7.1 The chemical bonding in titanium compounds

In titanium borides and silicides, the strong B-B and Si-Si bonds are formed, respectively. However, in titanium compounds without TiO, the dominant chemical bonding is the Ti-X bonding (see in Fig. 5-25). The Ti-X bond is formed by the interaction of the X-*n*s and *n*p bands with the Ti-3d, 4s and 4p orbitals. The bonding character around E_F is nearly non-bonding in compounds with the second row elements and is still bonding with the third row elements. The schematic illustrations for the change of the Ti-X bonding in the series of TiC, TiN, TiO is shown in Fig. 7-1. With rising the atomic number of X atoms, the X-*n*s and *n*p band is shifted downwards and the interaction between the Ti and X atoms changes from covalent to ionic.

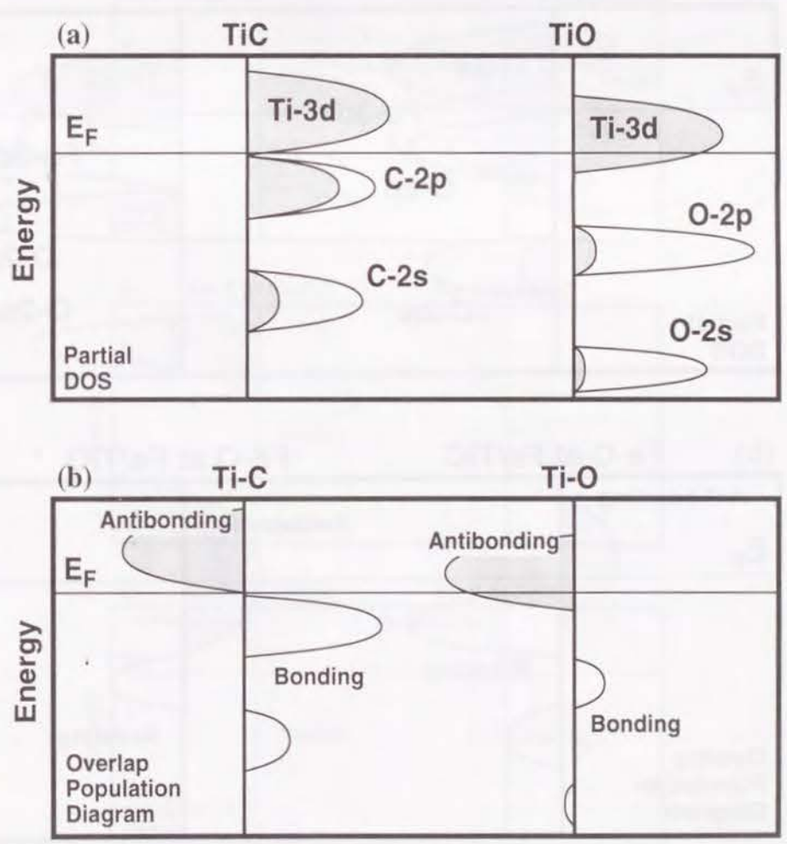

Fig. 7-1 Schematic illustrations of (a) partial density of states and (b) overlap population diagrams for TiC and TiO.

7.2 Lattice imperfections: the Fe/TiX(X=C, N, or O) interfaces

The difference of the chemical bonding among the Fe/TiX (X=C, N or O) interfaces is characterized by the change of the Fe-X bonding. At all interfaces, no significant charge transfer occurs between the Fe and TiX layers. The Fe band at all interfaces is located in the almost same position. The strength of the Fe-Ti bonding slightly increases in the order of the Fe/TiC, Fe/TiN, Fe/TiO, because the overlap between the Fe and Ti-3d bands increases in the same order (Fig. 7-2 (a)). On the other hand, with rising atomic number of the X atoms, the strength of the Fe-X bond in the Fe/TiX interfaces decreases more significantly than that of the Fe-Ti bond. The change of the strength of the Ti-X bond at the interfaces is also more notably than that of the Ti-X bond in bulk TiX. The change of the Ti-X bond in the series of TiC, TiN, TiO is mainly due to the decrease of bonding contribution in the X-2p band. However, at the Fe/TiX interfaces, since more than half of

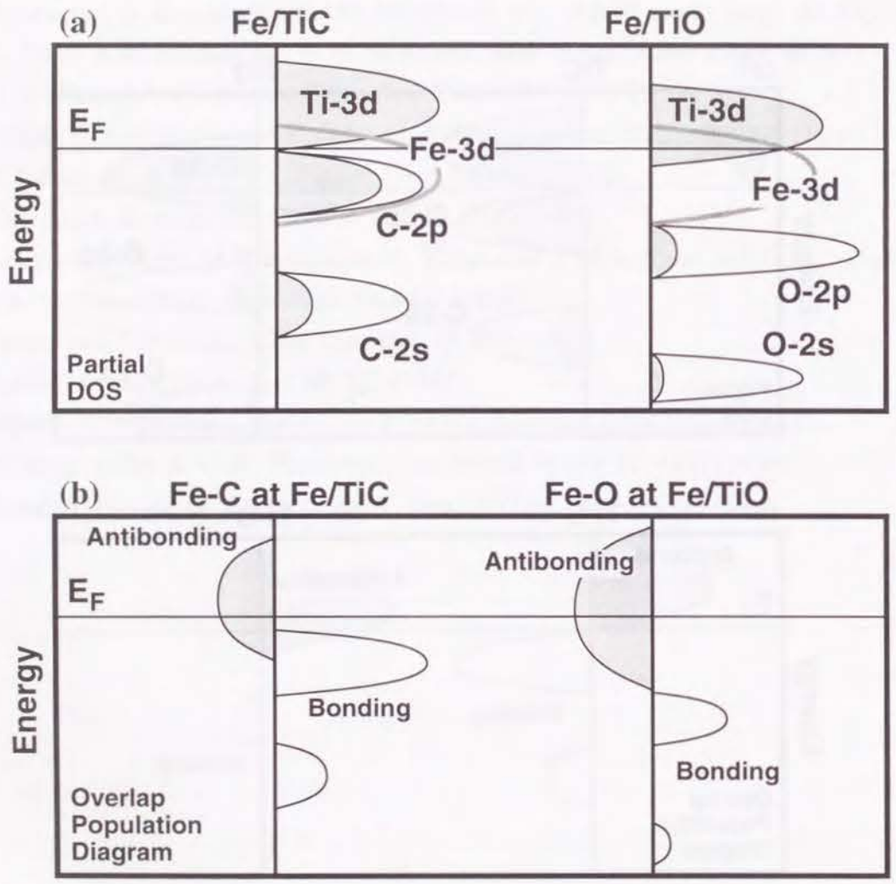

Fig. 7-2 Schematic illustrations of (a) partial density of states and (b) overlap population diagrams for Fe/TiC and Fe/TiO interfaces.

the Fe band is located below E_F, the increase of antibonding contribution is more significant to the change of the Fe-X bonding (Fig. 7-2(b)). From these results, it is expected that in the case of M which has smaller atom number than Fe, the strength of the M-X bond at the M/TiX interface is larger than that at the Fe/TiX. In the case of M which has larger atomic number than Fe, the strength is expected to be smaller because of the increase of the antibonding contribution. The chemical bonding at Fe/VC interface can be also expected from the electronic structure of the Fe/TiC interface and bulk VC in Chapter 5. In VC, the V-3d and C-2p bands are located about 2.0 eV lower than those in TiC. In comparison with the Fe/TiC, it is expected that the Fe-C bond at the Fe/VC interface is slightly weaker because of the increase of the antibonding band (Fig. 7-3 (b)). On the other hand, the increase of the overlap between the Fe and V-3d bands would make the Fe-V bond slightly stronger (Fig. 7-3 (c)).

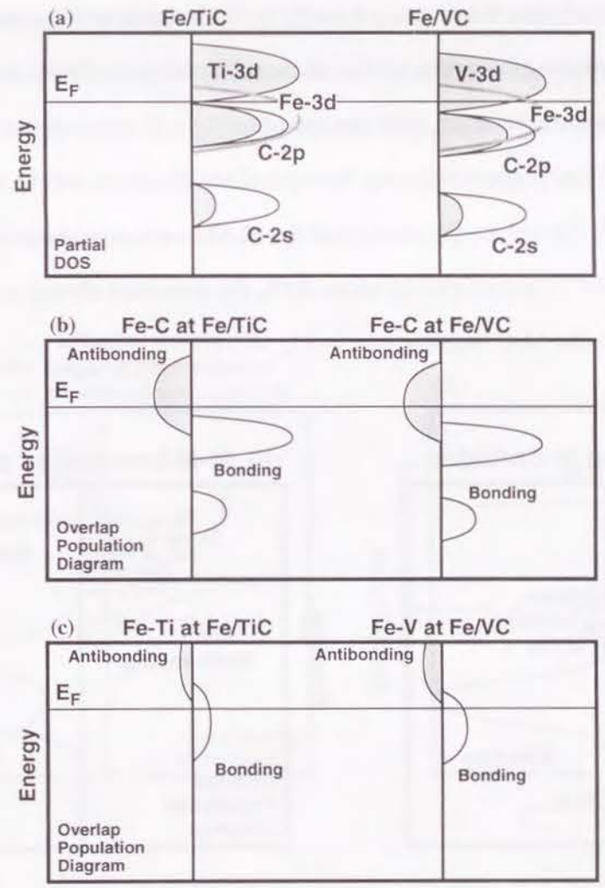

Fig. 7-3 Schematic illustrations of (a) partial density of states and (b) (c) overlap population diagrams for Fe/TiC and Fe/VC interfaces.

7.3 The chemical bonding in 3d transition metal carbides

In 3d transition metal carbides, the strong metal-carbon (M-C) bond is formed by the interaction of the C-2s and 2p band with the M-3d, 4s and 4p orbitals. The strength of the M-C bonds formed around the C atom does not depend on the sort of M atom or the C content (see in Fig. 4-22). The strength of the M-M bond decreases with rising the C content or with rising the atomic number of M from Cr to Ni. These features can be explained by the overlap population diagrams shown in Fig. 7-4 with schematic figures. With respect to the M-C bonding, the C-2s and 2p bands have large bonding contribution. The antibonding component involved in the M-3d band is located above E_F and the bonding character around E_F is nearly non-bonding. This view is common feature in 3d transition metal carbides. Regarding the M-M bonding, the bonding and antibonding bands are located around E_F. In earlier transition metal carbides, E_F lies in upper part of the bonding band. With increasing the atomic number of M, E_F moves upwards and the bonding contribution is the largest around chromium carbides. When going from Cr to Ni, the antibonding contribution increases because of the increase of the occupation of the antibonding orbitals. These features are almost independent of the C content. However, with the increase of the C content, the magnitude of the bonding and antibonding components decrease because of the M-3d, 4s and 4p orbitals employed in forming the M-C bonds. Therefore, the strength of the M-M bonds monotonously decreases with increasing C content. If the C content exceed about 30%, the dominant chemical bonding changes from the M-M bonding to the M-C bonding (see in Fig. 4-24).

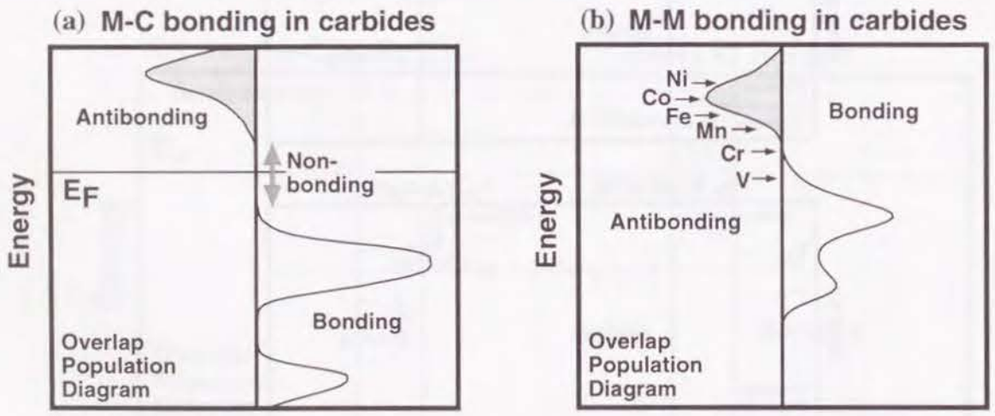

Fig. 7-4 Schematic illustrations of overlap population diagrams for 3d transition metal carbides.
(a) For the M-C bond.
(b) For the M-M bond. Arrows denote the position of the Fermi level.

7.4 Lattice imperfections: solute atoms in 3d transition metal carbides

If the 3d transition metal carbides containing the solute atoms which have larger atomic number, E_F is shifted upwards. In the case of the solute atoms with smaller atomic number, E_F moves downwards. From the overlap population diagrams for the M-M bonding, the change of the M-M bonding induced by the solute atoms can be estimated (Fig 7-5(a)). In the case of Fe_3C, the solute atoms with larger atomic number weaken the Fe-Fe bonding because of the increase of the antibonding contribution. When the solute atoms with smaller atomic number contained in Fe_3C, the E_F moves downwards and the strength of the Fe-Fe bonding increases because of the decrease of the antibonding contribution. In the case of chromium carbides, any solute atoms in 3d transition metals decrease the strength of the M-M bonding, because in pure chromium carbides, E_F is located between the bonding and antibonding band and the shift of E_F always induces loss of the bonding components. Another factor is the change of the magnitude of the bonding and antibonding components because of the change of the M-M interaction. The 3d-3d interaction which is dominant component in the M-M bonding decreases with increasing the atomic number of M. This decrease is due to the contraction in the size of the 3d orbitals with the increase of the atomic number of M. However, a trend of the interaction among 4sp orbitals is opposite to the 3d-3d interaction. Consequently, the M-M interaction shows the maximum around Cr. In comparison with the effect

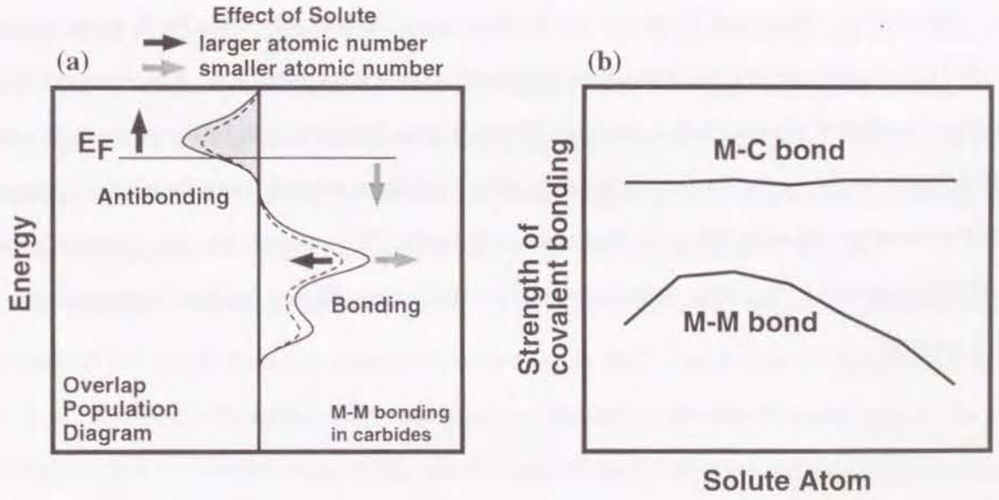

Fig. 7-5 Schematic illustrations for effect of solute atoms in 3d transition metal carbides.
(a) Effect of solute atoms on the M-M bonding. Black and gray arrows denote the effect of the solute atoms which have larger and smaller atomic number, respectively.
(b) The change the strength of the M-C and M-M bonding induced by solute atoms.

of the shift of E_F, the change of the magnitude of the bonding and antibonding components induced by solute atoms has a similar effect on the strength of the M-M bonding. Therefore, the M-M bonding strongly depends on the atomic number of the solute atoms. On the other hand, the solute atoms have quite smaller influence on the M-C bonding than on the M-M bonding, because the M-C bonding is nearly non-bonding in character around E_F. As mentioned above, the M-M bonding is more dominant in carbides including smaller C content. Therefore, the influence of the solute atoms on the M-M bonding is more significant in carbides including smaller C content.

7.5 Relation to experimental works

The change of the magnitude of the M-M bonds in Fe_3C with solute atoms is in good agreement with the variation of Vickers hardness of the Fe_3C solid solutions. Since the M-M bond is dominant between (001) planes in Fe_3C, it is natural that the M-M bond strength shows strong effects on the hardness which is mainly determined by the (001) slip. The present result is contrary to the previous views: it has been believed that the M-C bond strength rather than the M-M bond determines the hardness of the Fe_3C solid solutions.

Several compounds, including TiC, TiN and TiO, have been applied for the intragranular ferrite nucleation site in steels. However, the experimental data on the nucleation potency are not well established. In present calculations, it is was found that the Fe/TiX bond strength decreases with rising atomic number of X because of the decrease of the strength of the Fe-X bond. Although the Fe/TiO interface shows smallest lattice mismatch among three interfaces, it is expected that the chemical bonding at the interface is weakest. The interfacial bond-strength by the present calculation well agrees with the ferrite nucleation potency, which has most recently been found by experiments which is not expected from the lattice mismatch with ferrite. This suggests that the chemical bonding contribution seems to be larger than the mismatch strain contribution for the ferrite nucleation in these systems.

Summary and conclusions

In this thesis, the author performed systematic calculations for the electronic structures of perfect crystalline titanium compounds and 3d transition metal carbides by first principles molecular orbital calculations using the DV-Xα cluster method. The author also carried out the electronic structure calculations for Fe_3C containing solute atoms and Fe/TiX (X=C, N or O) interfaces and discussed the chemical bonding of solutes and interfaces as lattice imperfections. The obtained results are summarized as follows.

In Chapter 3, the electronic structures of titanium compounds, TiB, TiB_2, TiC, Ti_2N, TiN, TiO, TiO_2, TiSi, $TiSi_2$, TiP, TiS and TiS_2 were calculated. In titanium borides and silicides, the strong B-B and Si-Si bonds are formed, respectively. However, in titanium compounds without TiO, the dominant chemical bonding is the Ti-X bonding. The Ti-X bond is formed by the interaction of the X-*n*s and *n*p bands with the Ti-3d, 4s and 4p orbitals. The Ti-X bonding character around E_F in the compounds with the second-row elements is almost non-bonding. On the other hand, that in the compounds with the third-row elements is still bonding.

In Chapter 4, the electronic structures of 3d transition metal carbides, TiC, V_2C, VC, $Cr_{23}C_6$, Cr_7C_3, Cr_3C_2, Mn_3C, Fe_3C, Co_3C and Ni_3C were calculated. In all the carbides, the strong M-C bond is formed by the interaction of the C-2s and 2p bands with the M-3d, 4s and 4p orbitals. The strength of the M-C bonding is almost independent of the sort of the M atoms and the C content in the carbides. The strength of the M-M bonding decreases with the increase of the C content. When going from Mn to Ni carbides, the M-M bonding decreases with rising atomic number of the M atoms because of the increase of the antibonding contribution. If the C content exceed about 30%, the dominant chemical bonding change from the M-M bonding to the M-C bonding.

Chapter 5 deals with solute atoms from Ti to Ni in Fe_3C. Based on the results in Chapter 4, the influence of the solute atoms on the chemical bonding in Fe_3C was discussed. The strength of the M-C bond is almost independent of the solute atoms because of non-bonding character of the M-C bonding around E_F. On the other hand, the strength of the M-M bond strongly depends on the atomic number of the solute atoms. The reason is that E_F lies at the middle of the antibonding band of the M-M bond in pure Fe_3C and solute atoms induce a shift of E_F. The strength of the M-M bond decrease with rising the atomic number of the solute. The change of the strength of the M-M bonds

agree well with the change of the experimental Vickers hardness of the Fe_3C solid solutions, since the M-M bond is dominant between (001) planes which are the primary slip planes in Fe_3C.

Chapter 6 deals with the Fe/TiC, Fe/TiN and Fe/TiO interfaces. At the all interfaces, no significant charge transfer occurs between the Fe and TiX layers. Ionic interaction is small and covalent bonding is predominant at the interface. The interfacial bond strength is stronger when Fe atoms are located on X atoms. The Fe/TiX bond strength decreases with rising atomic number of X. The antibonding of the Fe-O bonds at the Fe/TiO interface is noteworthy. Although the Fe/TiO interface shows smallest lattice mismatch among three interfaces, it is expected that the chemical bonding at the interface is weakest. The interfacial bond strength by the present calculation well agrees with the potency of TiX for intragranular ferrite nucleation in steels that was recently found by experiments.

In conclusion, the author performed systematic calculations for the electronic structure in titanium compounds and 3d transition metal carbides and investigated the chemical bonding at Fe/TiX(X=C, N, or O) interfaces and solute atoms in Fe_3C as lattice imperfections. The author presented that interpretation of the mechanism of the chemical bonding in perfect crystalline compounds can be applied to the estimation of the change of the chemical bonding induced by lattice imperfections in Chapter 7. The finding and concepts in this work would contribute to the investigation of other compounds including lattice imperfections.

Acknowledgment

The author is greatly indebted to Professor Hirohiko Adachi at Kyoto University for his continuous guidance and encouragement throughout the course of this work.

The author is also indebted to Professor Tadashi Maki and Professor Masaharu Yamaguchi at Kyoto University for their helpful comments and the critical reading of the manuscript.

The author is also very greatful to Associate Professor Isao Tanaka at Kyoto University for his continuous guidance and discussions throughout this work.

The author would like to thank Kobe Steel, LTD. for their helpful support and financial assistance.

The author wishes to thank all members of the laboratories under the direction of Professor Hirohiko Adachi.